UNIVERSITÀ DEGLI STUDI DI PADOVA

UNIVERSITA' DEGLI STUDI DI PADOVA

Dipartimento di Ingegneria Industriale DII

Master's Course in Energy Engineering

Experimental and numerical study of a CO_2 heat pump working simultaneously with solar and air as thermal sources

Supervisor: Prof. Marco Azzolin

Co-supervisor: Ing. Riccardo Conte

Student: Marco Lazzarin

Student ID: 2062607

Academic Year 2023/2024

Summary

This thesis investigates experimentally and numerically the performance of a dual-source solar-air heat pump, working with CO_2 as refrigerant. The tested prototype can operate in three different evaporation modes: air-mode (using a finned-coil evaporator), solar mode (using a photovoltaic-thermal PV-T evaporator), and simultaneous mode (using both the evaporators). The simultaneous mode represents a novel solution and it does not require a control to decide which is the thermal source to use because both sources are used at the same time. Experimental data collected in the present and previous years have been analyzed to evaluate the impact of various external conditions.

The thesis is divided into five chapters. The first chapter presents an overview of the state of the art reached by the research sector, both on the dual-source heat pump technology and on the use of CO_2 as a refrigerant. The second chapter describes the main components and layout of the heat pump prototype studied, as well as the measurement system used to collect the data. The third chapter presents the experimental tests performed, focusing on the heat pump system operating in simultaneous mode, when both evaporators work at the same time, and comparing it to the heat pump operating with each evaporator individually. The fourth chapter describes how the experimental data collected has been used to validate the numerical model in steady-state conditions. Following this the chapter delves into the performance of the heat pump in dynamic conditions, demonstrating the model's accuracy in predicting the dynamic behavior while also comparing the performance of the different configurations under the same operating conditions. Finally, the fifth chapter focuses on the seasonal performance of the heat pump system. It numerically compares three heat pump configurations: an air-source heat pump working with propane, a CO_2 air-source system, and a CO_2 dual-source solar-air heat pump. The analysis is based on climatic data from two cities, Rome and Strasbourg, and simulates a building sector user who needs both heating and domestic hot water.

Sommario

Il presente lavoro di tesi indaga sperimentalmente e numericamente le prestazioni di una pompa di calore aria-solare a doppia sorgente, funzionante con CO_2 come refrigerante. Il prototipo testato può operare in tre diverse modalità di evaporazione: modalità aria (utilizzando un evaporatore a serpentina alettata), modalità solare (utilizzando un evaporatore fotovoltaico-termico PV-T) e modalità simultanea (utilizzando entrambi gli evaporatori). La modalità simultanea rappresenta una soluzione innovativa e non richiede un controllo che decida quale sorgente termica utilizzare, in quanto entrambe le sorgenti vengono utilizzate contemporaneamente. I dati sperimentali raccolti negli anni presente e precedenti sono stati analizzati per valutare l'impatto delle varie condizioni esterne.

La tesi è divisa in cinque capitoli. Il primo capitolo presenta una panoramica dello stato dell'arte raggiunto dal settore della ricerca, sia sulla tecnologia delle pompe di calore a doppia sorgente che sull'uso della CO_2 come refrigerante. Il secondo capitolo descrive i principali componenti e il layout del prototipo di pompa di calore studiato, nonché il sistema di misurazione utilizzato per raccogliere i dati. Il terzo capitolo presenta i test sperimentali eseguiti, concentrandosi sul sistema di pompa di calore che opera in modalità simultanea, quando entrambi gli evaporatori lavorano contemporaneamente, e confrontandolo con la pompa di calore che opera con ciascun evaporatore singolarmente. Il quarto capitolo descrive come i dati sperimentali raccolti siano stati utilizzati per validare il modello numerico in condizioni stazionarie. Successivamente, il capitolo esamina le prestazioni della pompa di calore in condizioni dinamiche, dimostrando l'accuratezza del modello nel prevedere il comportamento dinamico e confrontando anche le prestazioni delle diverse configurazioni nelle stesse condizioni operative. Infine, il quinto capitolo si concentra sulle prestazioni stagionali del sistema pompa di calore. Vengono confrontate numericamente tre configurazioni: una pompa di calore funzionante con propano con sorgente aria, un sistema a CO_2 con sorgente aria e una pompa di calore a CO_2 con doppia sorgente aria-solare. L'analisi si basa su dati climatici di due città, Roma e Strasburgo, simulando come utente un edificio che necessita sia di riscaldamento che di acqua calda sanitaria.

Table of Contents

SUMMARY **3**

SOMMARIO **4**

TABLE OF CONTENTS **5**

CHAPTER 1 ..... **1**

INTRODUCTION **1**

1.1 HEAT PUMP TECHNOLOGY 1

1.2 DUAL-SOURCE CONFIGURATION 5

1.3 OVERVIEW OF CO_2 AS REFRIGERANT 7

1.4 SEASONAL PERFORMANCE 10

CHAPTER 2 ..... **12**

EXPERIMENTAL HEAT PUMP SYSTEM **12**

2.1 SOLAR-ASSISTED HEAT PUMP SYSTEM 12

2.2 EXPERIMENTAL UNIT 12

2.3 SYSTEM COMPONENTS 14

2.3.1 Solar collector PV/T *14*

2.3.2 Finned coil heat exchanger *16*

2.4 TRANSCRITICAL CYCLE 16

2.5 MEASUREMENT SYSTEM 18

2.6 CONTROL SYSTEM 20

2.6.1 Control on the operation parameters *20*

2.6.2 Control on the thermal power produced *20*

2.6.3 Control on the electric power produced *21*

CHAPTER 3 ..... **22**

EXPERIMENTAL CAMPAIGN **22**

3.1 DATA REDUCTION 23

3.2 EXPERIMENTAL TESTS IN SIMULTANEOUS MODE 27

3.2.1 Water temperature difference effect *28*

3.2.2 Air temperature effect *29*

3.3.3 Solar irradiance effect *31*

3.3 EXPERIMENTAL TEST IN AIR-MODE 32

3.4. COMPARISON OF THE THREE EVAPORATION MODES 33

CHAPTER 4 ..... **37**

NUMERICAL MODEL **37**

4.1 MODEL DESCRIPTION 37

4.2 CALIBRATION OF THE INTERNAL HEAT EXCHANGER 38

4.3 STEADY-STATE MODEL 41

4.3.1 Simultaneous-mode *41*

4.3.2 Air-mode *42*

4.4 DYNAMIC MODEL 43

4.4.1 Model validation in simultaneous-mode *44*

4.4.2 Comparison between different evaporator modes *46*

4.4.3 Model validation in air-mode *48*

4.4.4 Variable inlet water temperature *51*

CHAPTER 5 ..... **57**

SEASONAL PERFORMANCE OF HEAT PUMPS FOR THE BUILDING SECTOR WORKING WITH NATURAL REFRIGERANTS **57**

5.1 SEASONAL COP DEFINITION 57

5.2 SYSTEM LAYOUT 58

5.3 NUMERICAL MODEL 61

5.3.1 Finned coil evaporator *63*

5.3.2 Compressor sub-model *64*

5.3.3 Water storage tank *65*

5.4 HEAT PUMP DESIGN 70

5.5 RESULTS 74

CONCLUSIONS **82**

APPENDIX **84**

NOMENCLATURE **85**

BIBLIOGRAPHY **86**

Chapter 1

Introduction

In recent years the society has shown a growing awareness of the alarming developments in global warming, and the urgent need to transition to sustainable energy solutions. Actions are being taken worldwide, including infrastructure development, social responsibility initiatives, and changes in production processes, energy generation and usage. However, while initiatives in the electricity generation sector have yielded good results, progress in the heating and cooling sector has been slower. According to Eurostat [1], in 2022, renewable solutions accounted for only 24 % of the total final energy consumption in these sectors within the EU.

The 2018 Renewable Energy Directive, strengthened in 2023[2], mandated an increased policy prioritization of the sector to accelerate the diffusion of renewables, aiming for a 1.1% annual increase in each EU country, both in district heating and traditional heating and cooling. An increasing population and higher living standards contribute to greater energy demand. Additionally, due to heightened awareness of climate change, other essential energy requirements—such as low environmental impact, reliability, and affordability—have become more prominent. For these reasons, heat pumps, especially when powered by low-emission electricity, are considered central to the global transition to secure and sustainable heating [3]. Considering the national fuel mix [4], a portion of the electrical energy required by electrically driven heat pumps is produced from renewable primary energy sources. This makes heat pump integration crucial in transitioning to more sustainable space and water heating systems in both residential and non-residential applications.

1.1 Heat pump technology

The purpose of a heat pump is to increase and maintain the temperature of an ambient by extracting the heat from a source at a lower temperature. To do this, according to the second principle of thermodynamics, it is necessary to spend some additional work. A heat pump is thus a heating system that transfers thermal energy from a cold sink to a hot sink by spending mechanical energy in a compressor. The theoretical reference of the vapor compression cycle

is the Carnot inverse cycle, in which the fluid carries out four reversible processes in four components:

Evaporator: a/b - Isothermal expansion, Q_2 absorbed

Compressor: b/c - Isentropic compression, E supplied

Condenser: c/d - Isothermal compression, Q_1 rejected

Expansion device: d/a – Isentropic expansion, without any heat transfer

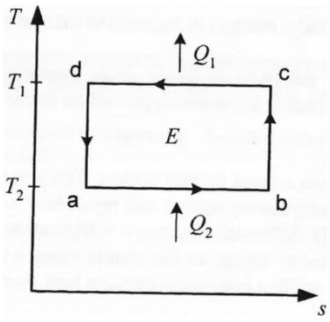

Figure 1.1 – Carnot inverse cycle [5]

The heat Q_1 exchanged in the condenser is called **heating capacity** and it is used to evaluate the performance of the cycle through the **coefficient of performance** (COP), ratio between the heating capacity and the compression work

$$COP = \frac{Q_1}{P} \tag{1.1}$$

However, due to some unfeasible practical requirements the Carnot cycle can be used only as a reference cycle, and thus the Carnot COP represents the ideally maximum possible COP, depending only on the cycle temperature:

$$COP_C = \frac{T_2}{T_1 - T_2} \tag{1.2}$$

This expression shows that to increase the performance of the ideal cycle it is sufficient to increase the evaporating temperature while keeping the condensing temperature constant, resulting in a decrease of the compression work. This concept also applies to real thermodynamic cycles. Therefore, a solution for performance increase can be the use of a solar-air dual source heat pump (SAHP). In this system, solar radiation is exploited by a solar thermal collector which increases the temperature of the heat sink, leading to a higher evaporation temperature. This option represents an innovative way of exploiting solar energy for thermal

purposes, as it allows the low solar energy available in winter to evaporate the refrigerant, potentially increasing performance compared to an air-source heat pump system. This option addresses the main issue with solar thermal energy exploitation, where solar thermal collectors alone cannot meet user needs in winter due to insufficient solar radiation.

While the concept of using solar energy directly for heating dates back to ancient civilizations, the development of modern solar thermal energy systems began in the 1900s Research on solar evaporators started with the pioneering work of Sporne and Ambrose in 1955 [6]. The combination of solar energy with heat pump technology began to attract attention during the 1970s, when the oil crisis sparked significant interest in alternative and renewable energy sources. In the following decades, research developed around two types of SAHPs:

- **Indirect solar-assisted heat pumps** (IDX-SAHP): a secondary fluid (water or water+anti-freeze substance) is heated up by solar collectors and then it is sent to a storage tank. The evaporator of the heat pump absorbs the heat from the fluid stored inside the tank.
- **Direct solar-assisted heat pumps** (DX-SAHP), where the solar collector directly acts as the evaporator, evaporating the refrigerant thanks to the heat provided by the solar radiation, without any secondary circuit.

Direct solar-assisted heat pump technology is particularly interesting: the refrigerant is more suitable for circulation in an outdoor system, avoiding potential corrosion from water in pipes and extending the device's lifespan. due to the passage of water in pipes, extending the device's lifespan. Additionally, refrigerants have much lower freezing temperatures than water, preventing freezing issues.

Growing environmental awareness has driven a gradual increase in the market penetration of SAHPs, primarily for residential systems but also for some small commercial applications. In recent years, PV modules have been increasingly used to power heat pumps, reducing dependence on grid electricity. Over the last two decades, significant improvements have been made in technology, focusing on optimizing system performance through better controls and adaptive functioning based on weather conditions and user demands. Future prospects involve the integration of IoT (Internet of Things) for efficient monitoring and control, and their incorporation into smart grids. As net-zero energy buildings become more common, SAHP

systems are expected to diversify and extend into larger commercial buildings and industrial processes.

A study by Tao et al. [7] identified solar-assisted heat pump systems as the most suitable among six other solar-assisted heating systems. The main heating devices currently found in residential units are gas boilers, heat pumps and electric heaters. Incorporating a solar collector helps reduce the carbon footprint of each heating system studied, but solar-assisted heat pumps demonstrated the highest solar fraction and heating COP. The solar fraction (SF) is expressed as the ratio between the net thermal energy delivered by the solar collector (collected energy Q_{av} minus losses Q_{lo}) and the heating demand Q_{hd} of the building.

$$SF = \frac{Q_{av} - Q_{lo}}{Q_{hd}} \tag{1.3}$$

The SF and heating COP values reported by the authors are respectively 16.45 % and 3.55.

In a previous thesis work, the current state of the art of solar energy was analysed, identifying Photovoltaic-Thermal (PV/T) collectors as a promising technology for building more efficient heat pump systems that rely less on electricity from the grid, given the right environmental conditions. PV/T collectors serve a dual function: the photovoltaic cells generate electricity when exposed to sunlight, while the thermal component attached to the rear of the panels transfers heat to the refrigerant used in the heat pump system. This arrangement is particularly advantageous because it enhances the overall efficiency of the PV system by cooling the modules through the heat transfer process. In a solar PV cell, the conversion efficiency is inversely proportional to the operating temperature. Generally, only 15-20 % of the energy available in the solar radiation that reaches the PV cell is converted into electricity, while the remaining 80 – 85 % is lost in the form of heat. This led to PV cell cooling being a topic of research for years. The goal was that of seeking for a way to enhance the production of electric energy as well as collect the heat for secondary usage.

PV/T systems were first studied in 1978, starting from the idea of both air-cooled and water-cooled PV/T systems. Water has been found to cause corrosion problems, suggesting alternative solutions such as nanofluid-based collectors or the usage of PCM in solar collectors, as reported by Zhao et al. [8]. In the last decade, the impact of various nanofluids has been investigated, however this solution didn't reach the large-scale production due to the high cost of nanofluids. Alternatively, the introduction of PCM materials in the collector has been investigated. These

materials are commonly used as an efficient energy storage system for solar energy systems. Among many studies, paraffin wax slurry-based PV/T solar collectors have been investigated and significant performance improvements have been reported by Qiu et al. [9]. Another application is the usage of heat pipe cooling for PV/T systems, but due to complexity and issues related to the degradation of the heat transfer fluid inside them, they have been considered as uneconomical for PV/T systems, and the attention has switched to refrigerant based cooling systems. As reported by James et al. [10], the cooling effect provided by the refrigerant on the back of the PV module can decrease cell temperature up to 25 % compared to the PV system without cooling, under the highest tested irradiance, resulting in a 20 % increase of PV power output. The goodness of the cooling effect has also been found by Yang et al. [11] in the context of their numerical analysis of a PV/T coupled air-source heat pump.

PV/T solar-assisted heat pumps have proven to be advantageous compared to standard single-source heat pump systems, because of the higher thermal performance registered across multiple studies. These results are explained by the positive effect of the integration of the PV/T collectors in the heat pump. In this way, energy efficiency is improved by enabling the direct use of generated electricity to power the heat pump. Thermodynamically, this setup also enhances the evaporative capacity of the system when working in the simultaneous evaporation configuration, raising the evaporation temperature of the fluid, which in turn positively impacts the Coefficient of Performance (COP) of the inverse Carnot cycle. While in an air-source evaporator heat is delivered to the refrigerant at the air temperature (T_{air}), in the PV/T collector this temperature can be higher than T_{air}, reflecting in a higher evaporation temperature (T_{evap}). This reduces the difference $\left(T_{cond} - T_{evap}\right)$ resulting in an improved COP.

1.2 Dual-source configuration

As explained in §2.2, the goal of solar-air heat pump systems is to overcome the limitations of single source heat pump systems. A dual-source SAHP system can show an improved efficiency compared to traditional single-source systems, and produce heat with more stability, under varying environmental conditions. This aspect has been investigated by Cai et al. [12], that compared three configurations (solar-air series (SA-SHP), solar-air parallel (SA-PHP), air-solar series (AS-SHP)) both in steady-state and dynamic performance. The study explored the dynamic behavior and optimal working conditions of each proposed configuration, as well as evaluated the economic feasibility and the annual performance in different climatic regions.

Results show that the SA-PHP performs the best with a COP ranging between 4.50 and 4.58, followed by the AS-SHP (COP=4.39 – 4.50) and SA-SHP (COP=4.33-4.41).

The authors pointed out that, for increasing solar irradiance the relative contribution of the two evaporators switched in favour of the PV/T collector and showed to be the highest for the SA-SHP and the lowest for the AS-SHP. The reason for this is to be identified in the fact that at the outlet of the air evaporator the quality of the refrigerant is increased significantly compared to its inlet, resulting in a poorer heat transfer in the subsequent solar evaporator. In addition, when the solar irradiance rises above 500 W/m^2 the heat delivered by the air evaporator in the SA-SHP decreases to being lower than 0. This is because in the air-source evaporator the evaporation temperature achieved by the refrigerant in the SA system gets higher than ambient temperature, leading to a heat loss to the environment.

Chinnasamy et al. [13] conducted a numerical study on a dual-source solar-air heat pump system, examining its performance in three distinct operational modes: Natural Mode (NM), Forced Mode (FM), and Air-source Forced Mode (AFM). Their research, which assessed the system under varying climatic conditions and different water tank temperatures, determined the daily Coefficients of Performance (COP) to be 3.62, 3.37, and 3.05 for NM, FM, and AFM, respectively. The study delineates the dependency of the system's heat absorption capabilities on the intensity of solar irradiance, operating primarily through solar radiation in natural convection, switching to forced convection under reduced sunlight, and relying solely on air-source heat extraction in the absence of solar irradiance.

Numerous other literature studies (Simonetti et al. [14], Li and Huang [15]) demonstrate that a dual-source heat pump system can adapt and optimize its operation on a wide set of climatic conditions. This can be clearly identified by comparing the performance of the dual-source system with that of a single-source heat pump in the same conditions. This is what Deng et al. [16] studied experimentally a dual-source parallel heat pump system, comparing its performance to that of a single source solar heat pump. They proved that at low and medium solar radiation when both evaporators are working the heating time decreases up to 19.8 % and the COP increases by 14.1 %. Their study investigates also the effect of solar radiation and ambient temperature on the system performance as well as the refrigerant mass flow rate distribution in the system. In the study by Cai et al. already cited [12] the SA-SHP results suitable for working in an environment with low solar irradiation, AS-SHP performs better

when air temperature is low and solar irradiance is high and finally SA-PHP can achieve the optimal state at high ambient temperature or high solar irradiation.

The adaptability of dual-source solar-air heat pump systems highlighted by research studies is beneficial to operational efficiency, reflecting in energy savings and reduced environmental impact. Another crucial factor contributing to both the efficiency and environmental sustainability of these heating systems is the choice of the refrigerant. As the primary medium for heat transfer, the refrigerant significantly influences the overall performance and impact of the system. Therefore, selecting an appropriate refrigerant requires careful consideration of several key aspects.

1.3 Overview of CO_2 as refrigerant

Historically, commonly used refrigerants such as chlorofluorocarbons (CFCs) and hydrofluorocarbons (HFCs) prove to be extremely dangerous for the planet, since the first ones have a high Ozone Depletion Potential (ODP), causing the Ozone layer to decompose and exposing Earth to global warming, while the latter can have a considerable Global Warming Potential (GWP) compared to CO_2 having the reference value of GWP = 1. Following Montreal [17] and Kyoto [18] protocols in 1987 and 1997 phase out of these refrigerants has been introduced and attention has shifted to natural refrigerants such as ammonia and CO_2 or hydrocarbons such as propane. Apart from being less dangerous for the environment since they already exist in nature in the atmosphere, they also have good performances when working in the system. The adoption of low GWP refrigerants and the phase-down of the HFCs is today pushed by the recent regulations (Regulation No 517 of European Union of 2014 – and its new proposal, which is nowadays under review- and the Kigali Amendment of United Nations of 2016 [19]).

Environmental reasons are however not enough to justify the choice of a refrigerant, that also needs to satisfy numerous requirements. These characteristics can be collected in two groups:

- The refrigerant should not cause any risk of injuries in case of leakage.
- The chemical, physical and thermodynamical properties of the refrigerant must be suitable for the system and the working condition, at the lowest cost.

Generally, the most important criterion is the chemical stability within the refrigeration system, considering however that when released in the atmosphere, the refrigerant should decompose easily, without forming harmful substances. [5]

In the real thermodynamic cycle of a heat pump, several factors contribute to its efficiency beyond just the evaporation temperature. Practical cycles deviate from the ideal Carnot cycle due to unavoidable losses like de-superheating and throttling losses, which are forms of exergy losses. After compression, the refrigerant exits superheated and must lose enthalpy before it can condense, during which heat exchange occurs at a lower efficiency. Throttling losses occur because the pressure drop happens in a throttling valve rather than an isentropic expander, leading to inefficiencies. Efficiency is also impacted by factors such as the refrigerant's pressure drops and heat transfer characteristics, which affect the temperatures of evaporation (T_{ev}) and condensation (T_{cond}), reducing the overall temperature difference and efficiency of the cycle.

Attention has turned towards natural fluids for refrigeration, air conditioning and heating purposes. Natural refrigerants such as ammonia (R717) and carbon dioxide (R744) are substances that occur naturally in the environment and are used as cooling agents in refrigeration, air conditioning and heat pump systems. For example, carbon dioxide, as a refrigerant, has a global warming potential (GWP) of 1, making it a much more environmentally friendly option compared to traditional synthetic refrigerants like Freon-12, which has a GWP of 10.9. Carbon dioxide is particularly noteworthy as a natural refrigerant due to its low environmental impact and excellent thermodynamic properties. It is not harmful to the ozone layer having an ODP of 0, and it can come from industrial by-products, potentially increasing the recycling possibilities and delaying the release of this gas in the atmosphere.

Physically, CO_2 boasts a range of properties that make it suitable for heat pump applications. Its low kinematic and dynamic viscosity, combined with high thermal conductivity, allow to maintain efficient heat transfer even at low temperatures. CO_2's large heating capacity per unit volume (22,6 MJ/m^3 at 0 °C) is about 5 to 8 times greater than traditional refrigerants, leading to a more compact system design with smaller compressor and overall equipment. Finally, the small pressure ratio (about 2.5 – 3.0) and high ratio of liquid density to vapor density after throttling ensure an even distribution of the refrigerant in the refrigeration pipes, optimizing performance).

The chemical properties of CO2 also contribute to its viability and safety as a refrigerant. It is non-toxic, non-flammable, and chemically stable, not decomposing into harmful gases at high temperatures. Moreover, CO2 is inexpensive, widely available, and thus economically favorable. However, there are challenges associated with using CO_2, primarily due to its low critical temperature (31.1°C) and high critical pressure (7.37 MPa). These factors necessitate robust system components capable of handling pressures up to 10 MPa in a transcritical cycle, demanding higher design standards [20].

In light of the presented considerations, the chosen refrigerant for the heat pump system studied in this thesis is CO_2, due to its multiple advantages besides the obstacles. From the cycle performance side, CO_2 presents high HTC and low-pressure losses in the circuit. Despite having a low critical point, CO_2 working in transcritical cycle can provide high temperature lifts between evaporating and condensing temperature, making the fluid ideal for domestic hot water (DHW) applications.

It has been numerically demonstrated that CO_2 can provide a good performance increase (up to 30 %) compared to traditional R134a heat pump systems with proper cycle modifications or with a different heat source (SAHPs). Many studies have addressed the use of SAHPs using CO_2 as refrigerant: Leonforte et al. [21] assessed COP and seasonal performance, sharing a positive result on thermal and electrical efficiency of the system, as well as a maximization of seasonal performance and reduction of purchased electricity. According to Tammaro et al.[22], CO_2 performs better than propane in terms of heating capacity in low temperature applications, while roles invert at ambient temperatures higher than 8 °C. According to the author, the CO_2 is more adapted to produce sanitary hot water, since it performs with lower water inlet temperature, that is usually the case of water coming from the water network. In addition, this application allows to take advantage of the curve shape of the refrigerant inside the gas cooler.

Due to its high pressure in the circuit, the CO_2 can develop a high heat capacity, and its critical pressure is still not very far from the maximum pressure achieved in the system, meaning that the COP can also be high. Specific heat should be small in order not to achieve high losses in the expansion device.

In conclusion, CO_2's minimal environmental impact and superior thermal properties make it an ideal refrigerant for heat pumps used for DHW production and space heating (DH). Its use aligns with the principles of a circular economy, revaluing this by-product and contributing to

a more sustainable future. As we move towards greener alternatives, CO_2 emerges as one of the few refrigerants that can match the performance and eco-friendliness of category A1 refrigerants.

1.4 Seasonal performance

The space and water heating in buildings account for a significant portion of energy demand and CO_2 emissions. According to the IEA [23], these activities represent 45 % of total energy demand and 80 % of direct CO_2 emissions in buildings. Sanitary hot water production contributes significantly to this energy consumption, varying by building type. For instance, it ranges from 14 – 18 % in residential buildings to 7 – 17 % in healthcare and educational facilities, as reported by the U.S. Department of Energy [24].

The drive towards nearly Zero Energy Buildings (nZEB) in Europe, mandated for new constructions from 2020, has led to the adoption of new systems to increase the energy efficiency of existing buildings. This transition is coupled with a growing interest in natural refrigerants due to the F-gas regulation [19], prompting extensive research into the performance of natural refrigerants such as CO_2 and propane in heat pump systems.

Tammaro et al. [25] examined the water tank storage capacity required to meet user demand, comparing two different user profiles across three locations. Additionally, they highlighted the importance of proper stratification in maximizing system performance. Seasonal operation convenience of one heat pump over another was influenced by storage tank size, stratification, user demand profile and climatic conditions.

Velasco et al. [26] studied the effect of stratification in the storage tank, discovering that maintaining low vertical tank filling velocities ($v \approx 10^{-4}$ m/s) and low water flow rates between the tank and the heat pump gas cooler can increase the system's global COP by 12.4 % and reduce compressor energy consumption by 16 % compared to other strategies. Higher flow rates were found to increase thermal energy storage but also mixing, resulting in longer heating times and a decreased SCOP. Moreover, a higher temperature at the evaporator inlet increased the COP by up to 59% and reduced heating time by 40 %.

Tammaro et al. [25] conducted a comparative study on the seasonal performance of two 40 kW air/water heat pumps working with CO_2 and propane. This research, which examined different climates (Athens, Strasbourg, Helsinki) and user profiles (hospital and school), revealed that

the gas cooler capacity of the CO_2 heat pump is significantly influenced by the inlet water temperature. For instance, the capacity drops from 39 to 33 kW when the temperature increases from 5 to 25 °C. In contrast, the propane unit's capacity reduces to only 36 kW under the same conditions, indicating that stratification is much more important for the CO_2 unit.

Further investigation into the yearly performance of heat pump systems, specifically dual-source indirect SAHP systems, was conducted by Croci et al. [27]. Their study focused on the performance of such systems in Milan and Rome, highlighting that integrating a PV/T evaporator in dual-source mode can decrease electric consumption by 6 % and 12 % respectively, and reduce grid consumption by 29 % and 71 % respectively, compared to the air-source heat pumps with only PV systems and hybrid PV/T panels.

Botticella et al. [28] compared the performance of propane and R1234yf heat pumps in various building types (apartment block, office, school) and applications (fan coil, radiant floor panels). Their findings showed that propane heat pumps outperformed R1234yf units in all cases, with the most significant performance gap observed in fan coil applications in Helsinki, favoring the propane heat pump by 13.5 %.

The performance of CO_2 heat pumps under different external conditions ($T_{w,in}$: 16, 50 °C, T_{air}: -9, 19 °C) was analyzed by Trinchieri et al. [29] Their study, supported by a wide range of stationary tests, demonstrated that the COP of the CO_2 heat pump becomes competitive with high DHW demand when coupled with a stratified tank.

Wang, Belusko et al. [30] discussed the limitations imposed by current CO_2 reciprocating compressors, which have upper pressure and discharge temperature limits of 140 bar and 140 °C. They explored alternative compressors, such as scroll or turbo compressors, but noted that turbo compressors struggle with efficiency at high pressures, while scroll compressors suffer from significant leakage flow.

Chapter 2

Experimental Heat Pump System

2.1 Solar-assisted heat pump system

Dual-source heat pumps are being studied to overcome the limitations of single-source heat pump systems. In the experimental heat pump system at the University of Padova, this solution is adopted by the solar-assisted heat pump (SAHP) system studied in this thesis, a system in which the heat from the air temperature and solar radiation is exploited as the low-temperature thermal energy source for the fluid evaporation. For this purpose, a finned-coil heat exchanger evaporator and a PV-T evaporator are used, composed of three PV modules thermally coupled with a heat exchanger in which the refrigerant flows.

2.2 Experimental unit

The experimental system studied in this thesis is a dual-source solar-air heat pump working with CO_2 as refrigerant, located on the roof of the Department of Industrial Engineering at the University of Padova. This prototype has a heating capacity of 5 kW, used to heat water stored in two storage tanks of 200 L each. The heat pump system is equipped with two different heat exchangers at the evaporator:

1. **Finned coil heat exchanger:** External air is moved by a fan, which passes it through a coil in order to facilitate the evaporation of the refrigerant.
2. **PV-T evaporator:** The refrigerant is evaporated on the back of three PV modules, that exploit the solar radiation to produce electricity, while heat is dissipated by heating up the working fluid on a serpentine duct.

The schematic layout of the system is shown in Figure 2.1, where the three possible evaporation modes are shown:

- Air-mode
- Solar-mode
- Simultaneous-mode

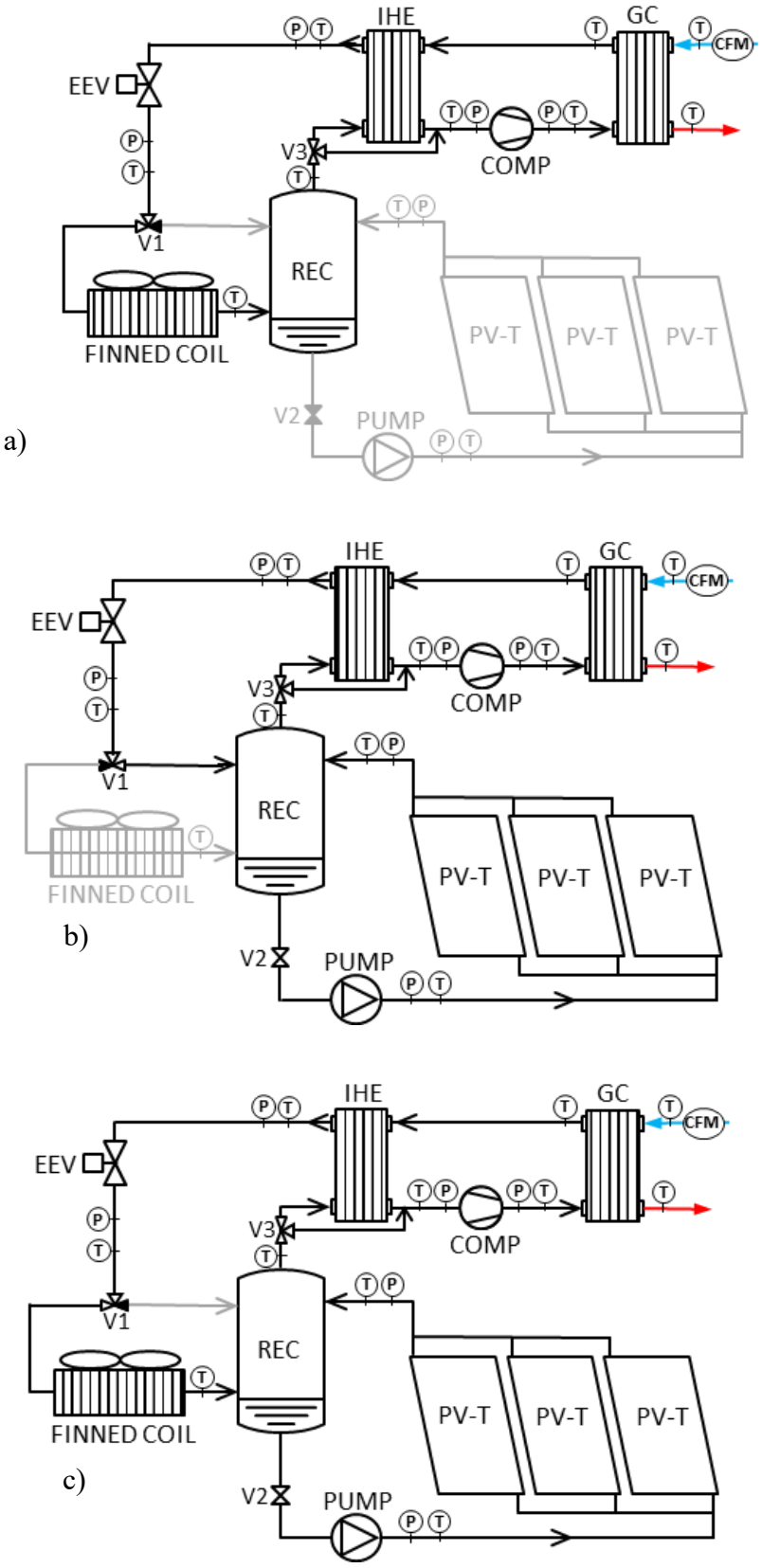

Figure 2.1 - Layout of the experimental system: a) air-mode, b) solar-mode, c) simultaneous-mode

2.3 System components

The system is composed by a multitude of devices. The refrigerant is compressed in a rotary compressor (COMP) produced by Toshiba (model DY30N1F-10FU). The compressor is inverter-driven with displacement equal to 3.02 $cm^3\ rev^{-1}$. Two brazed plate heat exchangers are used for two different roles: one acts as the gas cooler (GC), made of 28 plates (model SWEP B9HX28/18) where water is heated up, while the other one acts as the internal heat exchanger (IHE), made of 18 plates. The electronic expansion valve (EEV) is a CAREL E2V-09, operating as a backpressure valve to control the pressure at the gas cooler. Depending on the opening position of the valve V1, the refrigerant goes either in the finned coil heat exchanger (FINNED COIL) and then collects in the low-pressure receiver tank (REC) or it goes directly to the receiver. The finned coil heat exchanger has 4 circuits and a fan driven by a 0-10 Vdc signal to modulate the rotational speed. The low-pressure receiver tank is a liquid-vapor separator made by FRIGO MEC, from which two pipes depart. The first one includes the valve V2, that combined with value V1 defines the three operating modes of the machine. When V2 is closed, the heat pump works in air-mode, while when V2 is open, depending on V1 it may work in solar-mode or in simultaneous-mode. A solenoid valve at the bottom of the low-pressure receiver guarantees oil return. The pump (PUMP) extracts the refrigerant liquid through the three PV/T evaporators, a series of three 270 W modules coupled with a sheet and tube heat exchanger in which the refrigerant flows. The system is completed by a secondary loop for water circulation, in which a brazed plate heat exchanger is used to dissipate the heat and control water temperature at the gas cooler inlet.

Figure 2.1 highlights also the position of measurement sensors installed in the system:

- P: pressure gauge
- T: temperature gauge
- CFM: Coriolis flow meter

2.3.1 Solar collector PV/T

The three photovoltaic-thermal (PV/T) solar collectors consist of a polycrystalline silicon photovoltaic module, Solvis SV260-270, thermally coupled on the rear surface to a sheet-and tube heat exchanger through which the refrigerant flows. The module's rear surface is attached via a conductive paste to a 0.5 mm thick aluminum absorber plate and a copper tube with an internal diameter of 6 mm and a thickness of 1 mm, which is soldered to the aluminum plate.

The modules have no thermal insulation on the back: this is done to avoid overheating in summer, when the system is only used for electricity production since no heating is needed. Figure 2.2 presents the layer structure of the PV/T solar collector, while technical characteristics are reported in Table 2.1.

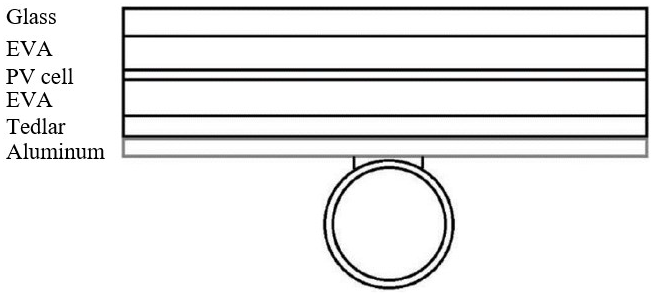

Figure 2.2 - Layer structure of the PV/T solar collector

Table 2.1 - Technical specifications of the PV/T collector's components

Photovoltaic Module		**Sheet and Tube Heat Exchanger**	
N° modules	3	**Absorbed plate material**	A1
Size	1650 x 992 mm	**Plate thickness**	0,5 mm
Inclination angle	45°	**N° tubes**	15
Type	Policrystalline Si	**Design**	Serpentine
Connection scheme	Series	**Tube material**	Cu
N° cells	60	**External tube diameter**	8 mm
Peak power	270 W	**Tube thickness**	1 mm
Temperature coefficient	0.005 %/K	**Tube pitch**	80 mm

2.3.2 Finned coil heat exchanger

The air-source evaporator consists of a finned coil unit with a fan, model SHVN 9/5 H – EC FAN by LUVE Exchange. The fan is equipped with EC (Electronically Commutated) technology, which helps to reduce energy consumption. Additionally, it features an integrated control system, with an input signal ranging from 0 – 10 Vdc, allowing for the modulation of the fan's rotational speed to match the thermal load requirements. Main technical specifications provided by the manufacturer are listed in Table 1.2.

Table 2.2 – Technical specifications of the finned coil heat exchanger's components

Finned coil		**Fan**	
Model	SHVN (3,2 mm) 9/5	Model	EC FAN
Size	753 x 520 x 906 mm	Size Ø	350 mm
Weight	28 kg	N° fan	1
N° circuits	4	Connection	230 V 1 - 50 Hz
Circuit volume	4,4 dm3	Rotational speed	Cu
Circuit area	15.3 m2	Air flow rate	8 mm
Tube material	Cu	N° poles	1 mm
Fin material	Al	Motor consumption	180 W
			0,85 A

2.4 Transcritical cycle

The CO_2 operates a transcritical cycle. From the low-pressure liquid receiver, the CO_2 gas is extracted from the top and, after being preheated in an internal heat exchanger, it is compressed to a higher pressure by the compressor. The CO_2 superheated vapor produces the required heat by heating water while being cooled down in the gas cooler, a brazed plate heat exchanger with 28 plates. The CO_2 gas is further cooled down in the internal heat exchanger (IHX), a brazed plate heat exchanger with 18 plates, where the incoming gas is preheated. In this device, the hot CO_2 stream increases the temperature of a fraction of the CO_2 gas-stream exiting the liquid receiver, to control the superheating degree. The two refrigerant heat flow rates through this device are regulated by the three-way valve.

The high-pressure side completes with the passage through the electronic expansion valve (EEV), that acts as a back pressure valve to control the pressure at the gas cooler. On the low-pressure side of the cycle, the evaporation mode can be chosen, however in this thesis the focus will be on the simultaneous-mode, that will be described in the next paragraph.

In air-mode, (Figure 2.1(a)) after the EEV all the refrigerant mass flow rate goes through the finned coil evaporator, where the heat provided by the air, increased by the forced convection realized by the fan work, makes the refrigerant evaporate. At the evaporator outlet, the refrigerant is collected in the receiver tank, from which it is sent to the IHX and then to the compressor, closing the cycle. In this configuration, the valve V1 is open in dry expansion mode, while the valve V2 is completely closed. The finned coil heat exchanger has 4 circuits and the fan is driven by a 0-10 Vdc signal to modulate the rotational speed.

In solar-mode (Figure 2.1(b)), after the passage through the EEV the refrigerant directly collects in the tank receiver. From here, the collected liquid CO_2 is pumped from the bottom of the tank through the PV/T evaporator, where the solar irradiance heats up the PV modules, and part of the heat is dissipated by evaporating the refrigerant that runs in the serpentine attached to the back of the panel. At the PV/T collector outlet, the refrigerant collects back into the receiver tank, from which the gas from the top is extracted and directed to the IHX and the compressor. In this configuration, the valve V1 is open in flooded evaporator mode, while the valve V2 is open.

In the simultaneous working solution, the liquid CO_2 coming from the EEV will first evaporate in the finned coil heat exchanger, it will collect in the receiver at a height of 1.7 m, from which a liquid line will depart to bring the liquid through a pump to the solar PV-T evaporator. The evaporator in this way described is presented as a simultaneous evaporator more than a series one. The evaporation happens in series, however the exploitation of the gas happens simultaneously for the gas coming from the evaporation in the finned coil heat exchanger and the PV-T system.

In all the configurations the refrigerant goes back to the receiver after the vaporization process.

Heated water is collected in a first 200 L water storage tank (TANK2), from which heat is delivered to the brazed plate heat exchanger. The second water tank collects cold water to be heated by the heat pump system. This tank is equipped with four 4.5 kW electric heaters to control the temperature of the water at the inlet of the gas-cooler (TANK1). Figure 2.4 highlights the presence of a by-pass valve for flow regulation in the heat exchanger as well as two valves placed before and after the user to stop the system supply if no thermal energy is needed.

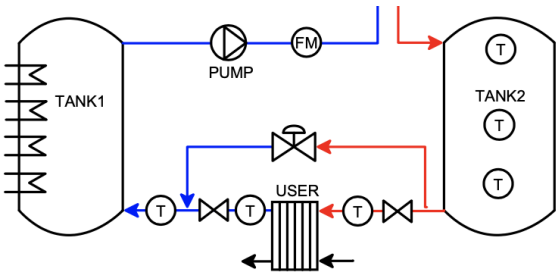

Figure 2.4 - Water circuit with circulation pump, user BPHE and two tanks for hot and cold water

2.5 Measurement system

Figure 2.1 shows also the measurement instrumentation installed in the experimental apparatus: T temperature sensors, P pressure sensors, CFM Coriolis flow meter. The measurement system is composed as follows:

- 8 pressure gauges:
  1. 6 measure the relative pressure at the inlet/outlet of the main system devices
  2. 2 measure the pressure difference between precise points of the circuit. The first one measures the pressure drop between the extremes of the finned coil heat exchanger, the second one the liquid level in the low-pressure receiver. Regarding the air temperature, the RTD has been positioned close to the inlet section of the finned coil evaporator and shielded by the direct component of the solar radiation.
- 45 temperature gauges:
  1. 3 RTD-Pt100 to evaluate environmental air temperature and water temperature at inlet/outlet of the gas cooler. In the water circuit, RTDs are placed inside thermowells in direct contact with the water flow.
  2. 42 thermocouples distributed as follows:
     a) 3 at inlet/outlet of each solar panel
     b) 25 on the back side of the PV/T, used to build the temperature profile of the refrigerant in the evaporator. This profile is useful to identify potential overheatings or a variation of the heat transfer coefficient, as well as the surface temperature

  c) The remaining ones are placed at the inlet/outlet of the remaining main system devices.

The thermocouples are T-type units positioned on the external side of the pipes (under the insulation material) and they use a heat sink compound to have an optimal thermal contact. Each thermocouple was calibrated against 1/10 DIN platinum thermal resistance detectors (Pt100 with accuracy $\pm$ 0.03 K) before the beginning of the experimental campaign.

- A Coriolis-type water flow meter measures the water mass flow rate in the gas cooler.
- 3 pyranometers have different purposes:
  1. Installed in the horizontal plane to measure the global irradiance on that plane.
  2. Installed in the horizontal plane with a shading band, to measure the diffuse irradiance on that plane.
  3. Installed on the collector plane to measure the global irradiance on the inclined surface.
- One anemometer measures wind speed

Data acquired by these devices is collected by a data acquisition system, the Agilent 34970, to which the entire measurement system is connected. This device is equipped with three reading cards acquiring each 22 input signal, the first 20 of which are used for reading voltage signals while the remaining two read the current signals (Coriolis, anemometer and pressure gauges). Therefore, the Agilent system acquires six current signals only, requiring some of the pressure gauges current signals to be converted into voltage signals.

The electric power required by the compressor and by the heat pump (respectively "Compressor power P_{comp}" and "General power P_{gen}"), as well as the power produced by the PV system P_{pv}, is measured by the power analyser Norma 4000.

Compressor power affects the performance of the cycle, since it represents the main contribution in the power consumption. Therefore, to improve the system's efficiency it is of greatest interest to limit the power consumption. That's what James et al. [10] tried to achieve, by implementing a feedback-controlled variable frequency detector for the compressor unit, that optimizes the compressor frequency based on the evaporator load conditions.

2.6 Control system

2.6.1 Control on the operation parameters

The heat pump system operation is controlled by three potentiometers, each regulating the voltage (0 – 10 V) that powers three components: compressor, EEV, fan. The purpose of the control system is multiple. One controls the compressor speed, that can range from still (0 V) to the maximum speed (10 V) with a linear increase. The electronic expansion valve controls instead the hgh pressure of the system. At 4 V the high pressure is equal to 80 bar, for higher voltage the pressure increases by 2.5 bar/V, with a maximum of 95 bar when V = 10 V. When the voltage is set at 2 V, the high pressure in the system is instead 78 bar. Finally, fan velocity linearly varies between 0 and 100 % with the voltage (0 – 10 V).

2.6.2 Control on the thermal power produced

The experimental tests, both in steady state and dynamic conditions, required a focused control of the conditions of the water entering and exiting the gas cooler. It is important to keep fixed values throughout the test, despite changes in external conditions. To regulate the temperature of the water entering the gas cooler, two storage tanks were used, each with a capacity of 200 L, connected to each other. In one of the tanks, three electrical resistances of 4.5 kW each were switched on to heat the water entering the gas cooler at the desired temperature. The water in the cold tank is fixed and kept constant by ensuring that the hot water coming back from the gas cooler and stored in the TANK 2 is made to pass through the brazed plate heat exchanger, where heat is dissipated.

To control the temperature lift at the gas cooler and choose the outlet temperature of the system, to be kept constant, it is necessary to act on the mass flow rate regulation valve. By changing the opening of the valve, the mass flow rate $\dot{m}_w$ is varied.

$$Q_{gc} = \dot{m}_w * c_p(T_{w,out} - T_{w,in})$$

Considering a constant thermal power produced in the gas cooler, Equation 1.1 shows that when the water mass flow rate is varied, the temperature lift varies as well. Therefore, fixing the $T_{w,in}$, $T_{w,out}$ changes. The flow rate was adjusted manually by acting on a regulation valve positioned before the entrance to the gas cooler.

A similar procedure has been adopted in one dynamic test, carried on the 21/02/2024, to realize a variable water temperature lift while keeping $T_{w,out}$ constant. Starting from an initial inlet water temperature, the water mass flow rate has been reduced to achieve the required $T_{w,out}$. At this point, the electric resistances in the cold tank have been switched on, and the water flow rate has been varied to keep $T_{w,out}$ constant, despite the increasing inlet temperature.

2.6.3 Control on the electric power produced

The power produced by the PV system is dissipated through a wirewound rheostat, made of three toroidal resistors of 67 Ω each, connected in parallel. The rheostat simulates a variable electric load, and it is manually adjusted to operate at the maximum power point (MPPT), despite the varying environmental conditions.

Chapter 3

Experimental Campaign

The data presented and analysed in the following chapter have been collected in the fifth experimental campaign, between 12/2023 and 02/2024. Additionally, data collected in the previous experimental campaigns will be used to highlight some performance comparisons. Data have been collected with the power control and measurement system described in the previous chapter. The simultaneous operation mode will be the focus of this thesis, since as described before it has been proven as the one realizing the best performance.

A set of 30 experimental tests have been collected in different environmental and external conditions, extending the set of experimental data collected in previous campaigns. Tests have been carried out both in form of steady-state measurements, with constant external conditions, and dynamic state, describing the behavior of the heat pump system in variable environmental conditions with a test lasting two hours.

The heat pump performance is influenced by many parameters, of which the most important ones are:

- Air temperature
- Solar radiation
- Inlet water temperature at the gas cooler

To get a proper description of the heat pump's performance it is required to collect experimental data under a wide set of external conditions. Only in this way in fact, it will be possible to have a glimpse at how the heat pump could perform when working for a longer period in dynamic conditions, for example considering a seasonal operation scenario. This has been the aim of the experimental campaign studied in this thesis and it has been followed also in the cited paper [16], where the authors investigated the heat pump's behaviour across a range of air temperature and solar irradiance, respectively between 10 °C to 30 °C and 100 to 700 $\frac{W}{m^2}$.

A variation of the air temperature will reflect in a modified response of the finned coil evaporator, slightly affecting also the PV/T evaporator. A variation of the solar radiation will

have effect on the performance of the PV/T evaporator, and thus substantially impacting the performance of the heat pump system. In this work, focus has been given also to the inlet water temperature at the gas cooler: it has been seen that this parameter's operative range may represent a limit that depends on the heat pump system's configuration. Experimental data is classified in an organic way, highlighting the different conditions in which tests are carried out. Heat pump's performance will also depend on machine parameters such as fan and compressor frequency and opening of the EEV, that controls the high-pressure level.

Since this year's campaign started earlier in winter compared to last year's, it has been possible to collect data at lower environmental temperature and solar irradiance conditions. In future works it would be interesting to extend this set of data even further, studying the behaviour at even lower environmental temperatures; however this has not been possible due to the location of the heat pump.

3.1 Data reduction

As previously mentioned, two categories of experiments have been conducted:

1. Steady-state analysis
2. Dynamic analysis

In the first group of experiments the main goal is the definition of the performance of the heat pump given fixed environmental and system parameters. Steady-state condition is reached when there are no temperature and pressure variations inside the circuit while the system is working. It is required that the boundary conditions, such as environment and operation set-up of the system, remain constant through the test acquisition. Each 10 seconds LabVIEW acquires measured data for a total of 31 values per each test, covering a period of 5 minutes. The average value of these 31 measurements corresponds to the measured steady-state point.

The dynamic measurements lasted 2 hours, and the only parameters remaining fixed are system parameters, such as compressor power, lamination valve opening and fan speed, as well as the temperatures of the water entering and exiting the gas cooler. After fixing the initial steady-state point, all the values measured are collected as single points that will be useful to analyse the parameter trend in the following.

Dynamic condition is instead the transitory state in which the machine operates when boundary conditions change. The machine adapts to these modifications and tries to reach a new steady-state point. In dynamic test measurements, each collected value represents a point of the dynamic test. Also in dynamic condition, points are acquired every 10 seconds. Acquired data are then analysed through a MATLAB script to evaluate different thermodynamic properties. These values are then printed on a Excel file. The most important parameters are reported below.

1) Heating capacity at the gas cooler

$$Q = \dot{m}_w * c_{p,w} * \left(T_{out,w} - T_{in,w}\right) \tag{3.1}$$

where $\dot{m}_w$ [kg/s] is the mass flow rate of water through the gas cooler, $c_{p,w}$ [J kg^{-1} K^{-1}] is the water specific heat and $T_{out,w}, T_{in,w}$ are respectively the outlet and inlet water temperature.

2) Evaporating temperature

$$T_{evap} = refprop(p_{evap}, x = 1) \tag{3.2}$$

The evaporation temperature is evaluated with REFPROP from the evaporating pressure, experimentally measured in the system, and imposing a unitary vapor quality.

3) Superheating at the compressor suction

$$SH = T_{in,comp} - T_{evap} \tag{2.3}$$

where $T_{in,comp}$ is the refrigerant temperature at compressor suction.

4) Refrigerant mass flow rate

$$\dot{m}_{ref} = \frac{Q_{gc}}{h_2 - h_3} \tag{3.4}$$

where h_2, h_3 [J/kg] are respectively the enthalpy of the refrigerant at the inlet and outlet of the gas cooler.

5) Evaporating capacity

$$Q_{evap} = \dot{m}_{ref} * (h_x - h_5) \tag{3.5}$$

where h_x, h_5 [J/kg] are respectively the enthalpy at the receiver and lamination outlet.

6) Coefficient of performance calculated with respect to the compressor power and total power

$$COP_{comp} = \frac{Q_{gc}}{P_{comp}} \tag{3.6}$$

$$COP_{gen} = \frac{Q_{gc}}{P_{tot}} \tag{3.7}$$

where P_{comp} [W] is the power consumption of the compressor while P_{tot} [W] also consider additional power consumption, as indicated by Equation 2.8

$$P_{tot} = P_{comp} + P_{pump} + P_{fan} + P_{aux} \tag{3.8}$$

This results in COP_{comp} being always higher than COP_{gen}.

Measurement systems are, however, not perfect, and each measured data brings with itself an uncertainty level and a confidence interval. The chosen confidence interval defines the probability that the value measured data falls into the confidence interval itself. This can be seen as an error in the measurement, that depends on a systematic and on a casual component. Quantifying this error is crucial for a proper data interpretation. Systematic components act in the same way in multiple measurements and depend on the characteristics of the measurement instruments. Therefore, they can be solved by properly calibrating the instrument. Regarding the casual effects, they depend on non-predictable variations on the measured quantity, they act in a different way at each measurement and therefore they can't be correct. However, repeating a measurement multiple times can limit its impact. In this thesis, repeating 31 times each measurement allowed to evaluate the uncertainty related to a confidence interval of 95 %. The combined uncertainty takes into account of two different types of uncertainty.

Type A uncertainty is estimated by statistical inference from the known experimental sample, of which the sample mean is calculated:

$$\overline{X_n} = \frac{1}{n}\sum_{i=1}^{n} X_i \tag{3.9}$$

as well as the sample variance

$$S_n^2 = \frac{1}{n-1}\sum_{i=1}^{n}(X_i - \overline{X_n})^2 \tag{3.10}$$

where n is the number of elements in the sample. The type A uncertainty results as

$$U_A = t * \sqrt{\frac{S_n^2}{n}} \tag{3.11}$$

where t accounts for the 95% confidence level and is the inverse cumulative distribution function of the t-Student probability distribution, that is chosen because the number of samples for each test in steady state is small, n=31.

Type B uncertainty is estimated from previous knowledge, in this case technical specifications given by the manufacturer. Based on the GUM [31], type B uncertainty is in this work calculated for the complete ignorance case:

$$U_B = k * \frac{half-width}{\sqrt{3}} \tag{3.12}$$

with k=2 for a confidence level of 95 %.

- Thermocouples: ± 0.1°C;
- RTD temperature sensors of 1/10 DIN type: 0.0009·T[°C] + 0.0249;
- Pressure gauges:
  a) 0.1% of full scale for both relative and absolute pressure gauges;
  b) 0.12 kPa for differential pressure gauges;
- Coriolis flow meters: 0.1% of the reading;
- Power measured by Norma 4000:
  a) $half - width = 2\sqrt{3} \cdot \sqrt{(i(V)^2 + i(I)^2 + i(\omega)^2)}$ (3.13)
  b) i(V) voltage uncertainty calculated as 0.1% of the average of readings
  c) i(I) current uncertainty calculated as 0.025% of the average of readings
  d) i(ω) angular velocity uncertainty calculated as 0.01% of the average of readings. This value is disregarded because it is very small.

The two uncertainties are taken into account to evaluate the combined uncertainty as

$$U_C = \sqrt{U_A^2 + U_B^2} \tag{3.14}$$

Measured data have been used to evaluate other variables not measured experimentally, therefore the error propagation through the calculation should be properly estimated started from the calculated uncertainties.

3.2 Experimental tests in simultaneous mode

Characteristics of experimental tests carried out this year are presented and described in the following.

The tests have been performed in various operating conditions. A voltage is set on the potentiometer associated with the compressor, chosen among the values 4 – 5 – 7,5 – 10, corresponding to a speed of 40 – 50 – 75 – 100 % relative to the nominal speed. Another potentiometer regulates the opening of the expansion valve, through a varying voltage chosen among the values 2 – 4 – 6 – 8 – 10 V, corresponding to high pressure of approximately 78 – 80 – 85 – 90 – 95 bar. When the heat pump operates in air-mode and simultaneous-mode, a potentiometer regulates the fan velocity, with a voltage value chosen between 2,5 – 5 – 7,5 – 10, corresponding to a fan speed of 25 – 50 – 75 – 100 % relative to the nominal speed.

In the simultaneous evaporator configuration, 30 experimental tests have been performed, further expanding the range of experimental data collected in the previous year, which was lacking tests at:

- Higher compressor speed
- Higher gas cooler pressure
- Lower ambient temperature
- Lower water inlet temperature

In addition, the range of solar irradiance and air temperature has been extended to lower values. The previous experimental campaign has been characterised by tests mostly at high solar irradiance and air temperature values. In these situations, the beneficial effect of the PV/T collector is enhanced, however when the solar irradiance decreases, this effect decreases as well. By extending the range of experimental tests to lower values, it has been possible to extend the study of the simultaneous configuration to less favourable environmental conditions.

Finally, multiple tests have been done in the simultaneous configuration with different values of inlet temperature of the water at the gas cooler. This aspect is important, since the heat pump's performance depends directly on the inlet water temperature. Therefore, it has been studied both in steady-state and dynamic conditions.

3.2.1 Water temperature difference effect

In this year's experimental campaign, the goal of some tests has been that of investigating the effect of the high temperature difference between outlet and inlet water and the effect of the low inlet water temperature when the heat pump operates in simultaneous-mode. These conditions affect the energy balance and thus the heat transfer at the gas cooler.

Figure 3.1 shows the effect of the water temperature differences at the gas cooler on the COPs of the heat pump in simultaneous-mode. Test conditions are:

- Compressor speed 100 %;
- Fan speed 50 %;
- High pressure level: 85 bar;
- Air temperature: 10 °C ± 0.5 °C
- GTI: 820 W/m^2 ± 15 W/m^2
- Water inlet temperature: 31 °C ± 0.5 °C

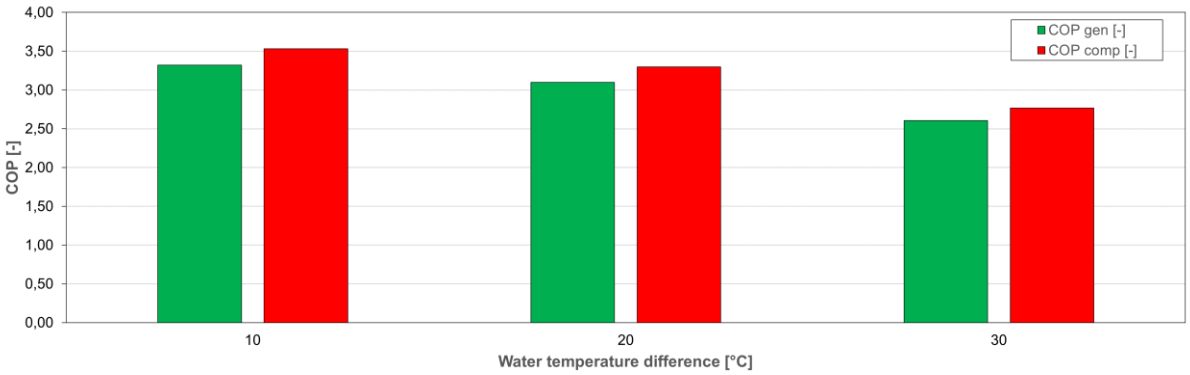

Figure 3.1 - Test performed with GTI = 820 ± 10 W/m^2, T_{air} = 10.2 ± 0.5 °C, $T_{w,in}$ = 31 °C ± 0.5 °C

A higher temperature difference between inlet and outlet leads to lower COP.

The higher temperature difference at the gas cooler is achieved through a reduction of the mass flow rate of water. Let's consider the thermal power produced by the gas cooler, expressed with Equation 2.1, If we suppose to keep the same produced thermal power but realize a higher temperature lift between water inlet and outlet, it is required to decrease the mass flow rate of circulating water through the heat exchanger.

$$Q = \dot{m}_w * c_p * (T_{w,out} - T_{w,in}) \quad (3.15)$$

Results show that increasing the temperature difference decreases the COP of the machine. This is related to various effects. First of all, the superheating level at compressor outlet is strongly affected. Its value increases when the water temperature difference increases. In addition, the pressure ratio decreases as the water temperature difference increases. This happens because the outlet pressure remains the same, while the inlet pressure increases because of the higher temperature reached by the refrigerant in the evaporator. So, while the compressor power doesn't vary significantly due to the pressure ratio remaining roughly the same, the gas cooler power decreases as the temperature difference increases. In fact, the higher superheating level means that a higher portion of the gas cooler will be exposed to a less efficient heat exchange process.

Table 3.1 – Results comparison between three tests in simultaneous-mode with high water temperature lift at the gas cooler

dT [K]	T [°C]	G [W/m^2]	COP_{gen} [-]	COP_{comp} [-]	SH [K]	rp [-]	P_{comp} [W]	Q_{gc} [W]	T_{ev} [°C]	T_{air}-T_{ev} [K]
10	10.71	817	3.32	3.53	13.2	2.33	1493	5272	1.97	8.74
20	10.07	823	3.10	3.30	16.0	2.29	1481	4884	2.58	7.49
30	9.74	827	2.60	2.77	20.1	2.23	1470	4068	3.70	6.04

3.3.2 Air temperature effect

The effect of air temperature on the system's performance in simultaneous-mode can be shown for a broad set of temperatures. A different air temperature affects the performance of the fin coil heat exchanger, and in lower measure that of the PV/T system, resulting in a modification of the COP of the system. This effect is shown in Figure 3.8, in the following steady state conditions:

- Compressor speed 50 %;
- Fan speed 40 %;
- High pressure level: 80 bar;
- Water inlet temperature: 30.5 °C
- Water outlet temperature: 35.5 °C
- GTI: 790 $\frac{W}{m^2} \pm 50 \frac{W}{m^2}$

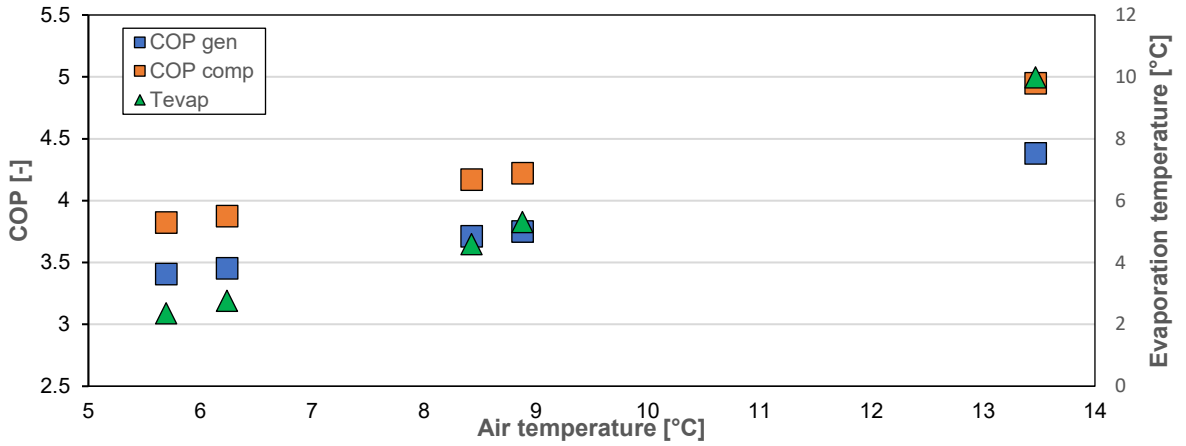

Figure 3.2 – Tezts performed with GTI = 800 W/m2, $T_{w,in}$ = 30.5 °C, $T_{w,out}$ = 35.5 °C

These results show that the higher the air temperature, the higher the COP, both referred to compressor power and to general power consumption. In fact, a higher air temperature increases the evaporation temperature of the refrigerant. This translates into a closer difference between evaporation and refrigerant temperature at gas cooler outlet, leading to an increase of the ideal Carnot cycle performance. In addition, this reduces the pressure ratio, leading to a lower specific power consumption by the compressor. These parameters are plot together in Figure 3.3.

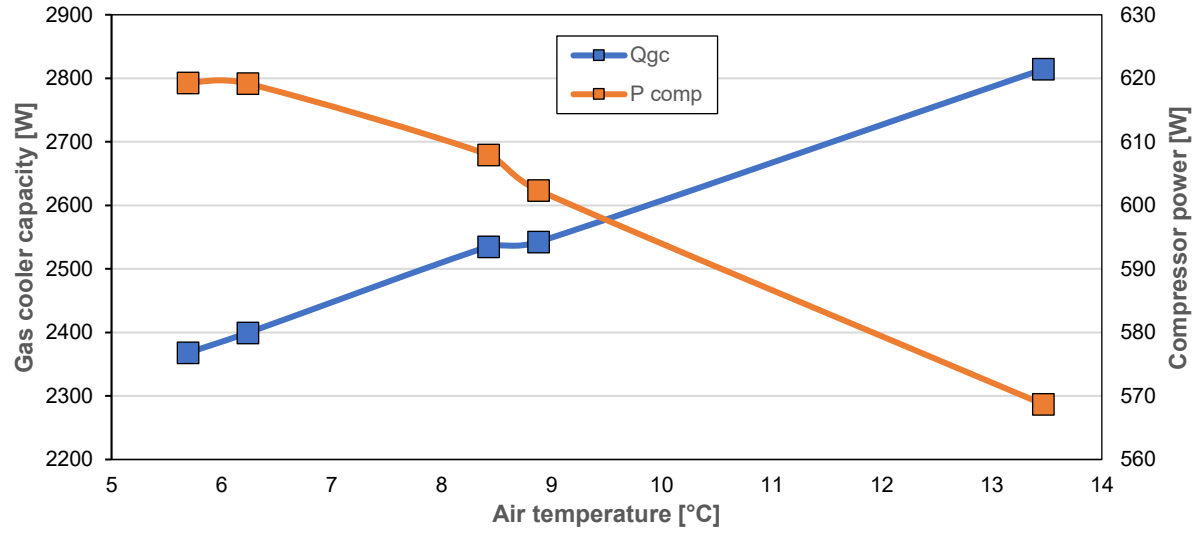

Figure 3.3 – Effect of the air temperature on the evaporation temperature and compressor power

Figure 3.3 shows that the P_{comp} decreases with an almost linear trend, at a rate of 1%/°C with the increase of the air temperature T_{air}. On the other hand, the evaporation temperature also follows a linear trend, increasing with T_{air} at a rate of approximately 1 °C per each °C increase of environmental temperature.

3.3.3 Solar irradiance effect

The intensity of the solar irradiance modifies the performance of the PV/T evaporator. The simultaneous-mode is however less exposed to the fluctuation of the solar irradiance, compared to the solar-mode system. Figure 3.4 compares the COP of the heat pump in simultaneous-mode between two different solar irradiance values. Test conditions are:

- Compressor frequency: 50 %
- Fan frequency: 50 %
- Higher pressure: 80 bar
- Air temperature: 8.8 °C ± 0,1 °C
- Water inlet temperature: 30.5 °C ± 0.2 °C
- Water outlet temperature: 35.5 ± 0.2 °C

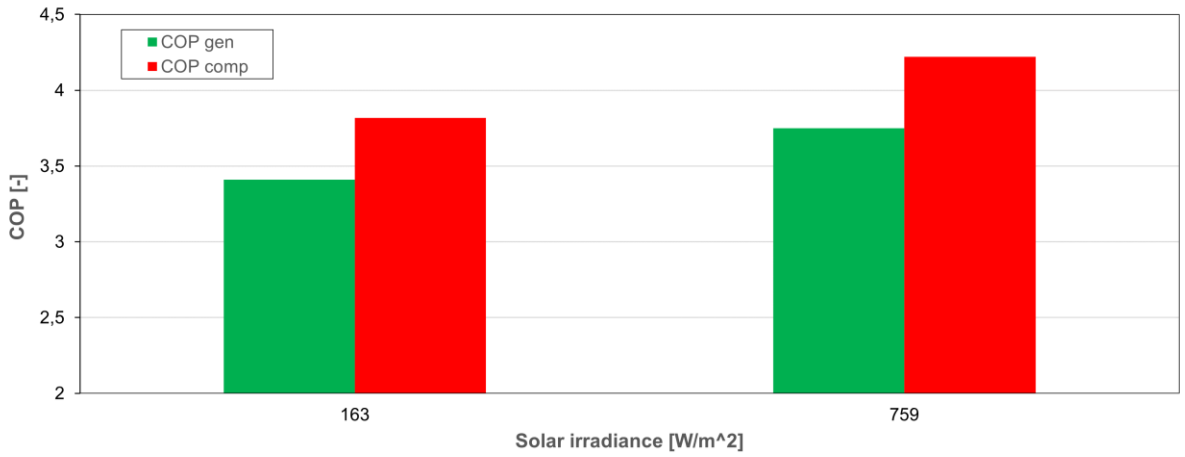

Figure 3.4 – Test performed with T_{air} = 8,8 °C, $T_{w,in}$ = 30,5 °C

The higher solar irradiance increases the heat flux at the PV/T evaporator, increasing the evaporation temperature and affecting positively the ideal cycle COP. Additionally, in this test the solar irradiance gets to a medium high value, however the power produced by the PV system is already sufficient to cover almost the whole heat pump consumption, increasing the energy savings. The COP increase is significant due to the higher GTI, coming at 9,9 % and 10,7 % for the COP_{gen} and COP_{comp} respectively.

Table 2.2 – Results comparison between two tests in simultaneous mode with low and medium solar irradiance

T_{air} [°C]	GTI [W/m^2]	T_{ev} [°C]	COP_{gen} [-]	COP_{comp} [-]	P_{PV} [W]	P_{gen} [W]	Q_{gc} [W]
8.83	163	2.31	3.41	3.82	23	697	2377
8,87	759	5.30	3.75	4.22	619	678	2543

3.3 Experimental test in air-mode

The following results compare three tests performed in air-mode with different temperature lifts on the water side:

- Higher pressure: 90 bar
- Compressor speed: 100 %
- Fan speed: 50 %.
- Water inlet temperature: 30 °C

Table 3.3 shows relevant results for comparing the three tests.

Table 3.3 – Results comparison between three tests in air-mode with high water temperature lift at the gas cooler

dT[K]	T_{air} [°C]	COP_{gen} [-]	COP_{comp} [-]	SH [K]	rp [-]	P_{comp} [W]	Q_{gc} [W]	T_{ev} [°C]	T_{air}-T_{ev} [K]
10	10.60	3.04	3.24	12.33	2.94	1600	5181	-4.75	15.34
20	9.68	2.82	2.97	12.1	2.8	1598	4745	-2.98	12.66
30	10.01	2.56	2.69	14.7	2.7	1595	4296	-2.08	12.09

Figure 3.5 compares the COPs of the heat pump in air-mode with different values of temperature lift at the gas cooler, when air temperature is about 10 °C.

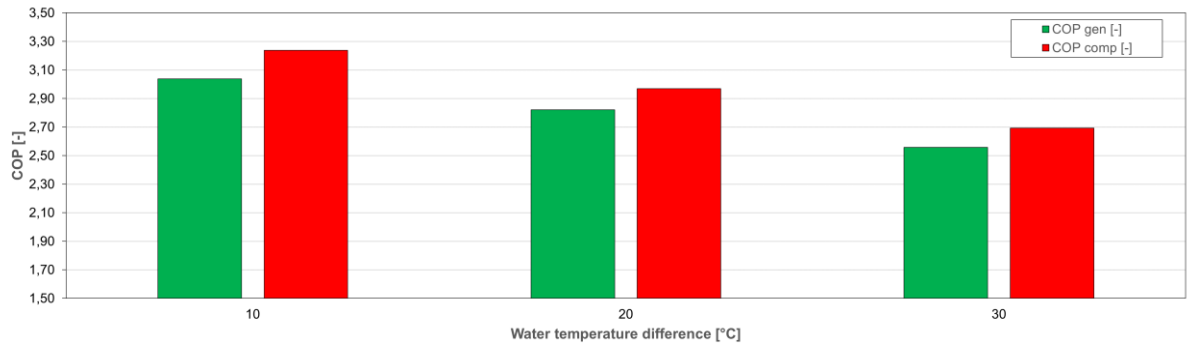

Figure 3.5 - COP comparison between three tests performed in air-mode with different water temperature lift at the gas cooler

Results show that the increase of water temperature difference at the gas cooler has a negative impact on the COP_{gen}, which decreases by 0.8 % per °C increase of water temperature difference. This is due to a decrease of the heating power produced at the gas cooler, influenced by the higher superheating at the compressor outlet, as shown in Table 3.3.

3.4. Comparison of the three evaporation modes

As already mentioned, the contribution of previous works has been that of identifying the simultaneous solution as the best performing one. This has been demonstrated in terms of evaporation temperature and COP under different varying parameters, such as solar irradiance, air temperature and fan speed. Similar results have been replicated by this year's experimental campaign. The following test has been carried out in similar external conditions, for the three machine configurations:

- Compressor speed: 50 %
- Fan speed: 50 %
- Higher pressure: 80 bar
- GTI = 850 $\pm$ 35 $\frac{W}{m^2}$
- Air temperature: 8,8 °C $\pm$ 0,2 °C
- Water inlet temperature: 31 °C $\pm$ 0.5 °C

Results are graphically shown in Figure 3.6, that compares the evaporation temperature achieved by the system in the three configurations.

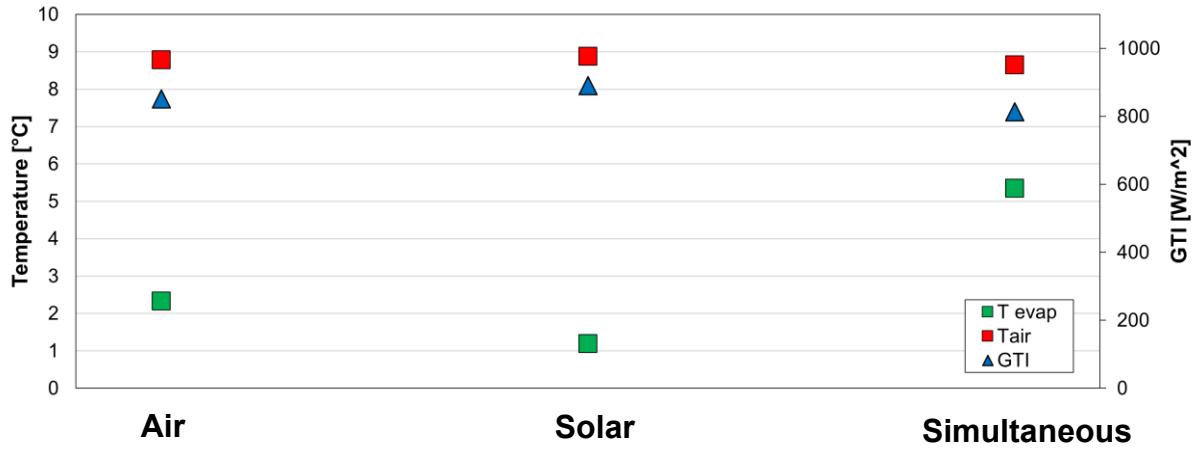

Figure 3.6 - Evaporating temperature comparison between air, solar and simultaneous-mode.

The simultaneous evaporation mode achieves an increase of T_{ev} equal to 3 °C with respect to the air-mode and of 4.2 °C compared to the solar-mode. This increase leads to a lower temperature difference between evaporation and refrigerant temperature at the gas cooler outlet, that reflects in a higher efficiency of the ideal Carnot cycle. In addition, the lower temperature difference determines a lower pressure ratio at the compressor, as shown in Table 3.4, that decreases the specific work done by the machine to compress the fluid. This factor also has a

positive effect on the COP, as shown in Figure 3.7. As a result, the registered COP_{gen} of about 3.77 in simultaneous-mode is about 6 % and 16.4 % compared to the air and solar-mode, increasing to 11.2 % and 22 % considering the $COP_{comp.}$

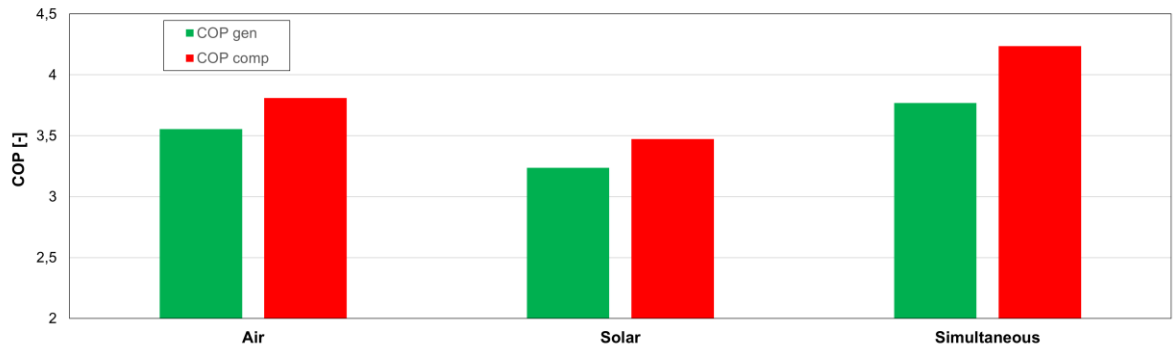

Figure 3.7 - COP comparison between the three configurations

This difference can be explained by the different amount of power that is consumed in the three configurations. While in solar-mode the power consumption comprehends only the compressor and pump, in simultaneous-mode also the fan is present. Figure 3.7 shows the importance of solar irradiance on the performance of the three configurations. Due to the quite high solar irradiance, the power output of the PV/T system in solar and simultaneous-mode is high enough to cover the power consumption of the system, especially in solar-mode since solar irradiance is 10 % higher than in simultaneous-mode for the considered test.

Table 3.4 - Results comparison between the air, solar and simultaneous-mode in similar external conditions

Mode	T_{air} [°C]	GTI [W/m²]	T_{ev} [°C]	COP_{gen} [-]	COP_{comp} [-]	rp [-]	P_{PV} [-]	P_{gen} [-]
Air	8.79	851	2.33	3.55	3.81	2.26	/	538
Solar	8.88	890	1.19	3.24	3.47	2.38	723	668
Simult.	8.65	813	5.35	3.77	4.24	2.00	650	676

In previous works, it has been demonstrated that the heat pump may perform better in solar-mode than in air-mode when the air temperature is low and solar irradiance is high, but for low solar irradiance values its performance decreases dramatically. For this reason, the simultaneous configuration represents the only viable way to employ a PV/T evaporator in a Mediterranean region in which the solar irradiance during winter is extremely variable and stays around relatively low values.

On the other hand, the convenience of the simultaneous configuration over single-source options is evident also at low solar irradiance conditions, as shown by Figure 3.8, that presents

COP results from a test carried out in low solar irradiance conditions, about 180 W/m^2 with 9 °C of air temperature.

Figure 3.8 – Test performed with GTI = 180 W/m2, T_{air} = 9 °C, $T_{w,in}$ = 30,5 °C

Clearly the performance increase in this case is more limited, due to the extremely low solar radiation intensity, however by coupling the PV/T evaporator the system is still able to gain 6,7 % relatively to the COP_{comp}. Due to the higher power consumption for the presence of the pump, the COP_{gen} increase is lower (5.2 %).

This series of tests has demonstrated the positive impact of integrating a PV/T evaporator into the studied dual-source heat pump system. Solar irradiance significantly influences the capacity of the PV/T evaporator. Higher GTI not only increases the produced electricity but also enhances the heat flux through the back of the panel, providing more energy for the evaporation of the refrigerant. This results in a higher evaporation temperature. As shown by Figure 3.1, even with very low solar irradiance the performance of the heat pump system is improved compared to the single-source air-mode system. Furthermore, if the solar irradiance is sufficiently high, the power generated by the PV system can be enough to meet the total power consumption of the heat pump.

Results indicate that the heat pump performs better at higher air temperatures. This is because higher air temperatures lead to higher evaporation temperatures, positively affecting the performance of both the finned coil and, to a lesser extent, the PV/T evaporators. Additionally, a higher evaporation temperature reduces the pressure ratio, lowering the specific work of the compressor and thus the denominator in the COP calculation. This improvement in volumetric

efficiency increases the mass flow rate processed by the compressor, thereby enhancing the heating capacity of the system.

Chapter 4

Numerical model

Data collected during the experimental campaign have been processed with the calculation model to simulate the system behaviour in steady-state and dynamic conditions. The model was updated to work with the system in simultaneous configuration during the previous master thesis, while the present work tries to extend the set of experimental data used for validating the model, both in steady-state and dynamic operation. The chapter begins with an examination of the mass ratio, a parameter indicating the regulation of mass flow rate of refrigerant passing through the internal heat exchanger (IHE). The objective is to optimize this parameter to optimize calculation errors for the steady-state tests conducted this year. In subsequent sections, the validation of the model will be done by comparing experimental measurements with results obtained by the calculation code. Additionally, the dynamic behaviour of the machine is modelled and compared across the three machine operative modes.

4.1 Model description

The heat pump system model built in MATLAB is designed to evaluate the system's performance under both steady state and dynamic conditions, based on several environmental and operational inputs, such as air temperature, solar irradiance, direct normal irradiance (DNI) incidence angle, wind velocity, water temperature at the gas cooler inlet, water flow rate at the gas cooler inlet and lamination temperature.

The performance evaluation first begins with the calculation of the evaporation temperature, that is done by solving a polynomial equation whose coefficients depend on the compressor speed. The model uses REFPROP to determine the thermodynamic properties of the air. These properties are crucial for calculating the conditions of the refrigerant at the evaporator outlet. The evaporation performance of the system's finned coil evaporator is influence by the air flow rate, which in turn depends on the fan speed. The fan speed is regulated by the frequency, as described by the relationship between the frequency and the rotational speed of the fan.

$$n = \frac{60f}{p} * (1 - s) \tag{4.1}$$

where the term $\frac{60f}{p} = n_0$ is the synchronism velocity of the electric engine, that in an asynchronous motor differs from the rotational velocity because of the motor slip. Sequential calculations of the air flow rate and evaporator efficiency allow the model to determine the system's evaporation capacity as well as the enthalpy and vapor quality at the evaporator outlet.

For the PV/T (photovoltaic/thermal) evaporator, the model uses a distributed parameter approach to return the spatial distribution of the refrigerant properties along the coil. The PV/T evaporator is divided into several control volumes and an energy balance is performed for each volume. The process gives the values of enthalpy and vapor quality as output, which are needed to evaluate the new iteration of evaporation temperature. The new evaporation temperature is used to determine the mass flow rate and other thermodynamic variables at different points in the cycle, which are essential for assessing the system's overall performance.

The gas cooler model analytically determines the refrigerant temperature at the outlet and the thermal capacity. Inputs required for this model include the refrigerant temperature at the inlet, water temperature at the inlet, refrigerant mass flow rate, water mass flow rate and compressor discharge pressure. The output values are found with an iterative process that compares the real gas cooler area with a guessed one, until convergence is reached.

Similarly, the regenerative heat exchanger model calculates the refrigerant temperature at the outlet on both the high-pressure and low-pressure sides. This model also employs an iterative process to compare the guessed heat exchanger area with the actual area until convergence is achieved. The conditions of the refrigerant at the compressor inlet depend on the fraction of mass flow rate that is pre-heated in the IHE with respect to the fraction which is directly sent to the compressor suction, bypassing the IHE. The impact of this parameter is relevant, therefore it is described more in detail in the next paragraph.

4.2 Calibration of the internal heat exchanger

The performance of the heat pump is significantly influenced by the behaviour of the IHX. At the low-pressure receiver outlet, a three-way valve regulates the fraction of refrigerant mass flow rate that passes through the IHX, while the remaining amount goes directly to the compressor suction. The IHX preheats the incoming refrigerant by cooling the refrigerant stream exiting the gas cooler, ensuring that only vapor enters the compressor suction. The

parameter *rapm* represents the ratio between the flow rate directed to the compressor suction and the flow rate sent into the regenerative heat exchanger.

In the previous study this parameter has been fixed at 0.8. However, this year's analysis has involved a more detailed investigation to determine the appropriate mass flow rate based on varying testing conditions. The previous year's experimental campaign primarily involved tests in simultaneous configuration under fixed conditions (HP = 80 bar, f_{comp} = 50 %, water inlet and outlet temperature fixed at 30 and 35 °C respectively). This year, a broader range of conditions necessitated a more thorough analysis.

A mathematical model was developed to evaluate the temperature estimation error of the regenerative heat exchanger model. The procedure consists in evaluating the refrigerant temperature at the heat exchanger outlet for both the low-pressure and high-pressure sides of the heat exchanger. This error is calculated for a selected set of tests and values of *rapm*. The calculation requires the following inputs:

- Refrigerant temperature at the gas cooler outlet
- Vapor quality at the inlet, so at the low-pressure receiver outlet
- Refrigerant mass flow rate
- Mass ratio
- Evaporating pressure
- Gas cooler pressure

A selected set of tests from the experimental campaign has been used, that sums up the different external conditions in which the machine has operated. Experimental results are compared with the model's predictions:

$$err_{HP}(i,j) = tref_{o,HP(real)}(i) - tref_{o,HP(model)}(i,j) \tag{4.2}$$

$$err_{LP}(i,j) = tref_{o,LP(real)}(i) - tref_{o,LP(model)}(i,j) \tag{4.3}$$

where:

- *i* is the index referring to a value in the input/output array
- *j* is the index referring to a mass ratio value within its array

The regenerative heat exchanger sub-model, like the condenser and gas cooler models, operates by discretizing the volume into small elements, each treated as an individual heat exchanger. Continuity and energy equations are solved for each element, neglecting the pressure drop. The model analytically evaluates the refrigerant temperature at the outlet of both the low-pressure ($T_{comp,in}$) and high-pressure ($T_{in,lam}$) sides. The model compares the real regenerative heat exchanger area with a hypothetical one (A_{hyp}). The value of *rapm* is an input parameter for the sub-model.

Input values from the experimental tests were used, with a fixed tolerance of 0.01, to calculate the error of the IHX model. By comparing the results obtained with different values of *rapm*, the optimal value that minimizes calculation error was identified. Results show that the average error with the new values is extremely low, apart from a couple of outliers.

The Table 4.1 presents the optimum value of *rapm* that minimizes the calculation error. It also details the selected tests, representing different external conditions.

Table 4.1 - Optimum value of rapm for selected tests from the fifth experimental campaign, fan 50 %

Test details							Results		
Test ID	Mass flow rate [kg/s]	High pressure [bar]	T in,LP [K]	Tout,LP [K]	Tin,HP [K]	Tout,HP [K]	rapm [-]	Err_LP [K]	Err_HP [K]
5C1	0,0117	80	2,62	12,32	29,57	21,94	0,66	0,053	0,051
5C2	0,0118	80	2,57	11,74	29,29	21,15	0,68	0,006	0,030
5C4	0,0224	85	1,20	13,40	33,21	26,41	0,68	0,028	0,018
5C5	0,0229	85	0,44	10,21	29,74	21,61	0,68	0,094	0,058
5C9	0,0225	85	1,99	17,43	32,65	24,27	0,85	0,026	0,025
5C10	0,0211	85	3,03	23,05	36,31	31,44	0,86	0,096	0,012
5C13	0,0217	85	4,09	23,79	36,50	31,84	0,88	0,102	0,083
5C15	0,0237	85	2,48	15,16	30,16	20,90	0,86	0,062	0,054
5C18	0,0240	85	3,59	17,97	32,85	24,58	0,87	0,075	0,045
5C21	0,0124	90	9,31	26,61	39,45	34,43	0,84	0,086	0,028
5C22	0,0230	90	5,13	24,81	38,85	33,36	0,89	0,054	0,070
5C23	0,0134	80	5,68	13,54	25,23	15,72	0,89	0,007	0,029
5C24	0,0136	80	7,15	16,04	27,58	18,18	0,89	0,018	0,072
5C25	0,0140	80	6,62	13,83	24,73	15,77	0,89	0,048	0,017
5C26	0,0239	80	4,57	20,98	31,68	23,01	0,95	0,675	0,471
5C28	0,0221	80	5,69	27,86	33,99	29,80	0,98	2,481	0,007
5C29	0,0116	80	2,49	13,54	29,07	19,89	0,77	0,011	0,022

The optimum value is different for each of the tests, however it is clear that while for the first tests the optimum value was found around 0.7, starting from the test n° 9 the *rapm* optimum values are generally found between 0.8 and 1.

4.3 Steady-state model

4.3.1 Simultaneous-mode

In this section the validation of the steady-state model will be described. This procedure consists in defining the accuracy of the results obtained by the calculation model. Each experimental test will be simulated by the model starting from a set of input variables, and when the model reaches convergence, some selected parameters are compared with the measured data, evaluating the calculation error. The chosen parameters for the accuracy evaluation are COP_{gen} and T_{evap}.

Calculation error is expressed as the difference between experimental value and results calculated by the model. Figure 4.1 shows the calculation error of the T_{evap} throughout all the tests performed in simultaneous configuration. The model predicts the value of the evaporation temperature with variable accuracy throughout the different tests performed in simultaneous evaporation mode. However, the average error is equal to 0.75 °C, which can be considered accurate enough.

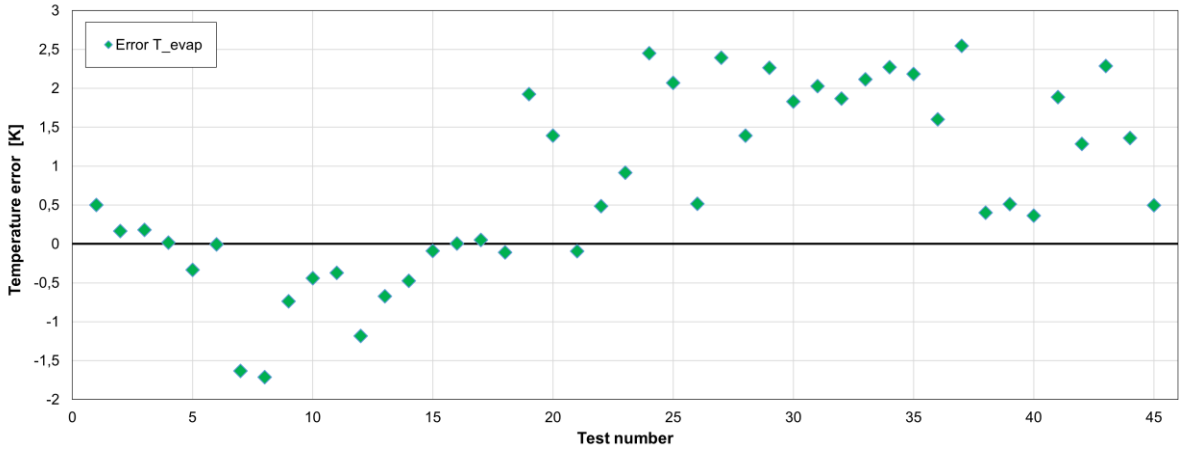

Figure 4.1 – Evaporation temperature error of the tests performed this year in simultaneous-mode. Data comprehend test compressor at 50 – 100 % nominal speed, high pressure 80, 85, 90 bar, fan at 50, 75, 100 % nominal speed, GTI between 165 – 1100 W/m2, Tair between 6 – 17 °C,

Average COP_{gen} error is 2.51 %, and nearly all the tests are inside the 5 % error range. The maximum error registered is equal to 6.68 %, happened for a test in which inlet temperature is 25 °C and compressor velocity is at its maximum.

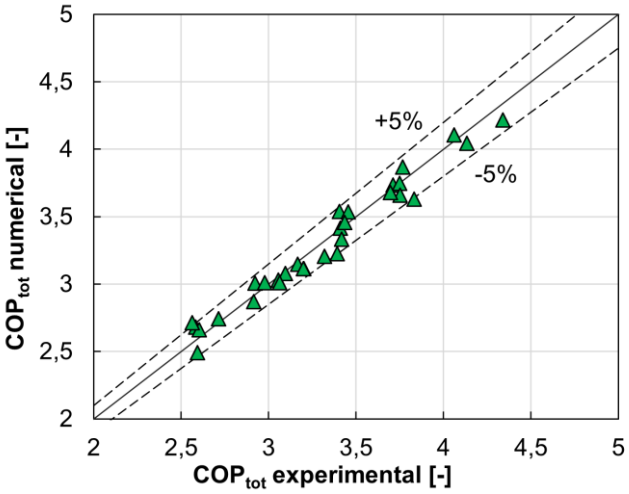

Figure 4.2 - Steady-state validation, COP error – simultaneous-mode

The numerical model is able to predict properly the performance parameters of the heat pump, with only three tests showing an error slightly higher than 5 %.

4.3.2 Air-mode

The steady-state validation has been performed also for the air-mode operation. A set of 10 experimental tests has been chosen to perform the validation.

The chosen parameters for validation are COP_{gen} and T_{evap}. The evaporation temperature is well predicted as shown in Figure 4.4, with an average calculation error of 0.29 K.

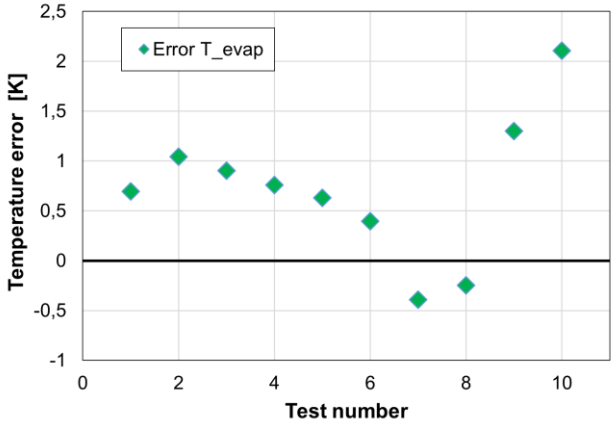

Figure 4.4 – Evaporation temperature error, air-mode

Figure 4.5 shows the COP calculation error. Results are well predicted, with an average error of 3.78 %.

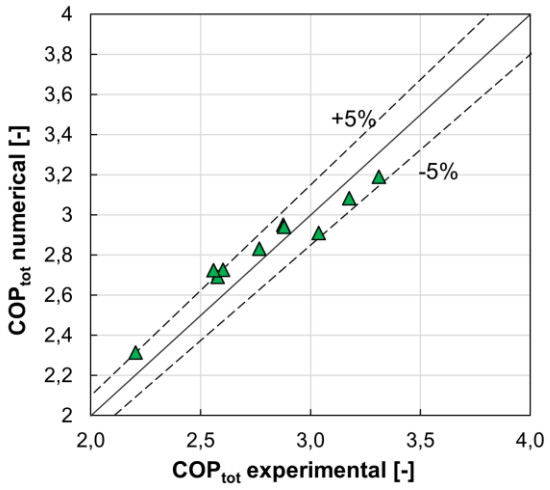

Figure 4.5 - Steady-state validation, COP error – air-mode

4.4 Dynamic model

The study of the heat pump's behaviour under dynamic conditions is this year supported by some dynamic tests conducted between December 2023 and February 2024. Data have been used to validate the numerical model.

The model in steady state conditions can be easily adapted to work in dynamic mode. In dynamic tests the goal is to see how the heat pump will adapt to the changes in the environmental conditions, by entering the dynamic regime aiming to reach a new steady-state condition. The data acquisition process works the same as in steady-state tests, so with one measurement collected every 10 s. However, in dynamic tests each measurement represents a point of dynamic behaviour.

The measurement begins from a steady-state point, from which one point is collected every 10 s, for a two-hour interval. The input variables of the model, coming from the experimental data, are:

- Air temperature
- Solar irradiance on the tilt plane
- DNI incidence angle
- Wind velocity
- Water temperature at the gas cooler inlet
- Water flow rate at the gas cooler inlet
- Lamination temperature

The matrix enters the code after the same input variables are given as steady-state initial point after which introducing the perturbation, in terms of solar irradiance and air temperature.

4.4.1 Model validation in simultaneous-mode

In the dynamic test collected on 21/12/2023, the initial steady state conditions are:

- Compressor velocity: 50 %
- High pressure: 80 bar
- Air temperature: 8.2 °C
- GTI: 594 $\frac{W}{m^2}$
- Water inlet temperature: 30 °C
- Water flow rate: 425.9 $\frac{kg}{h}$

The test has been performed with the heat pump working in simultaneous-mode. Environmental conditions throughout the test are shown in Figure 4.6.

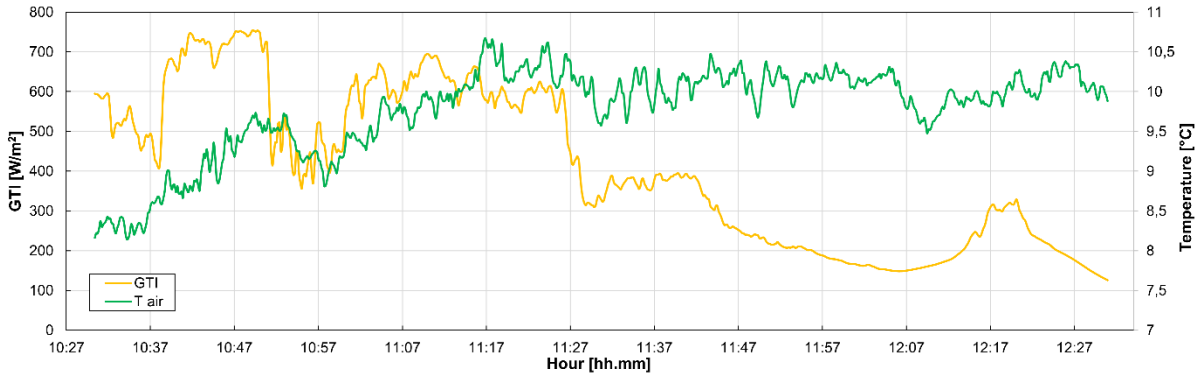

Figure 4.6 – Air temperature and solar irradiance variation during the dynamic test carried out on 21/12/2023.

Figure 4.6 shows how both solar irradiance and T_{air} change over time. The cloudy sky made the GTI vary significantly during the first half of the test, with many peaks and lows between 400 and 800 W/m^2. At the beginning of the second hour of testing, following an abrupt decrease, the GTI remains under 400 W/m^2 for the remaining testing period, while still undergoing significant variations. Accordingly, the air temperature increases when the GTI is higher, following well the trend of the radiation during the first hour, to remain instead around a constant value of 10 °C in the second hour, when the GTI is lower.

The model validation is done by comparing the experimental data and the data produced by the model. The comparison is done on some selected parameters with the goal of analysing the

mere performances (T_{ev}) but also the useful effect (gas cooler capacity). Figure 4.7 reports the comparison between the measureddata and the predicted values of the evaporation temperature obtained on the partly cloudy day shown in Figure 4.4.

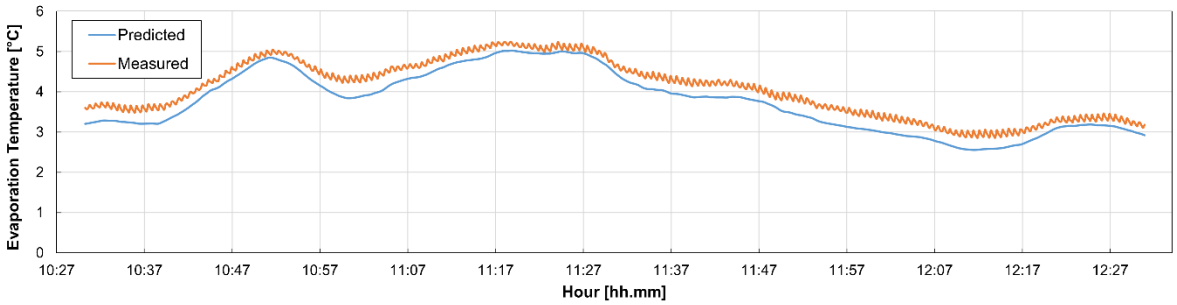

Figure 4.7 – Measured and predicted evolution of the evaporation temperature during a partly cloudy day

The model follows very well the measured data. Even in the presence of strong variations of the environmental conditions, as happening in the first half of the test, the model can quickly adapt and predict correctly the T_{ev} trend. Being this a test realized in simultaneous-mode, the evaporation temperature will depend both on the solar irradiance heating up the fluid in the solar panels and on the air temperature, the trend of which is also in some way correlated to the solar irradiance. As a matter of fact, we can observe how the evaporation temperature increases when the solar irradiance is higher, replicating here the trend of the air temperature. In the second half of the test instead, when the solar irradiance decreases, while the air temperature remain mostly at a constant value, the evaporation temperature goes through an evident decrease, due to the impact of the reduced performance of the PV/T evaporator. There is a slight but rather constant underestimation by the model, that becomes more evident in the decreasing section. However, even in the worst case, the difference remains very limited, with a peak error of 0.55 °C and an average of 0.29 °C.

Figure 4.8 reports the comparison between the measured data and the predicted values of the gas cooler heating capacity obtained on the partly cloudy day shown in Figure 4.6.

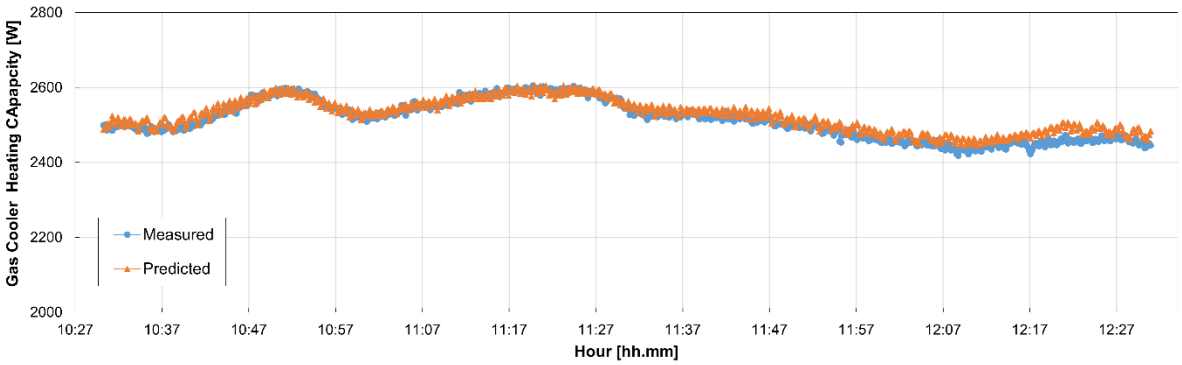

Figure 4.8 – Measured and predicted evolution of the gas cooler heating capacity during a partly cloudy day

Gas cooler performance prediction is even better. The chart shows that the predicted trend nearly coincides with the measured data. A slight variation can be seen towards the end of the measurement, but also in this case the peak error is very limited (2 %) and the average stays at 0.64 %, well below the technical 5 % limit. Data presented and analysed in the current paragraph clearly confirms that the model can properly predict the heat pump performance.

4.4.2 Comparison between different evaporator modes

Starting from the environmental conditions of the dynamic test in simultaneous-mode (Figure 4.6), the calculation models for the dynamic test in air-mode and solar-mode has been used to simulation the heat pump performance. In the present paragraph, the performance of the heat pump in the three different working configurations is investigated and compared. Figure 4.9 shows the evaporation temperature evolution during a partly cloudy day for the three heat pump operation modes.

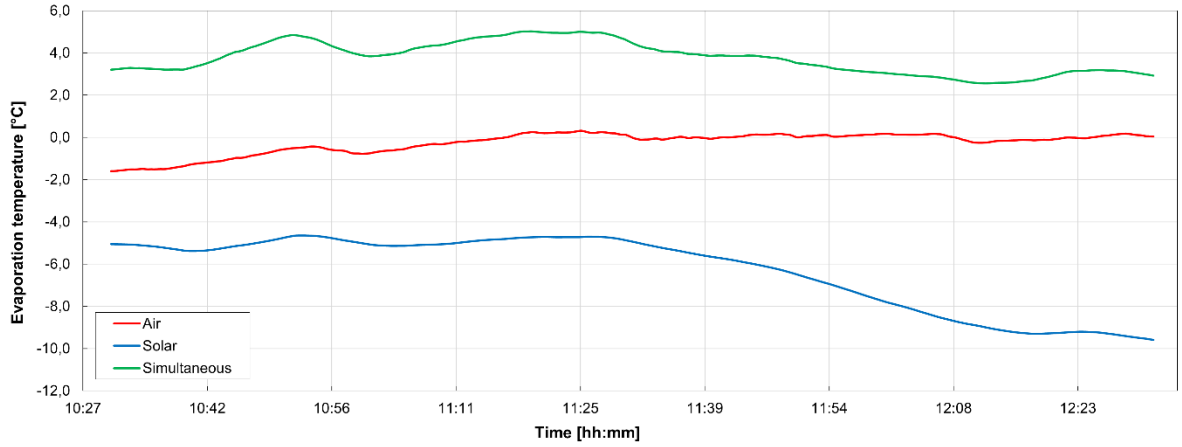

Figure 4.9 - Comparison between the numerical evaporation temperature for the air, solar and simultaneous-mode during a partly cloudy day.

The solar heat pump is the configuration with the worst evaporation performance. In this case, the heat pump performance depends totally on the solar irradiance. However, adding the PV/T evaporator to the air-source heat pump seems to increase its performance. While the air-source heat pump is clearly not influenced by the fluctuation of the solar irradiance, the simultaneous heat pump suffers a bit, however the decrease is very limited, and in all the points the evaporation temperature reached in simultaneous-mode is higher than the one reached in air-only evaporation. The gas cooler power behaves in the same way, as reported by Figure 4.10.

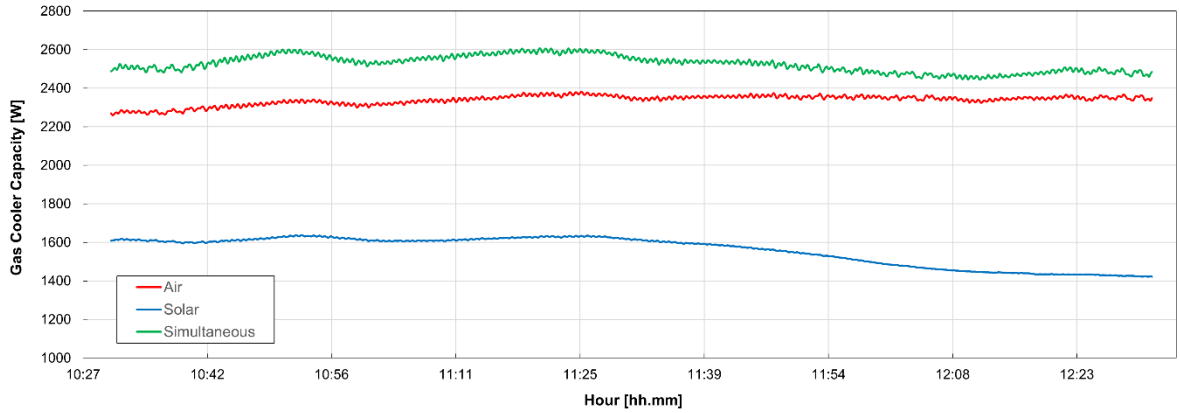

Figure 4.10 – Comparison between the numerical gas cooler heating capacity in the air, solar and simultaneous-mode during a partly cloudy day.

The performance of the gas cooler is determined by the performance of the evaporator. It is important to remember that these dynamic tests have been carried considering that the water flow rate was continuously changed in order to keep both a constant outlet temperature and temperature difference, so that water goes back to the storage tank always at the same temperature. The gas cooler capacity shown by the simultaneous-mode can therefore heat up, for the same environmental conditions, a higher amount of water compared to the other two modes.

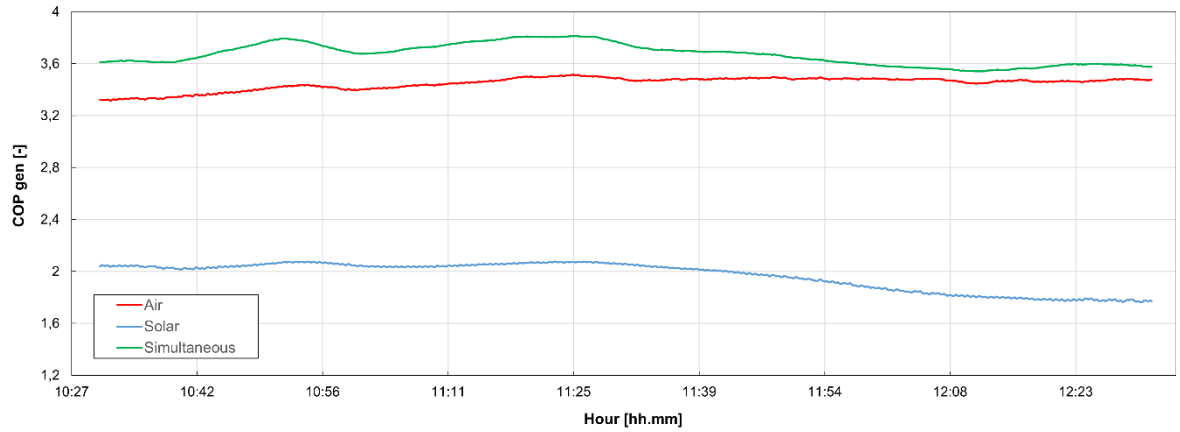

Figure 4.11 - Comparison between the numerical COP values for the air, solar and simultaneous-mode during a partly cloudy day.

Figure 4.11 shows how, while solar COP is much lower, the COP of air and simultaneous-mode are very close. The difference between the simultaneous and air-source heat pumps being higher at medium/high solar irradiance and attenuating for low solar irradiance.

In the experimental apparatus used in this thesis, the PV/T evaporator is not optimized for the operation, therefore considering a properly sized system, PV/T performance would increase, making the simultaneous configuration even more convenient.

4.4.3 Model validation in air-mode

A dynamic test conducted in air-mode during a previous campaign has been used for the model validation in air-mode. In this test the compressor velocity has been manually increased throughout the test from 50 to 90 % of the nominal velocity. The portion of the test considered in this paragraph has been carried out on 26/01/2022, from 12:20 to 14:49.

The initial steady state conditions are:

- Compressor velocity: 50 %
- High pressure: 80 bar
- Fan velocity: 100 %
- Air temperature: 5.3 °C
- Water inlet T: 18 °C
- Water flow rate: 79.3 $\frac{kg}{h}$

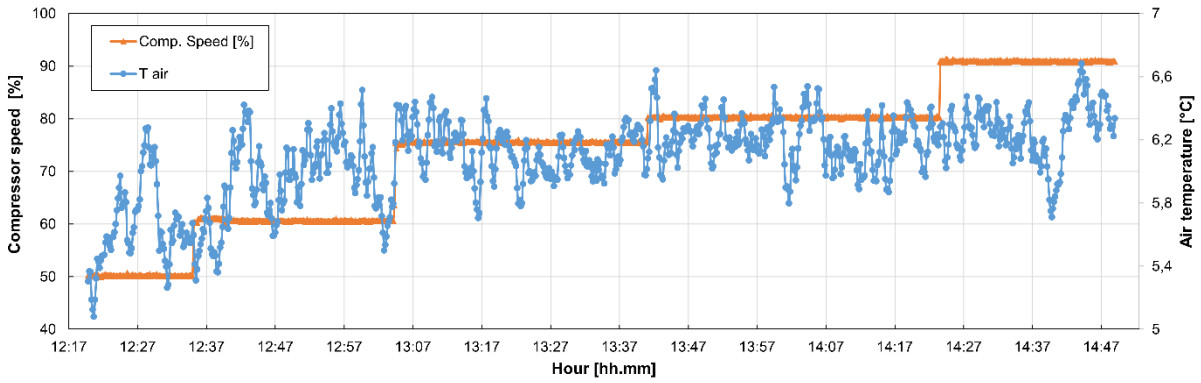

Figure 4.12 – Air test input

Figure 4.13 shows that the model predicts very well the evaporation temperature before the second frequency step increase, achieving an average error of 0.07 K in this first time fraction. In correspondence of the second frequency step increase the model starts to underestimate the evaporation temperature, increasing the average error to 0.94 for the remaining section of the testing period.

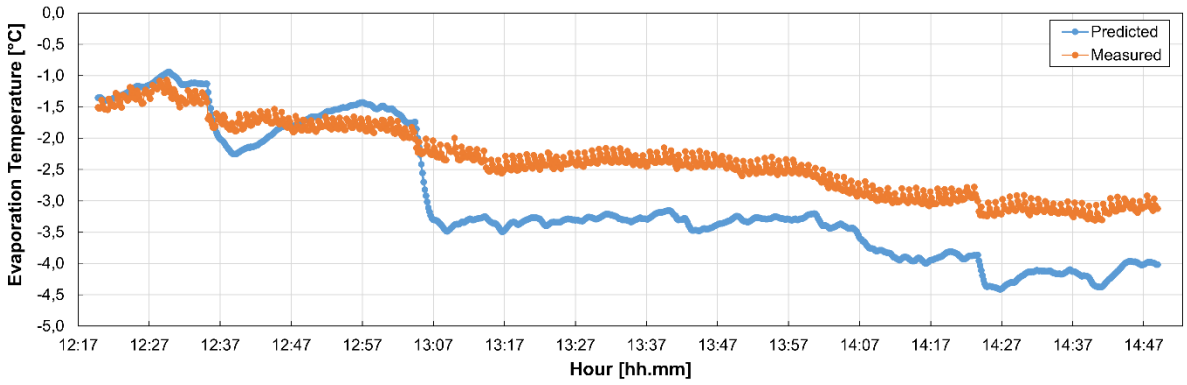

Figure 4.13 – Evaporation temperature prediction in a dynamic test with variable compressor rotational velocity

Figure 4.14 illustrates the predicted gas cooler capacity, that aligns with the measured data except near the points when the compressor frequency is adjusted. These discrepancies can be attributed to fluctuations in the mass of refrigerant, which is directly influenced by changes in compressor frequency.

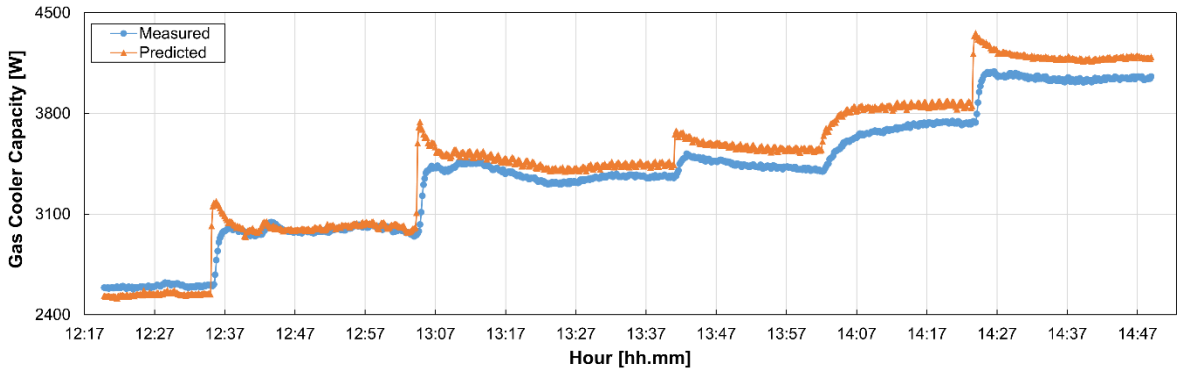

Figure 4.14 – Gas cooler capacity prediction in a dynamic test with variable compressor rotational velocity

This results in a peak error in correspondence of this area, and in an overestimation in the remaining part of the test. Despite this, the average calculation error maintains at 2.70 %, well below the 5 % average limit. As demonstrated in Figure 4.6, an increase in compressor frequency enhances the gas cooler capacity. This is because a higher frequency results in the compressor rotating more rapidly, thereby handling a greater mass flow rate of refrigerant. The gas cooler capacity overestimation reflects in an overestimation of the COP, since power consumption is predicted very well with average error of 0.76 % and maximum of 4 %. As depicted in Figure 4.15, the COP_{gen} trend is well predicted, with an average error of 2.42 %.

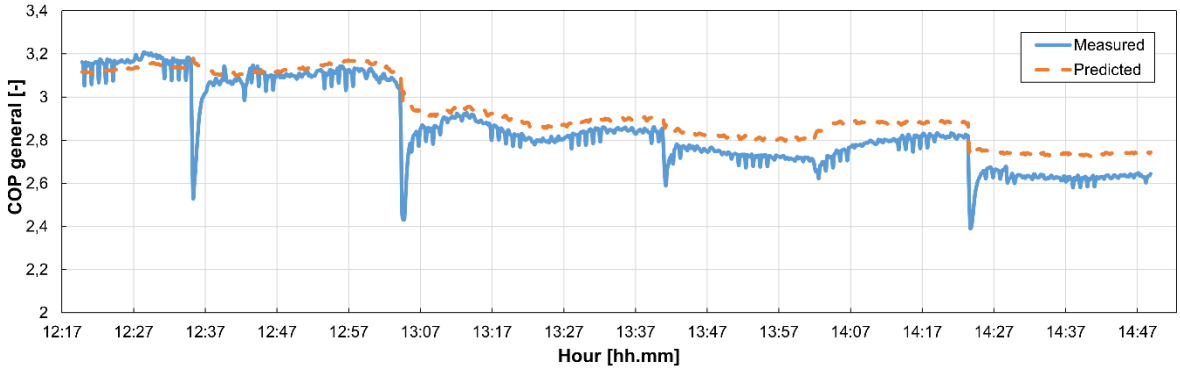

Figure 4.15 – General COP prediction in a dynamic test with variable compressor rotational velocity

As the compressor speed increases, a notable difference in the response dynamics between the numerical model and the experimental unit is observed. This discrepancy, initially evident as model inertia, stabilizes after a transition period, allowing for accurate predictions thereafter. Despite the enhanced gas cooler capacity, the system's COP decreases. This decline is primarily due to the disproportionately higher increase in compressor power consumption (P_{comp}), compared to the increase in heat output from the gas cooler (Q_{gc}). This relationship is clearly depicted in Table 4.2, which shows the average values of P_{comp} and Q_{gc} at various compressor

frequencies. The percentage increase relative to previous values is also detailed, highlighting the increasing energy demand at higher frequencies and its impact on overall system efficiency.

Table 4.2 – Effect of the compressor frequency variation on system performance

Time	f_{comp} [%]	P_{comp} [W]	% increase	Q_{gc} [W]	% increase	COP_{gen} [-]
12:20	50	639		2541		3.16
12:36	60	790	23	3018	19	3.08
13:05	75	1008	28	3469	15	2.83
13:42	80	1110	10	3704	7	2.76
14:24	90	1341	21	4202	13	2.63

4.4.4 Variable inlet water temperature

In the dynamic test performed on 21/02/24 in simultaneous-mode, the inlet temperature of the water at the gas cooler has been varied manually throughout the test. The test begins in the following conditions:

- Compressor velocity: 100 %
- High pressure: 85 bar
- Air temperature: 17.04 °C
- GTI: 692 W/m^2
- Water inlet T: 17.28 °C
- Water outlet T: 60 °C
- Water flow rate: 116.4 kg/h

Figure 4.16 shows the solar irradiance and T_{air} trend throughout the test, performed with the heat pump in simultaneous-mode.

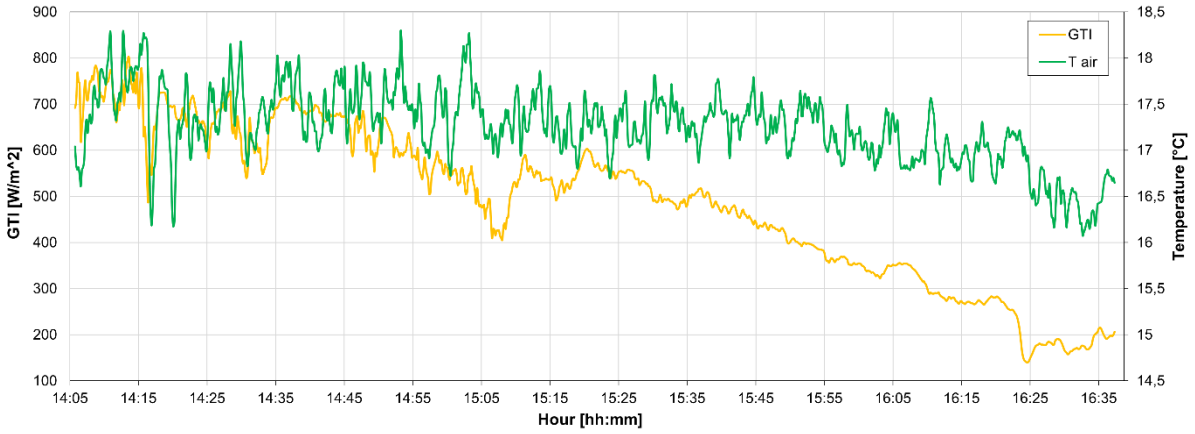

Figure 4.16 - Climatic conditions for the dynamic test carried out on 21/02/2024 in simultaneous-mode

Figure 4.16 shows that ambient temperature is not influenced by the GTI, that keeps decreasing. Fluctuations in ambient temperature are continuous, so no correlation between irradiation and air temperature can be found.

At the beginning of the test, the heating resistances in the cold tank are switched on, and water starts to heat up. The first hour of test shows some inertia and after a transition period water temperature starts to increase linearly, at a rate of approximately 0.29 K per minute. As the temperature of the water in the tank increases, $T_{w\ in,gc}$ increases as well, and this reflects in a modification of the heat transfer between the refrigerant and the water in the gas cooler, which affects the COP of the machine. To investigate this effect, the water temperature at the outlet of the gas cooler has been kept fixed at 60 °C throughout the test by continuously acting on the opening level of the water circuit valve. Figure 4.17 shows the effect of water temperature increase on the COP_{comp}.

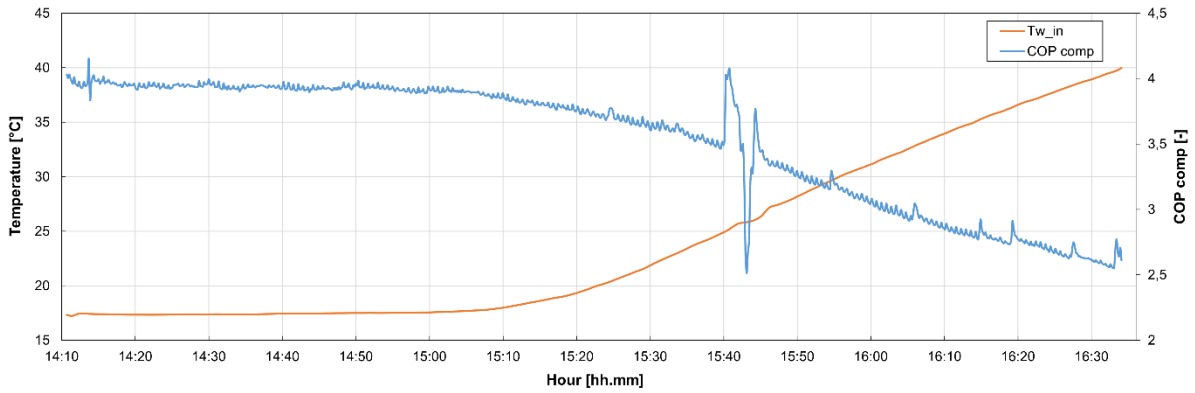

Figure 4.17 - Effect of the variable inlet water temperature on the COP

The increase of $T_{w\ in,gc}$ has a relevant impact on the COP. When the temperature starts to increase, the COP variation follows a linear trend, indicating that on average the COP decrease is 0.174 per °C of temperature increase, meaning, with respect to the initial COP at the water temperature of 17 °C, a percentual decrease of 1.68 % per °C.

The impact of varying inlet water temperature on the theoretical vapor compression cycle is shown in Figure 4.18. Points of the cycle appearing in the diagram are:

1: Compressor suction

2: Gas cooler inlet

3: Lamination valve inlet

4: Evaporator inlet

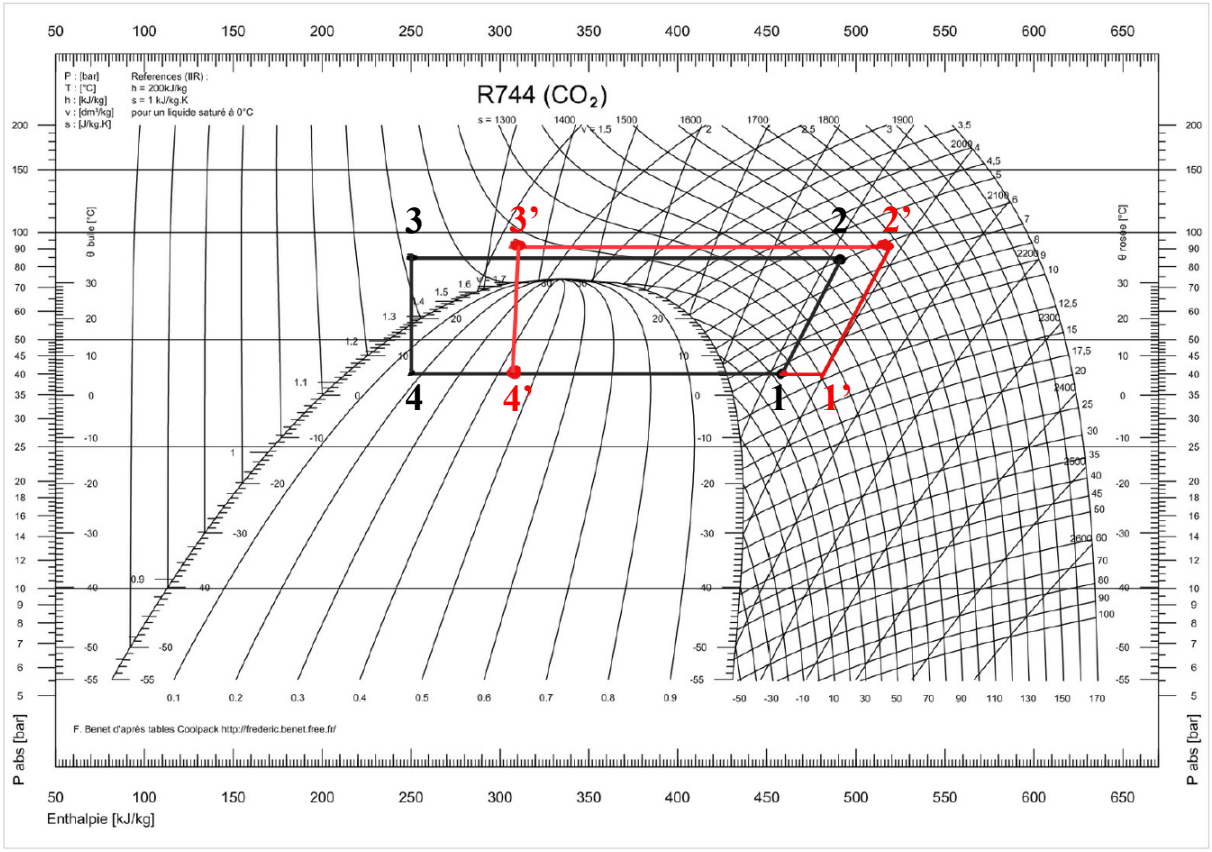

Figure 4.18 - CO2 p-h diagram showing the cycle evolution between initial and final test conditions.

The black cycle corresponds to the refrigerant conditions at the beginning of the test, when the water inlet temperature is 17 °C, while the red cycle refers to the refrigerant conditions at the end of the test, when water inlet temperature has increased to 40 °C. The refrigerant conditions

vary significantly through the test. Point 4' is moved in a region inside the curve with higher vapor quality. The compressor suction point 1' indicates a refrigerant much more superheated, where the refrigerant has a lower density. This reflects in a less efficient heat exchange process at the gas cooler: that is indicated by the lower enthalpy difference between the refrigerant gas at inlet and outlet of the device. The pressure ratio is higher, therefore the compressor's volumetric efficiency decreases, impacting on the COP. In summary, the heat extraction from the refrigerant becomes less efficient as the inlet water temperature is increased. The modification of the cycle highlighted by Figure 4.18 indicates that a much larger portion of the cycle area is outside the curve, potentially turning into a less efficient heat exchange process.

Similarly, also for this test the numerical model has been used to compare results in series mode with results in air and solar only mode. As expected, the simultaneous-mode proved to be better than both the other working conditions. Air and simultaneous-modes show comparable performance in terms of evaporation temperature, evaporating capacity and most of all COP and gas cooler capacity. The solar-mode is highly penalized by low irradiance, that eventually decreases as time goes on. Air and simultaneous-mode are instead not affected by this parameter, and they perform both well thanks to the high environmental temperature, that allows to maintain high evaporation temperature values.

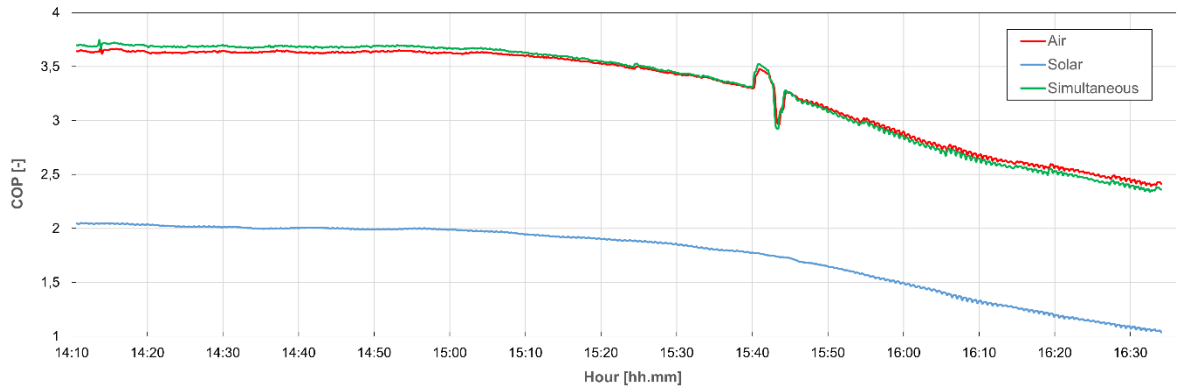

Figure 4.19 - COP comparison in the three working configurations

The case of the solar-mode requires some more reasoning. In this configuration, the solar irradiance is the only source of low temperature heat for the evaporation of the refrigerant. Therefore, the evaporation temperature decreases when the solar irradiance decreases. However, by comparing the two dynamic tests presented in this chapter, it can be easily seen that in this second case the solar-mode seems more penalized, even if the solar irradiance doesn't differ a lot from the first test. The evaporation temperature gets to much lower values

compared to the other two configurations, and other performance indicators such as the COP, Q_{gc} and Q_{evap} are affected as well. This is likely related with the higher compressor frequency, that in this dynamic test is 100 %. When the compressor works at a higher frequency, the mass flow rate of refrigerant elaborated increases. This increase improves the heating capacity at the gas cooler, but it also means that a higher mass flow rate of gaseous refrigerant is extracted from the receiver. To sustain the higher request, also the evaporating capacity should increase. However, being the number of solar collectors fixed, the PV/T evaporator may not be able to achieve this capacity increase. This can be made clearer by looking at some plots. Figure 4.20 shows the mass flow rate of refrigerant together with evaporation pressure when the heat pump works in solar-mode.

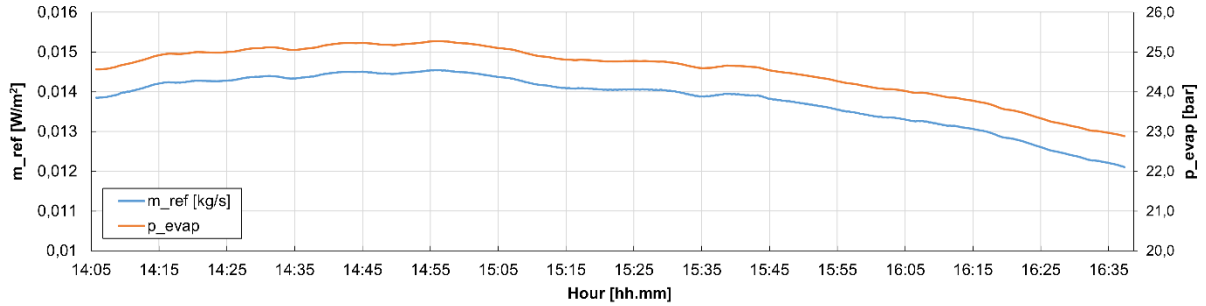

Figure 4.20 - Refrigerant mass flow rate and evaporation pressure evolution in solar-mode

The two parameters follow the same trend, that follows the decrease of the solar irradiance. The decrease of the mass flow rate comes from a decrease of the density of the refrigerant at the compressor inlet, which affects the performance of the compressor, by decreasing its volumetric efficiency and thus increasing its specific work, that ends up in a lower COP. By comparing the refrigerant's density trend in the three configurations, it appears clearly that the much lower density of the CO_2 in the flooded evaporator is responsible for the poorer performance of this system.

In the air and simultaneous configurations, the refrigerant's density trend depends much more on the air temperature. It can be also seen how the simultaneous and air source models are both affected by a sudden variation of density around 14:10 and 15:40, while the flooded evaporator system is not affected by this event. The explanation can be found in the fact that in the flooded configuration the refrigerant goes back directly to the receiver, from which only pure liquid is extracted to be evaporated. Therefore, the density of the refrigerant reaching the compressor only depends on this aspect. In the other two cases instead, before reaching the receiver, the refrigerant exiting the gas cooler passes through the air-source evaporator. Therefore, the

performance of the air-source evaporator is modified by a modification of the heat transfer in the gas cooler, reflecting in a modified density of the refrigerant visible at the compressor inlet (Figure 4.21).

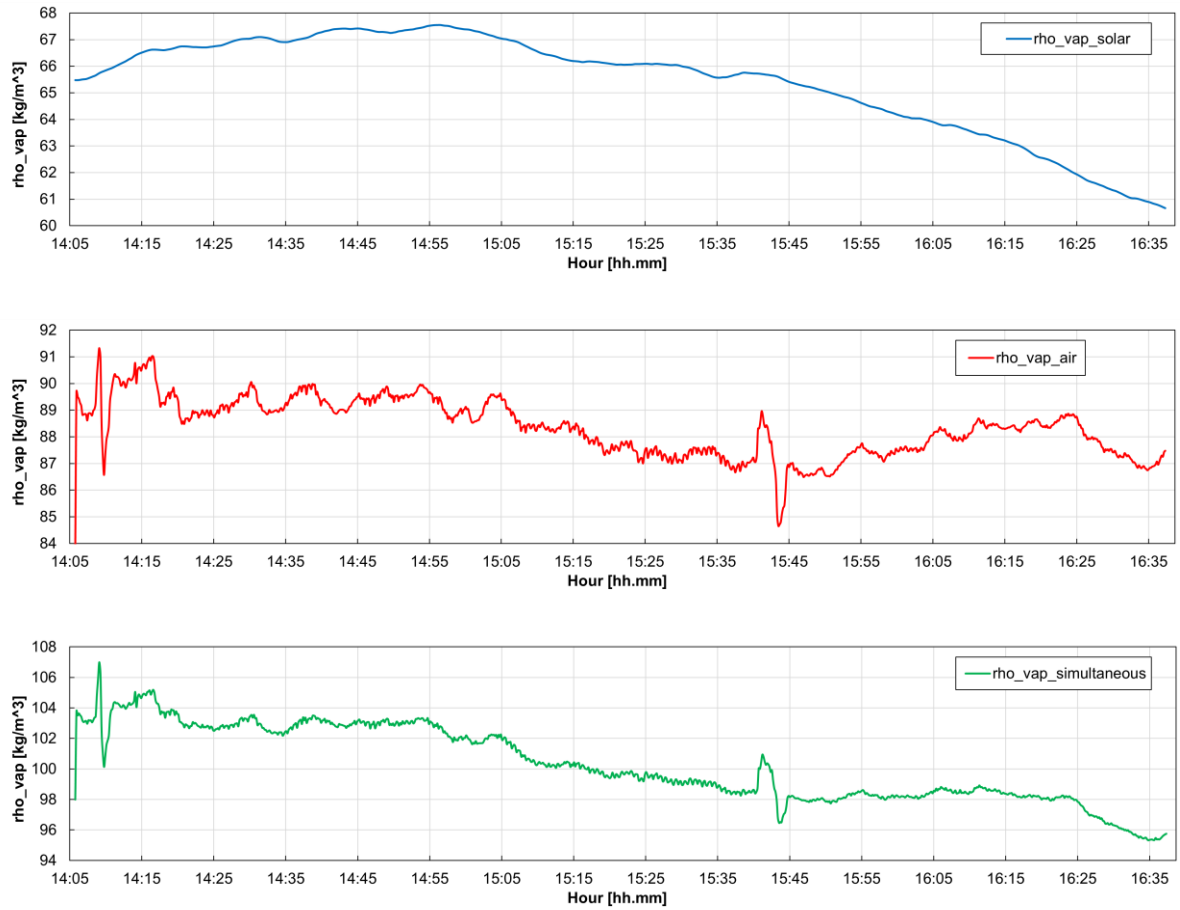

Figure 4.21 – Evolution of refrigerant's density throughout the dynamic test with variable inlet temperature in the three heat pump configurations

This test clearly shows that the number of PV/T collectors represents a limit in the stability of the heat pump performance. When the compressor frequency is higher, the simultaneous configuration performs much better.

Chapter 5

Seasonal performance of heat pumps for the building sector working with natural refrigerants

This chapter delves into the seasonal performance of heat pumps, extending the analysis beyond the steady state and short-term dynamic analysis covered in previous chapters. In the previous chapters these conditions have been extensively studied, highlighting their importance in design and use of heat pumps. When comparing the performance of different heating systems, it is crucial to assess their long-term performance over an entire heating season. Multiple studies have explored this theme, applying their findings to residential and commercial heat pump systems. A key metric in this analysis is the Seasonal Coefficient of Performance (SCOP), which quantifies the useful energy output relative to energy input over a heating season.

This chapter presents various simulations based on climatic data from Rome and Strasbourg, focusing on three heat pump systems that produce hot water for both domestic heating (DH) and domestic hot water (DHW). A user profile built based on normative standards [32], realistically represents typical operating conditions in a temperate (Rome) and continental (Strasbourg) climate.

A numerical model which evaluates the seasonal performance of different CO_2 heat pump configurations is introduced. Numerical results for the heating season compare a dual-source solar-air CO_2 system with CO_2 and propane air-source heat pumps.

5.1 Seasonal COP definition

Compared to conventional alternatives such as gas boilers, heat pumps require a higher capital investment. Therefore, for heat pumps to be economically viable, they need to have lower operating costs over a long period. A primary economic indicator of this viability is the Seasonal Coefficient of Performance (SCOP). SCOP represents the amount of useful energy produced during the heating season – essentially the desired outcome of the heating system – relative to the power consumption required to achieve it.

$$SCOP = \frac{\sum Q_1}{\sum E} = \frac{total\ useful\ heat\ energy}{total\ operating\ energy} \quad (5.1)$$

When comparing multiple heating alternatives, the system that requires the least amount of power to deliver the same amount of heat is the most cost-effective in terms of operating costs. The SCOP is of prime interest for the user, since it shows the net result for the full year operation and is thus a good indicator for the economic evaluation of the system. To achieve a high SCOP, a heat pump system must meet several conditions:

- High COP: The heat source should have a high and stable temperature level throughout the whole heating season. The heat sink temperature should be low, in order to extract as much heat as possible from the hot refrigerant.
- Low heat losses from the warm side
- Minimum idling losses of the system
- Low energy consumption of accessories: Measurement system and pumps should work at high efficiency points
- Minimizing defrosting losses

When heating buildings, the heat pump normally doesn't cover all the yearly heating demand, as it is usually beneficial to have a supplementary heat source to help heat the building during the coldest days of the year. Unless specified, the supplementary heating demand is not included in the SCOP. Generally, the heat demand varies strongly with the outdoor temperature, with the maximum demand occurring only for a very short time each year. Given the relatively high installation cost of heat pumps, it is in most cases not advisable to dimension the heat pump for the full system load on the coldest day. It is instead more practical to install a supplementary heat source to cover up the maximum load conditions. In addition, due to the widely variable heating load given especially by the DHW needs, it is essential to couple the hydronic circuit with a hot water storage tank, to limit the number of on-off cycles of the heat pump system.

5.2 System layout

A numerical model to simulate the performance of a heat pump (HP) and its hydronic circuits has been developed for this study. Three different heat pumps have been considered for the comparison:

1. Air-source heat pump working with R290 as refrigerant (R290-AHP).

2. Air-source heat pump with R744 as refrigerant (R744-AHP).
3. Dual-source solar-air heat pump with R744 as refrigerant (R744-SAHP).

Figure 5.1 shows the layout of the heat pumps coupled with the water circuit for domestic heating (DH) and domestic hot water (DHW) production.

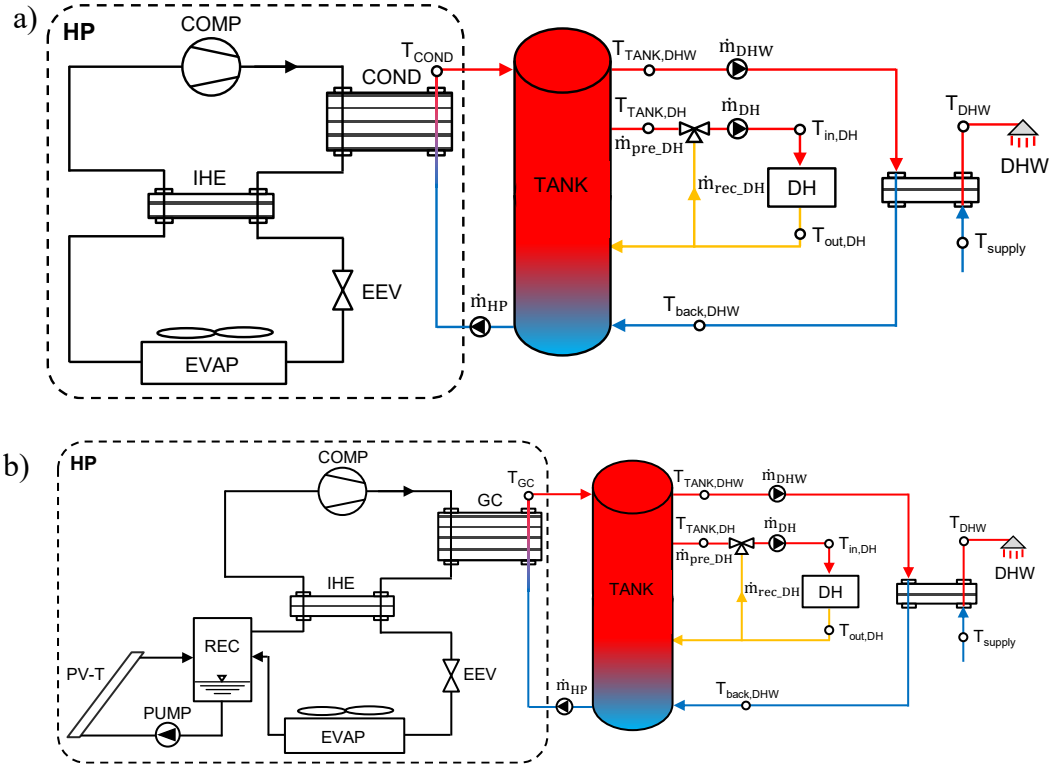

Figure 5.1 – Schematic representation of the heat pump systems: a) R290-AHP, b) R744-AHP and R744-SAHP

The R290-AHP (Figure 5.1a) system consists of a single-stage single-speed ON/OFF reciprocating compressor (COMP) paired with two brazed plate heat exchangers. One serves as a condenser (COND) while the other one acts as an internal heat exchanger (IHE). The circuit is completed by an electronic expansion valve (EEV) and a finned coil heat exchanger as an air evaporator (EVAP). The R744-AHP and R744-SAHP are shown together in a single scheme (Figure 5.1b).

The goal is to analyse the impact of two different refrigerants on the thermodynamic seasonal performance of these systems, therefore a comparable configuration for both R744 systems is required. The critical temperature of carbon dioxide is only 31 °C, lower than the temperature required for DH and DHW production, therefore the CO_2 operates a transcritical cycle. In the R744 heat pump a gas cooler (GC) substitutes the condenser, and a low-pressure receiver (REC)

is placed between the EVAP and the IHE to stabilize the system's low pressure and ensure a continuous supply of saturated vapor at the evaporator outlet, as confirmed by previous studies [33]. In the R744-AHP the valve which connects the PV/T evaporator to the low-pressure receiver tank is closed.

The R744-SAHP corresponds to the system studied in previous chapters. Compared to the R744-AHP and R290-AHP, it includes PV/T collectors, supplied with liquid R744 drawn from the bottom of the REC by a circulating pump (PUMP). The IHE in all three models ensures adequate superheating at the compressor's suction point. The EEV has different roles in each system: in the R290-AHP it manages subcooling after the condenser and maintains saturated vapor at the evaporator exit, while in the R744 setups it functions as a back pressure valve, setting the high-pressure level.

Concerning the water circuit layout shown in Figure 5.1, all three heat pump systems are designed to supply DH and DHW. The generated hot water is utilized to cater to varying temperature demands. Therefore, these heat pumps are not directly connected to the consumer's fixtures but are instead linked to a stratified storage tank. This tank enables drawing water at specific temperatures thanks to thermal stratification. Utilizing a storage tank in DH applications is unusual; however, due to the fixed-speed operation of the compressor, which does not directly adapt to fluctuating demands, a storage tank becomes necessary to buffer these variations. The water circuit configuration is identical across all three heat pump models. It includes a single tank that acts as the thermal reservoir for both DH and DHW.

A water stream ($\dot{m}_{HP}$) is pumped from the tank's bottom to the GC/COND where it gets heated before returning to the tank. From the water tank, two circuits depart to reach the user. Both circuits are in closed-loop configuration, therefore after leaving the water tank, they will return to it at a different temperature after passing through the user. A pump draws water from the tank for the DH circuit. . Since the water temperature inside the tank will usually be at a different temperature, the extracted amount ($\dot{m}_{preDH}$) is mixed in a three-way valve with a recirculation stream from the DH system ($\dot{m}_{recDH}$). This allows the water stream to reach the inlet temperature of the DH system ($T_{in,DH}$) here fixed at 35 °C. The stream exits the DH system at the fixed temperature $T_{out,DH}$ and the stream that is not recirculated returns back to the storage tank. A third pump directs a stream of water ($\dot{m}_{DHW}$) from the top of the tank to the DHW brazed plate heat exchanger, where it heats the water coming from the supply network at the

temperature T_{supply} = 10 °C to the required temperature (T_{DHW}). The water stream exits the heat exchanger at $T_{back,DHW}$ = 11 °C and returns back to the storage tank.

The tank's size is 700 L with a height of 2 m and a height to diameter ratio equal to 3 to maintain temperature stratification. The tank is insulated with a 0.05 m thick layer of material that has a thermal conductivity of 0.02 W/(m K). At the beginning of the simulation, the water temperature inside the tank is set at 20 °C. The storage tank is divided in 20 layers. The incoming water line from the heat pump and the outgoing DHW line are connected to layer 1, located at the top of the tank. The outgoing DH line is located in layer 3. The returns of DHW and DH lines, as well as the water line to the heat pump, are located at the bottom part of the tank (layer 20). For the DHW production, T_{DHW} and T_{supply} (see Figure 1) are set to 50 °C and 10 °C, respectively. The temperature approach between T_{supply} and $T_{back,DHW}$ (see Figure 1) is fixed at 1 K. For the domestic heating, it has been assumed a floor heating system with water flowing from 35 °C ($T_{in,DH}$) to 30 °C ($T_{out,DH}$).

The heat pumps always produce hot water at 60 °C and work with a constant compressor speed of 50 Hz. The compressor's ON/OFF cycling is controlled by the temperature measured at a specific layer inside the tank: layer 2 ($sensor_{onDHW}$) and layer 18 ($sensor_{on/off\ DH}$). The compressor turns ON when the temperature of layer 2 falls below 55 °C or the temperature of layer 18 is less than 32 °C to ensure the desired DHW and DH temperature, respectively. The compressor switches OFF when a temperature of 35 °C is reached in layer 18.

In the gas cooler, the high pressure is not set at a constant value but it is optimized with an iterative procedure: at each time step the COP is calculated for a range of high pressure between 80 to 100 bar and the value of pressure resulting in the highest COP is selected as the operating pressure. A similar procedure is implemented to optimize the subcooling in the condenser by selecting a value of subcooling within the range 5-40 K.

The simulation time-step was fixed to 1 minute.

5.3 Numerical model

The numerical models of the R290 and R744 heat pumps have been developed in MATLAB and display slight variations due to their different configurations. Models are built around the resolution of the reference thermodynamic cycle, with key points established based on energy conservation equations applied across the individual components. Shared inputs for both

models include the water inlet and outlet temperatures at the GC/COND, as well as external conditions such as air temperature and solar irradiance. Specific to the R290 heat pump is the input of subcooling at the COND, while for the R744 model the input is the high pressure at the GC. The outputs from both models include the refrigerant's thermodynamic properties throughout the cycle, along with the power consumption, heating capacity and COP of the heat pump.

At the beginning of the code, the n° of discretization is set at n = 20, while water temperature and air temperature start from a value of 20 °C. The control system in the water tank is defined, by specifying the position of the water extractions and of the temperature sensors. The heat pump works based on the load conditions and the operative mode of the heat pump system, independently from the value of the air temperature, as hot water is not only necessary for domestic heating but also for DHW, which is needed in all the environmental conditions. The size of the water storage tank is specified, defining its height and HD ratio. It has been found that different proportions lead to a different behaviour when it comes to the stratification quality.

As indicated in [25] the different cycle configuration (subcritical vs. supercritical) of the R290 and R744 heat pumps determines different components design, to carry out the test in comparable operating conditions. This applies to the heat exchangers, sized so that the temperature differences between air and refrigerant (at the evaporator) and refrigerant and water (at the gas cooler/condenser) are the same in both heat pumps at the design conditions. This approach is fundamental to highlight the performance difference of the two fluids.

The solution algorithm starts by setting first-attempt values for the evaporation temperature and superheating at the compressor suction. The COMP sub-model calculates the refrigerant mass flow rate and the discharge enthalpy. Following this, the GC/COND sub-model determines the refrigerant enthalpy at the outlet and the water mass flow rate. The IHE sub-model then adjusts the superheating at the compressor inlet and the enthalpy at the EEV inlet. The evaporator sub-model updates the evaporation temperature. This cycle continues, starting again from the COMP sub-model and repeating until convergence values for the evaporation temperature and superheating are found.

Based on the temperature sensors measurements of water temperature inside the tank, the control system ensures that the heat pump runs when it's supposed to, and water from the

storage tank is supplied to the user at two different temperatures. Return water temperature from the users are defined as 11 °C from the DHW usage and 30 °C from DH usage. Iterations are carried out on a 1 minute basis, starting from the given input of T_{air} and GTI, used to evaluate the performance of the evaporators. The electric power produced by the PV modules is evaluated at each iteration, by calculating the sequence T_{cell}, η_{PV} and P_{PV}:

$$T_{cell}(time) = T_{air}(time) + \frac{NOCT-20}{800*G(time)} \quad (5.2)$$

$$\eta_{PV}(time) = \eta_{stc} * (1 - \gamma * (T_{cell}(time) - 25)) \quad (5.3)$$

$$P_{PV} = G(time) * A_{PV} * n_{PV} * \eta_{PV}(time) \quad (5.4)$$

This power can be fed to the heat pump compressor directly, or when the heat pump is not working it can be stored if a battery storage system is present and then used when needed.

The brazed plate heat exchanger sub-model is used for COND, GC and IHE and it adopts a physical approach where the volume is discretized into small elements and each is treated as an individual heat exchanger, where the continuity and energy equations are solved, neglecting the pressure drop. This discretization approach has already been described and validated for the experimental system described in the previous chapters. In the GC model, the iterative procedure allows to determine the temperature and enthalpy at the outlet of the heat exchanger given the high-pressure. In the COND model, the same procedure is used with the subcooling as the constraint. The condensation pressure is updated after the COND model. The heating capacity produced by the heat pump at the COND or at the GC is calculated by the energy balance at the refrigerant side, knowing the difference between the inlet/outlet enthalpy

$$Q_{HP} = \dot{m}_r(h_{in} - h_{out}) \quad (5.10)$$

5.3.1 Finned coil evaporator

The finned coil evaporator consists of several coils in parallel attached to plain fins, where the refrigerant flows inside the tubes and air flows through them on the outside, in forced convection thanks to the presence of a fan. Tubes are typically made of copper or stainless steel, fins of aluminum.

A distributor ensures proper distribution of the two-phase mixture among the circuits, by introducing a local pressure drop, which by being right after the EEV does not represent a

problem for the exergy efficiency of the cycle, and thus doesn't penalize the performance of the system. The finned coil heat exchanger is modelled following a distributed parameter approach, that accounts for pressure drops. The three-dimensional discretization is described in the following.

The heat exchanger volume is divided into rows (N_r) and tubes per rows (N_t), with each tube further discretized into N_d longitudinal segments.

The discretization is geometrical, therefore each element has a fixed length. Each element, treated as an independent heat exchanger, sequentially calculates output conditions based on input from the previous element along the refrigerant path.

The main output of the model is the T_{ev}, obtained by convergence following a guessing/correction algorithm. The calculation begins from the following inputs:

- Refrigerant mass flow rate ($\dot{m}_{ref}$)
- Refrigerant enthalpy at the inlet (h_4)
- Secondary fluid inlet conditions ($\dot{m}_{air}, T_{air}$)
- Desired superheating at the evaporator outlet

The calculation iterates until the refrigerant enthalpy at the outlet ($h_{out,r,j}$) converges. This algorithm is repeated for subsequent discretizations along the refrigerant path until the circuit's end. The resulting refrigerant enthalpy at the outlet determines the superheating, evaluated using the REFPROP subroutine. If the calculated superheating is higher than the desired one, the saturation temperature at the inlet is increased, whereas if the calculated superheating is higher than the desired one, the saturation temperature at the inlet is decreased.

If refrigerant outlet conditions differ, the mass flow rate per circuit is iteratively corrected until the same pressure is found at each outlet element. The heat exchanger model is divided into three zones: evaporation, dry-out, and superheating. The inlet vapor quality of each element determines the heat transfer process, with correlations from Liu and Winterton for the evaporation zone, and Gnielinski correlation for the single-phase region (superheating).

5.3.2 Compressor sub-model

The compressor is modelled considering polynomial expressions for the electrical power consumption P_c and the mass flow rate processed $\dot{m}_r$, according to the standard for compressors

$$Y = C_1 + C_2S + C_3D + C_4S^2 + C_5SD + C_6D^2 + C_7S^3 + C_8S^2D + C_9SD^2 + C_{10}D^3 \quad (5.14)$$

where the coefficient values have been obtained from the compressor manufacturer for R744 and R290 compressor, for a suction compressor superheating (SH) of 10 K. S corresponds to the evaporation temperature at the suction dew point (T_{evap} in [°C]) while D corresponds to the discharge pressure (p_{GC} in [bar]) for R744 compressor and the condensing temperature at the suction dew point (T_{COND} in [°C]) for R290 compressor. To account for the SH, the mass flow rate can be corrected with the density ratio:

$$\dot{m}_r = \frac{\rho_{suction}}{\rho_{SH10}} * \dot{m}_{r,SH10} \quad (5.15)$$

where SH10 is referred to 10 K suction superheating condition.

5.3.3 Water storage tank

The storage tank model is constructed by considering heat transfer based on both conduction and forced convection while neglecting natural convection. The concept of discretization is applied, dividing the tank into *n* layers along its height, each representing a node. Each layer exchanges heat with its adjacent upper and lower layers. It is assumed that the temperature within each layer is uniform, thereby neglecting radial heat transfer. The change in heat content in the layers depends on the inflow and outflow impacts, including flows from the heat pump, DH and DHW, as well as interactions with nearby layers. Heat transfer in each layer is influenced by mass flow rates at the upper interface *(i-1,i)* as well as lower interface *(i, i+1)*.

$$\dot{m} = \dot{m}_{HP} + \dot{m}_{DH} + \dot{m}_{DHW} \quad (5.16)$$

If $m_i > 0$ the flow is downwards, while if $m_i < 0$ the flow is upwards. The heat balance of a layer is described by the following equations:

$$\rho V c_p \frac{dT}{dt} = Q_{flow} + Q_{cond} + Q_{conv} - Q_{loss} \quad (5.17)$$

where:

- V: volume of the layer
- c_p: specific heat capacity of the fluid
- $\frac{dT}{dt}$: rate of temperature change in the layer

Q_{flow} is the sum of the heat inflows and outflow of the heat pump, DHW and DH water loops, depending on the relative mass flow rate and water temperature

$$Q_{flow} = \sum \dot{m}_{flow} c_p T_{flow} \tag{5.18}$$

Q_{cond} are the heat flows transferred by conduction between adjacent layers

$$Q_{cond} = Q_{cond,(i-1,i)} + Q_{cond,(i,i+1)} \tag{5.19}$$

where *i* is the layer considered, *(i-1)* is the upper and *(i+1)* lower ones:

$$Q_{cond(i-1,i)} = \frac{\lambda A_i (T_{i-1} - T_i)}{H_i} \tag{5.20}$$

$$Q_{cond(i,i+1)} = \frac{\lambda A_i (T_{i-1} - T_i)}{H_i} \tag{5.21}$$

Q_{conv} are the heat flows transferred by convection due to mass inflows and outflows in the layer for the net mass flow ($\dot{m}_i$) forced in the tank. If it is downwards (*down*) or upwards (*up*) it is:

$$Q_{conv,down} = \dot{m}_i c_p (T_{i-1} - T_i) \tag{5.22}$$

$$Q_{conv,up} = \dot{m}_i c_p (T_i - T_{i+1}) \tag{5.23}$$

Q_{loss} represents the heat lost to the surroundings due to conduction between the layer and the external ambient, corresponding to a cylindrical geometry:

$$Q_{loss} = \frac{2\pi \lambda_{wall} H_i (T_i - T_{amb})}{\ln\left(\frac{\frac{D}{2} + l_{wall})}{\frac{D}{2}}\right)} \tag{5.24}$$

The DH system layout aims at guaranteeing a temperature inlet $T_{in,DH}$ and outlet $T_{out,DH}$ when a thermal load Q_{DH} is required. Depending on Q_{DH}, the required amount of water is extracted from the storage tank and sent to the user:

$$\dot{m}_{user_H} = \frac{Q_{user_H}(time)}{c_{p_{userH}} * (T_{w,inH} - T_{w,outH})} \tag{5.25}$$

This represents the amount of water required by the user, while the actual amount extracted will depend on the water temperature. In fact, water must be delivered at 35 °C, therefore a certain amount should be recirculated, depending on the temperature of the water extracted from the tank according to the energy balance:

$$\dot{m}_{ricH}(time) = \dot{m}_{userH}(time)\frac{c_{p,inH}T_{w,inH} - c_{p,out\ userH} * T_{l,out\ userH}(time)}{c_{p,outH}T_{w,outH} - c_{p,out\ userH} * T_{l,out\ userH}(time)} \quad (5.26)$$

where:

- $\dot{m}_{ricH}(time)$: mass flow rate of water recirculated at a the iteration
- $\dot{m}_{userH}(time)$: the mass flow rate of userH at the same time
- $c_{p,inH}$ is the specific heat capacity at the inlet for H
- $T_{w,inH}$ is the temperature at the inlet for H
- $c_{p,out\ userH}$ is the specific heat capacity at the outlet for userH
- $T_{l,out\ userH}(time)$ is the temperature at the outlet for userH as a function of time
- $c_{p,outH}$ is the specific heat capacity at the outlet for H
- $T_{w,outH}$ is the temperature at the outlet for H

From the mass balance, the model calculates the mass flow rate exiting the storage tank, considering the amount recirculated and the actual amount reaching the user:

$$\dot{m}_{preuserH}(time) = \dot{m}_{userH}(time) - \dot{m}_{ricH}(time) \quad (5.27)$$

where

- $\dot{m}_{preuserH}(time)$: mass flow rate of water reaching the user at the instantaneous time.
- $\dot{m}_{userH}(time)$: instantaneous mass flow rate of water exiting the storage tank for DH.
- $\dot{m}_{ricH}(time)$: mass flow rate of water that is recirculated to guarantee 35 °C at the inlet of the DH service

The DHW system layout aims instead at ensuring water heating from the supply temperature (T_{supply}) to a defined DHW temperature (T_{DHW}) in a heat exchanger when a specific water flow rate ($\dot{m}_{DHW}$) is required. The mass flow rate of water extracted from the storage tank for DHW reasons is expressed by

$$\dot{m}_{preuserDHW}(time) = \frac{Q_{userDHW}(time)}{c_{p,preuserDHW}(T_{l,out\ userDHW}(time) - T_{w,out,DHW})} \quad (5.28)$$

where

- $c_{p,preuserDHW}$: specific heat capacity of water as calculated in …
- $T_{l,out\ userDHW}(time)$: temperature of the water exiting the storage tank at the DHW extraction point
- $T_{w,out,DHW}$: temperature of the water for DHW production, in the return line to the storage tank

and with the heat load for DHW reasons $Q_{userDHW}$ calculated as

$$Q_{userDHW} = \dot{m}_{DHW} c_p (T_{DHW} - T_{supply}) \tag{5.29}$$

where $\dot{m}_{DHW}$ indicates the water flow rate required by the user at the temperature T_{DHW}.

A control is done also on the water temperature in the tank. The goal is to always have water hot enough to satisfy the load. This should be achieved by the system, but if at some point the water temperature is lower than required values, the auxiliary heating resistances switch on. This happens when

$$T_{l,out,userH}(time) < T_{w,inH} \tag{5.30}$$

or

$$T_{l,out,userDHW}(time) < T_{w,inH} \tag{5.31}$$

Considering $c_{p,userH}$ as calculated in Equation (…) the heating power consumption of the electrical resistance is expressed as:

$$P_{R,DH}(time) = \dot{m}_{userH}(time) * c_p * (T_{winH} - T_{out\ userH}) \tag{5.32}$$

and equivalently

$$P_{R,DHW}(time) = \dot{m}_{userH}(time) * c_p * (T_{winH} - T_{out\ userH}) \tag{5.33}$$

The storage tank's capacity is a critical factor in the heat pump system's ability to meet the thermal demands for domestic heating (DH) and domestic hot water (DHW). The tank's size is directly proportional to the heat stored, which is a function of the water's mass flow rate and

enthalpy. Ensuring the heat is delivered at the appropriate temperature for the intended application is essential.

The user's comfort level can be defined as the ratio of hours during which the system satisfies the thermal demand to the total number of hours in the period considered. This study aims at developing a system that ensures 100 % comfort level without the use of an electric resistance auxiliary heater. The storage tank serves as a thermal buffer, granting the system increased flexibility. In instances of sudden load spikes, the tank must contain sufficient water at the necessary temperature to fulfil the demand. Failure to do so would necessitate the activation of the resistance heater, potentially leading to user discomfort due to inadequate water temperatures. The heat pump's control system is designed with precise logic to heat the water at optimal moments. For example, the system is programmed to activate the heat pump when the water temperature at a specific level in the tank drops below 35 °C. This stratification ensures that the water above this level remains at a higher temperature.

The DHW controller, located at 80% of the tank's height, activates the heat pump when the temperature falls below 55 °C, while the space heating controller, positioned at 10% of the tank's height, operates between 30 °C and 35 °C. This dual-sensor system maintains proper stratification within the tank and prevents the lower section from becoming too cold, which is crucial for meeting peak hot water demands without engaging the auxiliary resistance heater. The COMP switches on if either of the conditions is true and switches off when both are false.

The storage tank model employs spatial discretization along its height, divided into 20 nodes, with a calculation time step of one minute. The gas cooler's high pressure is dynamically optimized, with the COP calculated at each time step for pressures ranging from 80 to 100 bar. The pressure yielding the highest COP is selected for operation. Extensive research has determined that the sensor's position significantly influences the resistance heater's activation more than the tank's size.

The balance between the mass flow rate of hot water supplied by the heat pump and the returning cold water from the user's circuit is critical for maintaining the system's efficiency. The predominance of cold water entering from the bottom can result in hot water accumulating at the top of the tank. Consequently, the strategic placement of the temperature sensor is essential. If the sensor is positioned too low, the heat pump may activate too frequently, increasing power consumption and consequently reducing the SCOP. Conversely, if the sensor

is placed too high, the heat pump may not engage often enough, failing to heat an adequate volume of water. This can lead to the activation of the auxiliary resistance heater or, worse, cause discomfort to the user due to insufficient hot water supply.

Considering n = 20 discretizations, the optimal position for the sensors and for the extraction of the water from the tank has been identified as:

- N_{DHW} = 1 for DHW circuit water extraction
- $N_{DHW,on}$ = 2 for DHW circuit temperature sensor
- N_{DH} = 3 for DH circuit water extraction
- $N_{DH,on}$ = 18 for DH circuit temperature sensor
- N_{off} = 18 for temperature sensor switching off the heat pump

These values were determined through multiple simulations with sensors placed at different heights. The optimal position chosen minimizes resistance power consumption. For the DH-only tests, N_{DH} = 1, as the entire hot water content of the tank is utilized for the DH user. In other cases, where both DH and DHW are needed, N_{DH} is set to 3 to reserve the hottest water for the DHW user.

5.4 Heat pump design

The design procedure for the R744-AHP and R290-AHP requires the selection of the COMP displacement, GC/COND number of plates N_{plates}, the finned coil size (number of circuit, tube length and number of fan). The R744-SAHP requires instead the slection of the number of PV/T collectors, while the GC and COMP remain the same as in the R744-AHP design. The GC and COND brazed plate heat exchangers use 379 cm x 79 cm plates, while the IHE, which has not been considered in the design process is modelled as a brazed plate heat exchanger with 4 plates of 377 cm x 12 cm. The finned coil tubes have an outer diameter of 10.12 mm and a thickness of 0.35 mm, distributed with a row spacing of 21.65 mm and tube spacing of 25 mm. The fins have 0.12 mm thickness and 3.2 mm spacing. A single fan has a diameter of 350 mm, a fixed airflow of 1645 m3/h with a power consumption of 66 W. The appropriate compressor size for the two different refrigerants was identified using the Frascold SPA selection software of single-stage reciprocating compressors [34], which also provides the coefficients used in equation (5.14). Due to the different refrigerant properties, the displacement of the R290-AHP compressor is 5 times larger than that of the R744-AHP and R744-SAHP. The specific

compressor work is evaluated assuming a compressor electric efficiency of 0.95. Regarding the PV/T evaporator, the NOCT has been modified from 44 °C given by the manufacturer to 24 °C to account for the cooling effect of the evaporator, as resulting from the measurements reported in [35]. This effect results in a 1 % increase in the electrical conversion efficiency of the PV system.

The three heat pumps have been designed to work in a Mediterranean climatic region (Rome weather conditions have been assumed as reference) with a nominal heating capacity of 15 kW at the design conditions of 7 °C air temperature and 10/60 °C water temperature at the GC/COND. Some additional design conditions have been imposed for the single heat pumps:

- For the R290-AHP, a fixed subcooling (SC) of 40 K inside the condenser has been imposed, based on the experimental data of Pitarch et al. [36] for a R290 heat pump working under similar operating conditions
- For the R744-AHP and R744-SAHP, a fixed high pressure value of 90 bar has been imposed
- For the R744-SAHP, a solar irradiance equal to 350 W/m^2 was assumed, corresponding to the mean value in Rome during the heating season

Starting from the R290-AHP and R744-AHP, the heat exchangers have been sized in order to get the same temperature difference between air and evaporating temperatures (ΔT_{evap}) abd between GC/COND outlet and water inlet temperatures (ΔT_{cond}). Furthermore, a SH of 9 K has been fixed. The size of the components was determined through multiple iterations of the numerical model of the heat pump until the ΔT_{evap} and ΔT_{cond} values were similar for both the heat pumps, with a maximum deviation of 0.5 K.

Following this, the R744-SAHP was equipped with the same components and component sizing as the R744-AHP, with the addition of the PV/T collectors. This assumption allows the R744-SAHP to achieve the nominal heating capacity even when solar radiation is not available, i.e. when the PV/T collectors do not work as an evaporator. The PV/T collectors have been chosen to produce approximately 3 kW of electrical power, under nominal conditions. Table 5.1 shows the results of the design process for the components of the three heat pumps. The corresponding COP in the design condition is equal to 3.9 for the R290-AHP and the R744-AHP and 4.2 for the R744-SAHP. The R290 heat pump realizes a COP similar to that of the R744-AHP because the condenser has a higher number of plates (corresponding to a higher heat transfer area)

according to the conditions fixed for the design. The R744-SAHP has the highest COP because the air and solar evaporators are operating simultaneously, and this increases the evaporating temperature reducing the power consumption of the compressor.

Table 5.1 - Design results of the three heat pumps

Component	Properties	Units	R290-AHP	R744-AHP	R744-SAHP
Compressor	Model		D3-15.1AXH	D4-3TK	D4-3TK
	Number of pistons	-	2	2	2
	Displacement	m^3/h	15.36	3.00	3.00
	Speed	rpm	1450	1450	1450
Gas-cooler/ Condenser	Number of plates	-	65	38	38
	Area	m^2	1.75	1.02	1.02
	ΔT_{cond} (design)	K	4.52	4.26	8.30
	Capacity (design)	kW	15.14	15.01	15.77
Evaporator	Type	-	Finned coil	Finned coil	Finned coil+PV/T
	Tube length	m	2	1.7	1.7
	Number of circuit	-	6	6	6
	Number of fan	-	3	3	3
	KA	W/K	1492	1273	1335
	Number of PV/T	-	0	0	11
	PV/T area	m^2	0	0	11.44
	ΔT_{evap} (design)	K	8.98	8.64	5.59
	Capacity (design)	kW	14.92	12.73	13.35
Heat pump	COP (design)	-	3.97	4.01	4.19

The heating load has been defined based on Rome, characterized by a mild climate. The Test Reference Year data for this location has been obtained from the Energyplus database and the hourly data of air temperature and global irradiance on the tilted plane of the PV/T collectors are plotted in Figure 5.5. The seasonal simulation covers only the heating season, defined from November 1st to April 15th (166 days).

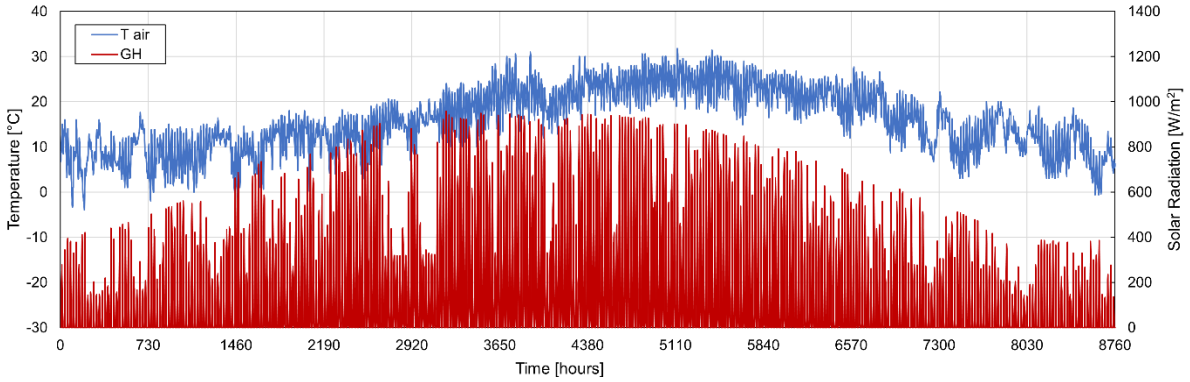

Figure 5.5 – Annual air temperature and global irradiance on the tilted plane in Rome

The heat pump's performance has been simulated also based on the climatic conditions of Strasbourg, which correspond to an average climatic zone reference (Figure 5.6). Given the different climatic conditions throughout the year, the heating season has been extended from October 1st to May 15th (227 days).

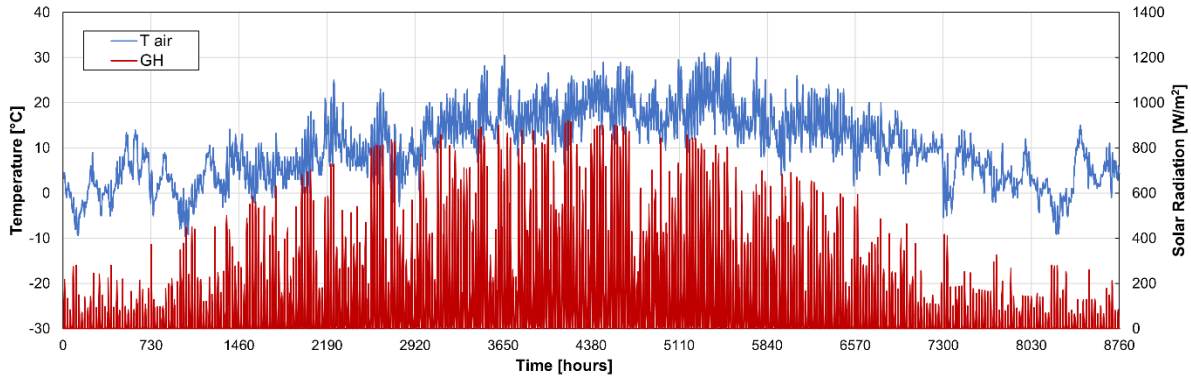

Figure 5.6 - Annual air temperature and global irradiance on the tilted plane in Strasbourg

The DH load profile of the simulated building was derived from a linear equation as a function of outdoor air temperature. A maximum DH load of 10 kW is imposed at an air temperature of -10 °C, which corresponds to the minimum temperature found in Strasbourg, while the DH load is 0 kW at 18°C. No heating demand is present when the outdoor air temperature is above 18°C. The same curve has been used for the DH load of Rome, where the maximum load is found at -4 °C, equal to 7.35 kW. It has been assumed that the DH load is required during daylight hours, from 7am to 10pm, thus there is no DH load demand during the night hours. The total seasonal hours of DH load are 2415.5 for Rome and 3277 for Strasbourg. The seasonal DH demand requirements in Rome is 7429 kWh, which averages to 44.8 kWh per day, while in Strasbourg is 13574 kWh, which averages to 59.8 kWh per day.

The DHW demand of the simulated-building was modeled as a time-dependent function with values defined at 5-minute intervals. The load profile is given on a weekly basis, with two different profile distribution for working days (from Monday to Friday) and weekend days (Saturday and Sunday). During the working days, the DHW demand is concentrated in three time zones: early morning, lunchtime and evening. On the other hand, during the weekend, the DHW demand is well distributed throughout the day. It has been assumed that the DHW load is required only during the daytime, from 7am to 10pm, as imposed for the DH load profile. For annual simulations, the weekly DHW load profile is repeated identically throughout the year and it is independently from the location selected. The average DHW load is 18.65 kWh per day, while the total seasonal hours of DHW load are 589 in Rome and 820 in Strasbourg.

5.5 Results

Seasonal simulation has been conducted to examine three combinations for coupling the previously defined loads:

1) Demand for only DH with null DHW (DH)
2) Demand for DH with 30 % DHW (DH DHW30)
3) Simultaneous demand for both DH and DHW loads (DH DHW)
4) Demand for DHW with 30 % DH (DH30 DHW)
5) Demand for only DHW with null DH (DHW)

Figure 5.8 compares the SCOP values of the three heat pumps under the five different thermal load conditions in Rome. It can be observed that the highest SCOP is always obtained for the R290-AHP and the lowest for the R744-AHP, regardless of the thermal load. Additionally, as the share of DHW load versus DH load increases, the performance of all the three heat pumps increases as well. However, as the share of DHW on the total heat load increases, the SCOP increase is higher for the CO_2 heat pumps compared to the propane heat pump.

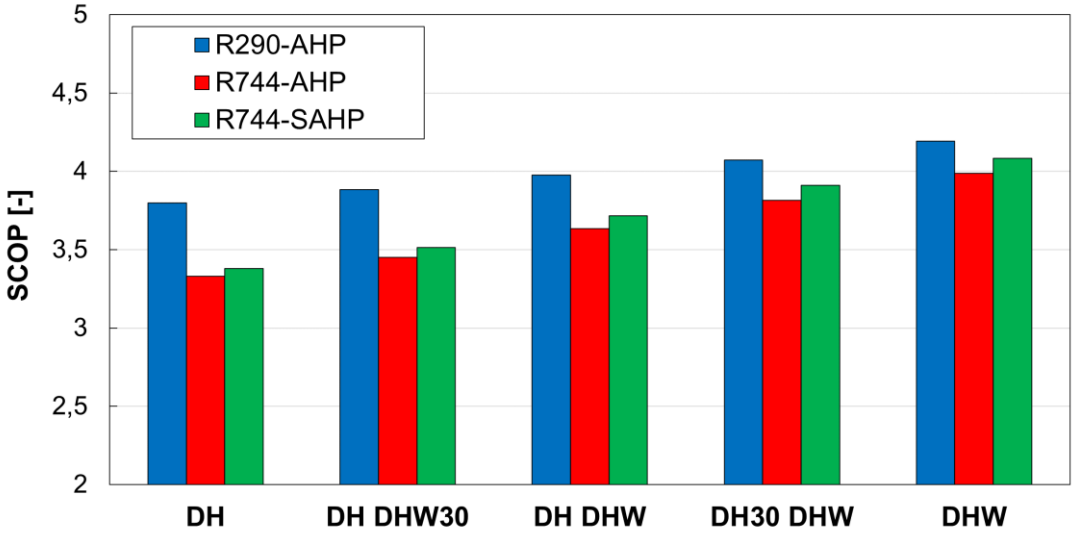

Figure 5.8 – SCOP of the three heat pumps in Rome under various load conditions: only DH load, only DHW load, DH+DHW load, DH at 30% with full DHW load, and DHW at 30% with full DH load

The rise in SCOP is not linked to an increase in thermal energy generated by the heat pump, as they all produce the same heating during the season, but rather to a reduction in electrical consumption. As shown in Table 5.1 (ΣP_{tot}) the R290-AHP consumes approximately 14 % less for DH load and 5.4 % less for DHW load compared to the R744-AHP.

Values of electrical energy produced by the PV modules (ΣP_{PV}) is also reported in Table 5.1. The use of PV/T in the R744-SAHP, which cools the cells by means of the evaporating refrigerant, results in a higher electrical energy production compared to the use of only PV modules combined with the two AHPs. Specifically, there is an increase of 1.6 % for DH+DHW load, 0.9 % for DH load and 0.6 % for DHW load. The performance increase is present but limited for two reasons. Firstly, PV/T collectors only work as PV modules when the heat pump turns off, without the cooling benefit of the circulating refrigerant on the electrical conversion efficiency. Secondly, the R744-SAHP does not always run during hours of production of the PV modules, thus the cooling benefit cannot always be exploited. In fact, during the heating season the PV system operates for approximately 1189 hours, while the operation in PV/T mode is limited to 210 hours in DH+DHW, 164 hours in DH and 69 hours in DHW.

Table 3.2 – Results for the seasonal simulation, Rome

Load	HP	Σ Q_{HP} [MWh]	Σ P_{tot} [MWh]	Σ P_{PV} [MWh]
DH	R290-AHP	6.035	1.800	1.592
	R744-AHP	6.034	1.829	1.582
	R744-SAHP	5.951	1.566	1.585
DH + 30 % DHW	R290-AHP	6.944	2.014	1.594
	R744-AHP	6.946	2.051	1.582
	R744-SAHP	6.918	1.788	1.585
DH + DHW	R290-AHP	9.124	2.550	1.594
	R744-AHP	9.124	2.605	1.582
	R744-SAHP	9.089	2.319	1.585
30 % DH + DHW	R290-AHP	5.049	1.357	1.585
	R744-AHP	5.044	1.378	1.582
	R744-SAHP	5.013	1.251	1.585
DHW	R290-AHP	3.309	0.814	1.588
	R744-AHP	3.308	0.837	1.582
	R744-SAHP	3.255	0.782	1.585

Figure 5.9 shows the SCOP when the heat pump operation is simulated based on the climatic conditions and heating load of Strasbourg, while Table 5.3 presents the SCOP comparison of the three heat pump systems both in Rome and Strasbourg and in the five heating load conditions previously mentioned.

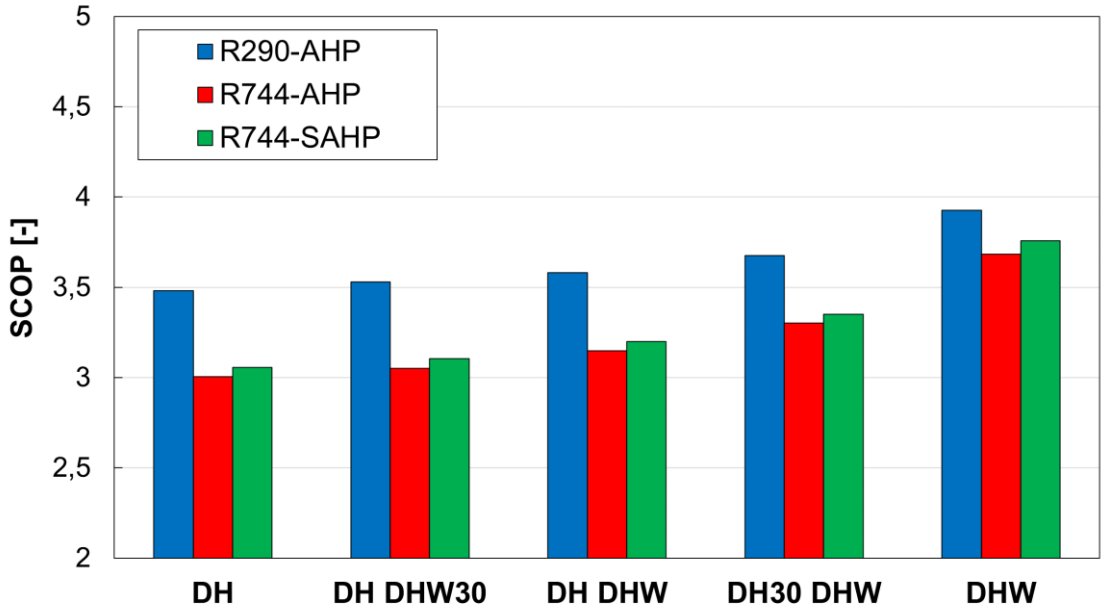

Figure 5.9 – SCOP of the three heat pumps in Strasbourg under various load conditions: only DH load, only DHW load, DH+DHW load, DH at 30% with full DHW load, and DHW at 30% with full DH load

Table 5.3 – SCOP comparison of the three heat pumps in Rome and Strasbourg under the different load conditions shown in Figure 5.9

Load	Rome			Strasbourg		
	R744-SAHP	R744-AHP	R290-AHP	R744-SAHP	R744-AHP	R290-AHP
DH	3.35	3.30	3.80	3.06	3.01	3.48
DH DHW30	3.44	3.39	3.87	3.11	3.05	3.53
DH DHW	3.58	3.50	3.92	3.20	3.15	3.58
DH30 DHW	3.72	3.66	4.01	3.35	3.30	3.68
DHW	4.07	3.95	4.16	3.76	3.68	3.93

The three heat pumps show comparable differences to the Rome case, however the absolute values of the SCOP is sensibly lower, due to the colder climate. The highest difference in SCOP due to the different scenario is found for the R744-SAHP in DH+DHW load, which loses 10.54 % compared to the same unit in Rome. The lowest difference is found instead for the R290-AHP in DHW, which has a SCOP 5.60 % lower than the same unit in Rome. For all the three heat pumps the most affected condition is the DH+DHW case, which shows a SCOP 10,54 %, 10,11 % and 8,66 % lower than in Rome, respectively for the R744-SAHP, R744-AHP and R290-AHP. As previously explained (§5.4) the heating load in Strasbourg is different than in Rome, in particular there is a higher share of DH on the total load. This application is the one affecting the most the heat pump's performance, as clearly highlighted by the not negligible

performance decrease compared to Rome, despite the environmental conditions not being significantly different.

Some dynamic results are presented to better understand the operation of the three heat pumps in presence of a combined DH+DHW load. Figure 5.10 displays the results of numerical simulations conducted over two consecutive days: a working day (day 1) and a weekend day (day 2). The environmental conditions, including air temperature (T_{air}) and global irradiance on the tilt plane of the PV/T collectors (G), varied between the two days (Figure 5.10a). Day 1 shows a high T_{air} (7 °C on average) and low G (maximum 340 W/m^2), while day 2 shows a low T_{air} (3 °C on average) and high G (maximum 790 W/m^2). Figure 5.10b shows that the required DH load varies depending on T_{air}, with a maximum of 5.4 kW for day 1 and 6.6 kW for day 2. In contrast, the DHW load has a different distribution depending on the day of the week, as explained in (§5.4), with a maximum of 9.6 kW for day 1 and 7.7 kW for day 2.

Figures 5.10c and 5.10d show the heating production (Q_{HP}) and electrical power consumption (P_{tot}). The R290-AHP produces a higher Q_{HP} than the R744 heat pumps (i.e. 1-2 kW more) despite they had to satisfy the same thermal energy demand equal to 172 kWh. As a result, the R290-AHP operates for less hours over the two days, specifically 12 hours 15 minutes, in comparison to the two R744 heat pumps, which operate 12 hours 55 minutes (R744-SAHP) and 14 hours 40 minutes (R744-AHP). Additionally, when comparing the two R744 heat pumps, it is evident that the R744-SAHP produces the same Q_{HP} and require the same P_{tot} in the absence of solar radiation. In contrast, when exposed to solar radiation (e.g. from 12 to 16 on day 2), the R744-SAHP enables greater Q_{HP} and P_{tot} than the R744-AHP. This is also reflected in the trend of the evaporation temperature, shown in Figure 5.10e (in this graph, when the heat pumps are not working the evaporating temperature is fixed to 0 °C).

Figure 5.10e shows that T_{ev} for the R744-SAHP is higher than that of the R744-AHP, and it further increases when G increases due to the contribution of solar evaporator source. Thus, to better exploit the advantages of the combined use of the solar and air source, the production of the heating capacity should be matched within the daylight hours in which the solar radiation is higher and thus avoiding the switch of the heat pump, even if this would require a larger thermal storage system. Additionally, it can be noted that, despite the higher T_{ev}, the R744-SAHP is not able to outperform the R290-AHP in terms of produced Q_{HP}. This may be explained by the larger heat transfer area of the condenser compared to the gas cooler (§5.4), which allows the heat pump to extract more heat from the hot refrigerant.

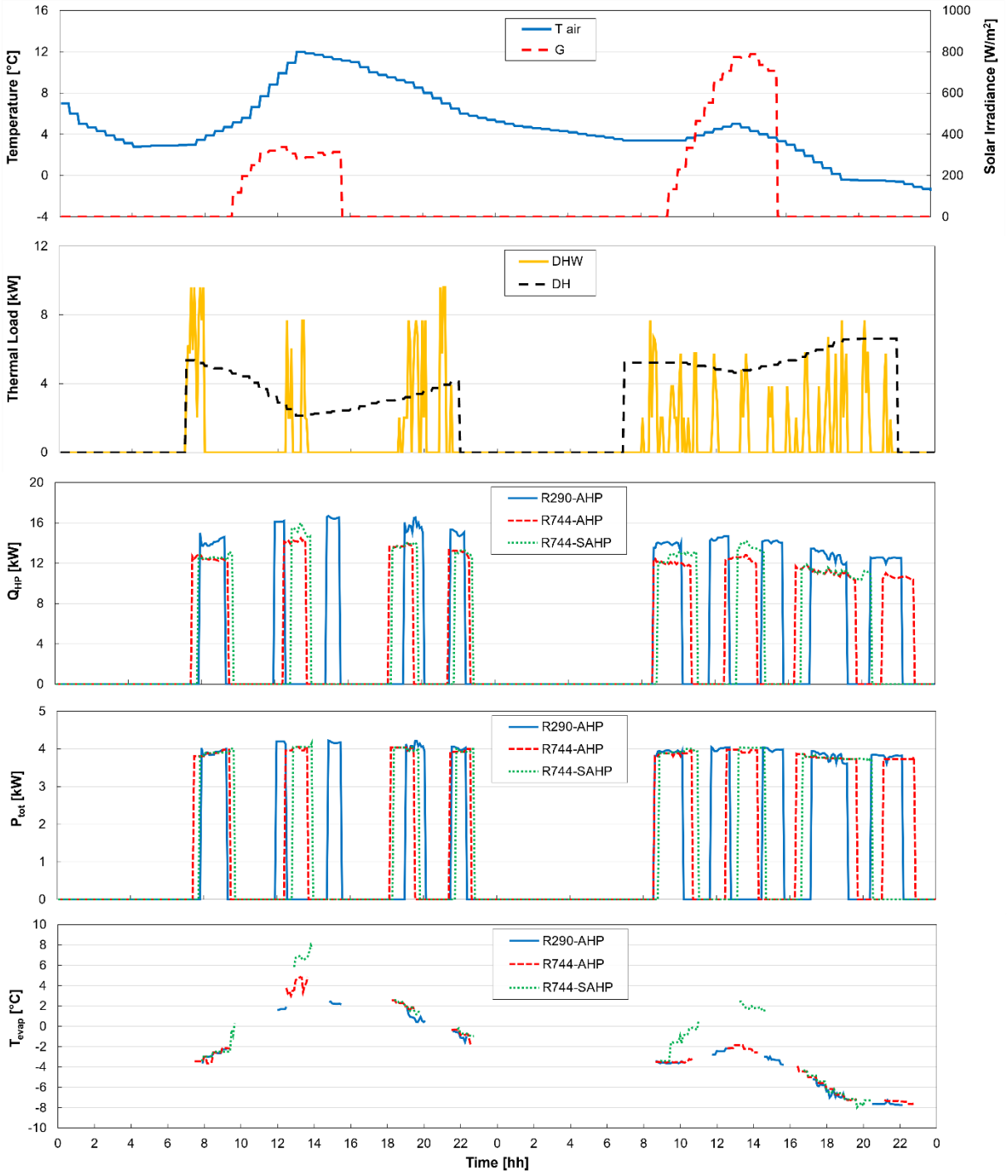

Figure 5.10 – Results of the simulations in Rome during two consecutive days with DH and DHW loads. From the top: a) air temperature and solar irradiance; b) DH and DHW loads; c) heating capacity; d) power consumption; e) evaporation temperature of the three heat pumps

In the present model the dehumidification and frosting at the evaporator have not been considered, however, the results in Figure 5.10e show the potential of the SAHP to reduce the possible defrosting cycles since the evaporating temperature is higher (this is the evaporating temperature in both the air and solar evaporators) compared to the AHP (green line compared to the red line in Figure 5.10e).

Figure 5.11 shows the detail of numerical results over two consecutive days for the three heat pumps in presence of DHW load. It can be clearly noticed how all the three heat pumps turn on less frequently, and the mismatch between the gas cooler capacity of the R290-AHP and the R744 heat pumps is strongly reduced.

This load condition is characterized by a water temperature profile which can better match with the profile of the CO_2 refrigerant at the gas cooler. This results in a better heat transfer and higher gas cooler capacity, improving the COP of the R744-AHP and R744-SAHP. The same concept applies also to the R290-AHP, which also can take advantage, even if in lower measure than the CO_2 heat pumps, of the higher water temperature difference compared to loads with higher DH share, as the condenser has been optimized for a subcooling of 40 K.

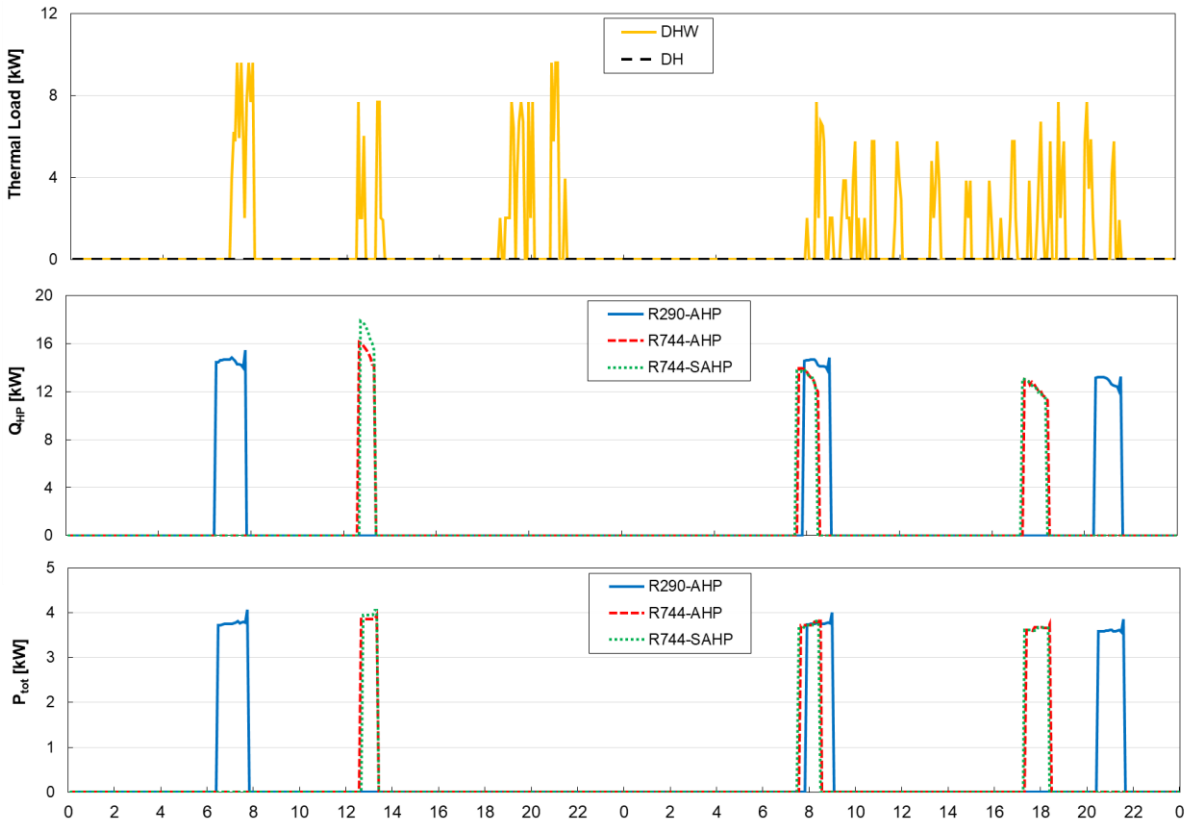

Figure 5.10 - Results of the simulations in Rome during two consecutive days with DHW load. From the top: a) DHW load; b) heating capacity; c) power consumption.

Figure 5.12 illustrates the temperature profiles recorded by some sensors installed inside the storage tank during the consecutive days in Figure 5.10 for the R744-SAHP. The 5 sensors are:

- $T_{TANK,DH}$: temperature of the water stream exiting the tank for DH load
- $T_{TANK,DHW}$: temperature of the water stream exiting the tank for DHW load

- $T_{sensor,onDH}$: temperature measured in the middle of the tank ($N_{sonda,onH} = 10$)
- $T_{sensor,off}$: temperature measured at the bottom of the tank ($N_{off} = 18$)
- $T_{sensor,onDHW}$: temperature measured at the top of the tank ($N_{onDHW} = 2$).

The $Tsensor_{onDH}$ triggers the heat pump to switch on when the measured temperature reaches 32 °C. It is evident that when this temperature is attained, water begins to heat throughout the entire storage tank. Since hot water is injected from the top, the water at the bottom takes longer to heat up, as indicated by the gentler slope of the $T_{sensor,off}$ curve. When this sensor measures a water temperature higher than 35 °C, the heat pump switches off, signifying that, due to stratification, 90 % of the tank's height above this sensor is at a higher temperature. $Sensor_{on,DHW}$ is positioned at the top of the tank to ensure water remains at a temperature above 55 °C for the DHW circuit. It activates the heat pump when the water temperature falls below 55 °C. However during the two days shown in the chart, it did not trigger. The two sensors $T_{TANK,DH}$ and $T_{TANK,DHW}$ confirm that the water is delivered to the circuit at temperatures exceeding the minimum required, thereby ensuring user satisfaction. These sensors also further demonstrate the stratification effect, as the water delivered for DHW, extracted at N=1, remains consistently around 60 °C. In contrast, the water temperature for DH, extracted at N=3, fluctuates between 44-60 °C.

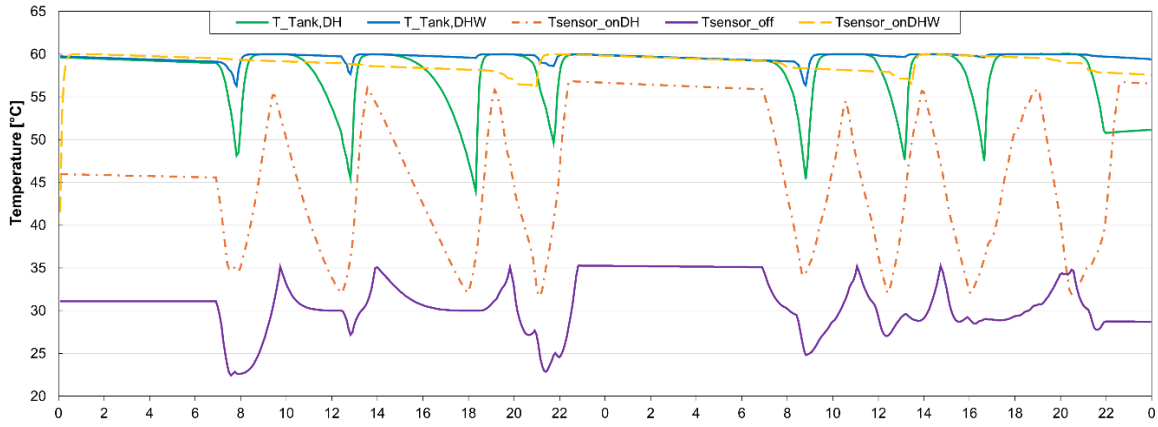

Figure 5.12 – Temperature profile for five different sensors placed in the hot water storage tank during the simulation of the two consecutive days in Figure 5.10 for R744-SAHP

Conclusions

In this thesis, a dual-source (solar-air) heat pump using CO_2 as refrigerant has been analyzed both experimentally and numerically. The heat pump operates in different evaporator modes, featuring a finned coil heat exchanger and three PV/T evaporators, enabling it to function in air-mode, solar-mode, and simultaneous-mode. In air-mode, the refrigerant flows directly to the finned coil heat exchanger via a distributor. In solar-mode, the refrigerant is collected into a low pressure receiver after passing through the EEV, and then the liquid refrigerant is extracted to evaporate in the PV/T evaporators. In simultaneous-mode, the refrigerant evaporates in both the finned-coil heat exchanger and the PV/T collectors.

The first goal of this thesis was to experimentally characterize the system performance, with a focus on the simultaneous-mode. Performance data were gathered under various environmental conditions (air temperature and solar irradiance) and system settings (water temperature difference at the gas cooler, high pressure value, compressor frequency). The results indicated that the COP increases by 0.036 per degree of water temperature increase through the evaporator, translating to a 1.08% COP decrease and 0.087 °C increase of the evaporation temperature per °C increase of ΔT_w. For each °C increase in air temperature, the heat pump's COP increases by 3.7%, and the T_{ev} rises by approximately 1 °C. Regarding solar irradiance, the COP increases by 1.7% per 100 W/m² increase. The simultaneous-mode outperformed the air-mode and solar-mode. When the air temperature was equal to 8.8 °C and solar irradiance equal to 850 W/m^2, the COP_{gen} increases of 6 % and 16.4% compared to the air-mode and solar-mode, respectively. Even at low solar irradiance (GTI = 180 W/m²), the simultaneous-mode showed a COP_{gen} increase of 5.2 % compared to air-mode.

The second goal was to validate the steady-state and dynamic models of the heat pump using the new experimental data. The results of the steady state model have been compared with the experimental data. When the heat pump was operating in simultaneous mode the average evaporation temperature error was 0.75 K, while the average COP_{gen} error was 2.51%, with nearly all tests within a 5% error range. With the heat pump operating in air-mode the evaporation temperature has shown an average error of 0.29 K, while the average COP error was 3.78%. The dynamic model also showed good performance prediction, with an average error of 0.64% for the gas cooler power and 0.29 K for T_{ev}. Dynamic validation in air-mode,

with the compressor frequency increased from 50% to 90% of the nominal value, showed a slight underestimation of T_{ev} after the second perturbation, with an average error of 0.94 K for the rest of the test. Gas cooler power prediction had an average error of 2.7%, while power consumption was very accurately predicted with an average error of 0.76%.

Finally, the third goal of the thesis was that of describing the seasonal performance of the CO_2 dual source heat pump system (R744-SAHP) while comparing it also with an air-source CO_2 system (R744-AHP) and a propane air-source system (R290-AHP). The analysis reveals that the rise in SCOP is primarily due to reduced electrical consumption rather than an increase in thermal energy generated. Among the heat pumps, the R290-AHP demonstrates superior efficiency, consuming significantly less energy for both DH and DHW compared to the R744-AHP. The R744-SAHP, enhanced by PV/T technology, generates more electrical energy than traditional PV modules, although this advantage is somewhat limited by operational constraints.

When comparing performance across different climates, all heat pumps show lower SCOP values in Strasbourg compared to Rome, with the R744-SAHP being the most affected. Dynamic simulations underscore the importance of operational strategies, highlighting that aligning heat pump operation with daylight hours can maximize the benefits of the solar evaporator. The R744-SAHP's higher evaporating temperature indicates potential for reduced defrosting cycles, although it still falls short of the R290-AHP in overall heating production.

Temperature stratification within the storage tank is effectively managed, ensuring that both DH and DHW requirements are met efficiently.

Appendix

Chapter 3

$$P_{gen_{flooded}} = P_{comp} + P_{pump} + 28.8 \quad (1)$$

$$P_{gen_{dry}} = P_{comp} + P_{fan} + 28.8 \quad (2)$$

$$P_{gen_{simultaneous}} = P_{comp} + P_{fan} + P_{pump} + 28.8 \quad (3)$$

Chapter 4

$$P_{comp} = fP(T_{evap}, p_{high}, f_{comp}) \quad (4)$$

with T_{ev} being the evaporation temperature, p_{high} the discharge pressure and f_{comp} the compressor frequency.

$$\begin{aligned} fP(x_1, x_2, x_3) = {} & 8.7982187 * x_3 + 0.051191237 * x_3^2 - 180.75873 * x_2 - 0.13015048 \\ & * x_2 * x_3 - 0.00012105516 * x_2 * x_3^2 + 2.4044842 * x_2^2 + 0.0017046925 \\ & * x_2^2 * x_3 - 20.28671 * x_1 + 0.17455746 * x_1 * x_3 - 0.0029651541 * x_1 \\ & * x_3^2 + 0.11437534 * x_1 * x_2 + 0.0020160275 * x_1 .* x_2 .* x_3 \\ & - 0.00036859409 * x_1 * x_2^2 + 1.0532872 * x_1^2 - 0.011378281 * x_1^2 * x_3 \\ & - 0.0082565303 * x_1^2 * x_2 + 4447.4581 * 1 - 0.011458934 * x_1^3 \\ & - 0.010359495 * x_2^3 - 1.4377916e - 05 * x_3^3 \end{aligned}$$

$$P_{fan} = 0.0411 * V_{vent}^3 + 1.3719 * V_{vent}^2 - 2.3277 * V_{vent} + 1.504$$

$$P_{pump} = 0.0267 * f_{pump}^2 - 0.0262 * f_{pump} + 0.1665$$

Nomenclature

PV/T = Photovoltaic/thermal evaporator

IHX = Internal heat exchanger / Regenerative heat exchanger

RTD = Resistance Temperature Detector

SAHP = Solar-assisted heat pump

IDX-SAHP = Indirect expansion solar-assisted heat pump

DX-SAHP = Direct expansion solar assisted heat pump

MPPT = Maximum Power Point Tracker

EEV = Electronic expansion valve

GTI = Global Tilted Irradiance

COP = Coefficient Of Performance

SF = Solar Fraction

PCM = Phase Change Materials

CO_2 = Carbon Dioxide

HFCs = Hydrofluorocarbons

GWP = Global Warming Potential

Bibliography

[1] Eurostat, “Renewable Energy statistics.” Accessed: May 15, 2024. [Online]. Available: https://ec.europa.eu/eurostat/statistics-explained/index.php?title=Renewable_energy_statistics

[2] “DIRECTIVE (EU) 2023/2413 OF THE EUROPEAN PARLIAMENT AND OF THE COUNCIL,” Brussels, 2023. Accessed: May 15, 2024. [Online]. Available: https://eur-lex.europa.eu/eli/dir/2023/2413/oj/eng

[3] I. - International Energy Agency, “World Energy Outlook Special Report The Future of Heat Pumps.” [Online]. Available: www.iea.org

[4] GSE, “Fuel Mix.” Accessed: May 09, 2024. [Online]. Available: https://www.gse.it/servizi-per-te/fontirinnovabili/ fuel-mix.

[5] E. Granryd, I. Ekroth, P. Lundqvist, A. Melinder, B. Palm, and P. Rohlin, *Refrigerating engineering*. Stockholm: Royal Institute of Technology, KTH, 2011.

[6] Sporn and Ambrose, “The heat pump and solar energy,” *Applied Solar Energy*, 1955.

[7] T. Li, Q. Liu, X. Wang, J. Gao, G. Li, and Q. Mao, “A comprehensive comparison study on household solar-assisted heating system performance in the hot summer and cold winter zone in China,” *J Clean Prod*, vol. 434, p. 140396, Jan. 2024, doi: 10.1016/J.JCLEPRO.2023.140396.

[8] J. Zhao *et al.*, “Solar radiation transfer and performance analysis of an optimum photovoltaic/thermal system,” *Energy Convers Manag*, vol. 52, no. 2, pp. 1343–1353, Feb. 2011, doi: 10.1016/j.enconman.2010.09.032.

[9] Z. Qiu, X. Zhao, P. Li, X. Zhang, S. Ali, and J. Tan, “Theoretical investigation of the energy performance of a novel MPCM (Microencapsulated Phase Change Material) slurry based PV/T module,” *Energy*, vol. 87, pp. 686–698, Jul. 2015, doi: 10.1016/j.energy.2015.05.040.

[10] A. James, M. Srinivas, M. Mohanraj, A. K. Raj, and S. Jayaraj, “Experimental studies on photovoltaic-thermal heat pump water heaters using variable frequency drive

compressors," *Sustainable Energy Technologies and Assessments*, vol. 45, p. 101152, Jun. 2021, doi: 10.1016/J.SETA.2021.101152.

[11] H. Yang, X. Wang, and S. Yao, "Thermodynamic analysis of a novel solar photovoltaic thermal collector coupled with switchable air source heat pump system," *Appl Therm Eng*, vol. 218, p. 119410, Jan. 2023, doi: 10.1016/J.APPLTHERMALENG.2022.119410.

[12] J. Cai, F. Zhang, and J. Ji, "Comparative analysis of solar-air dual source heat pump system with different heat source configurations," *Renew Energy*, vol. 150, pp. 191–203, May 2020, doi: 10.1016/J.RENENE.2019.12.128.

[13] S. Chinnasamy, K. B. Prakash, B. Kalidasan, and A. Sampathkumar, "Optimal utilisation of low-grade solar-air source for heat pump water heating using a dual-source evaporator with forced convection," *International Communications in Heat and Mass Transfer*, vol. 150, Jan. 2024, doi: 10.1016/j.icheatmasstransfer.2023.107174.

[14] R. Simonetti, L. Molinaroli, and G. Manzolini, "Experimental and analytical study of an innovative integrated dual-source evaporator for solar-assisted heat pumps," *Solar Energy*, vol. 194, pp. 939–951, Dec. 2019, doi: 10.1016/j.solener.2019.10.070.

[15] Z. Li and X. Huang, "Simulation analysis on operation performance of a hybrid heat pump system integrating photovoltaic/thermal and air source," *Appl Therm Eng*, vol. 200, p. 117693, Jan. 2022, doi: 10.1016/J.APPLTHERMALENG.2021.117693.

[16] W. Deng and J. Yu, "Simulation analysis on dynamic performance of a combined solar/air dual source heat pump water heater," *Energy Convers Manag*, vol. 120, pp. 378–387, Jul. 2016, doi: 10.1016/J.ENCONMAN.2016.04.102.

[17] United Nations Environment Programme, "Montreal Protocol on Substances that Deplete the Ozone Layer," Sep. 1987.

[18] United Nations, "Kyoto Protocol to the United Nations Framework Convention on Climate Change," Kyoto, Dec. 1997.

[19] United Nations, "Kigali Amendment to the Montreal Protocol On Substances that Deplete the Ozone Laye."

[20] R. U. Rony, H. Yang, S. Krishnan, and J. Song, "Recent advances in transcritical CO<inf>2</inf> (R744) heat pump system: A review," *Energies (Basel)*, vol. 12, no. 3, Jan. 2019, doi: 10.3390/en12030457.

[21] F. Leonforte *et al.*, "Design and performance monitoring of a novel photovoltaic-thermal solar-assisted heat pump system for residential applications," *Appl Therm Eng*, vol. 210, Jun. 2022, doi: 10.1016/j.applthermaleng.2022.118304.

[22] M. Tammaro, C. Montagud, J. M. Corberán, A. W. Mauro, and R. Mastrullo, "Évaluation de la performance saisonnière de systèmes de production d'eau chaude sanitaire fonctionnant au propane et de pompes à chaleur au CO2," *International Journal of Refrigeration*, vol. 74, pp. 222–237, Feb. 2017, doi: 10.1016/j.ijrefrig.2016.09.026.

[23] I. - International Energy Agency, "World Energy Outlook 2023," 2023. [Online]. Available: www.iea.org/terms

[24] US Department of Energy, " Commercial buildings energy consumption survey (CBECS)," 2015.

[25] M. Tammaro, C. Montagud, J. M. Corberán, A. W. Mauro, and R. Mastrullo, "Évaluation de la performance saisonnière de systèmes de production d'eau chaude sanitaire fonctionnant au propane et de pompes à chaleur au CO2," *International Journal of Refrigeration*, vol. 74, pp. 222–237, Feb. 2017, doi: 10.1016/j.ijrefrig.2016.09.026.

[26] F. J. S. Velasco, M. R. Haddouche, F. Illán-Gómez, and J. R. García-Cascales, "Experimental characterization of the coupling and heating performance of a CO2 water-to-water heat pump and a water storage tank for domestic hot water production system," *Energy Build*, vol. 265, p. 112085, Jun. 2022, doi: 10.1016/J.ENBUILD.2022.112085.

[27] L. Croci, L. Molinaroli, and P. Quaglia, "Dual Source Solar Assisted Heat Pump Model Development, Validation and Comparison to Conventional Systems," in *Energy Procedia*, Elsevier Ltd, 2017, pp. 408–422. doi: 10.1016/j.egypro.2017.11.153.

[28] F. Botticella and L. Viscito, "Seasonal performance analysis of a residential heat pump using different fluids with low environmental impact," in *Energy Procedia*, Elsevier Ltd, 2015, pp. 878–885. doi: 10.1016/j.egypro.2015.11.832.

[29] R. Trinchieri, M. Pieve, G. Boccardi, N. Calabrese, P. Rovella, and L. Saraceno, "Experimental analysis of a CO<inf>2</inf> heat pump for instantaneous domestic hot water production," *J Phys Conf Ser*, vol. 1599, no. 1, Sep. 2020, doi: 10.1088/1742-6596/1599/1/012059.

[30] J. Wang, M. Belusko, M. Evans, M. Liu, C. Zhao, and F. Bruno, "A comprehensive review and analysis on CO2 heat pump water heaters," *Energy Conversion and Management: X*, vol. 15. Elsevier Ltd, Aug. 01, 2022. doi: 10.1016/j.ecmx.2022.100277.

[31] Joint Committee for Guides in Metrology, "Guide to the Expression of Uncertainty in Measurement," 2008. Accessed: May 02, 2024. [Online]. Available: https://www.bipm.org/utils/common/documents/jcgm/JCGM_100_2008_E.pdf

[32] *Heat pumps with electrically driven compressors-Testing, performance rating and requirements for marking of domestic hot water units BSI Standards Publication*. 2017.

[33] E. Zanetti, M. Azzolin, R. Conte, S. Girotto, and D. Del Col, "Experiments and dynamic modelling of dry expansion and flooded evaporators in a CO2 solar assisted heat pump," *Appl Therm Eng*, vol. 217, Nov. 2022, doi: 10.1016/j.applthermaleng.2022.118964.

[34] Frascold, "FSS3, FRASCOLD SELECTION SOFTWARE."

[35] E. Zanetti, M. Azzolin, S. Girotto, and D. Del Col, "Performance and control of a CO2 dual source solar assisted heat pump with a photovoltaic-thermal evaporator," *Appl Therm Eng*, vol. 218, Jan. 2023, doi: 10.1016/j.applthermaleng.2022.119286.

[36] M. Pitarch, E. Hervas-Blasco, E. Navarro-Peris, J. Gonzálvez-Maciá, and J. M. Corberán, "Évaluation du sous-refroidissement optimal dans des systèmes de pompe à chaleur sous-critiques," *International Journal of Refrigeration*, vol. 78, pp. 18–31, Jun. 2017, doi: 10.1016/j.ijrefrig.2017.03.015.